Daniel Martin Lundeby

Improving the accuracy of TEM-EDX quantification by implementing the zeta-factor method

June 2019

Master's thesis

Master's thesis

2019

Daniel Martin Lundeby

NTNU
Norwegian University of
Science and Technology
Faculty of Natural Sciences
Department of Physics

NTNU
Norwegian University of
Science and Technology

NTNU
Norwegian University of
Science and Technology

NTNU

Norwegian University of
Science and Technology

Improving the accuracy of TEM-EDX quantification by implementing the zeta-factor method

Daniel Martin Lundeby

Abstract

To improve the accuracy of quantitative energy-dispersive spectroscopy (EDX) on transmission electron microscopes (TEM), approaches for determining ζ-factors have been developed and subsequently applied on a JEOL 2100 and a JEOL 2100F. For the JEOL 2100, the ζ-factor method was used for the first time. The ζ-factor method can achieve a much higher quantification accuracy than the usual approach of using the Cliff-Lorimer method with k-factors specified by commercial EDX software. These k-factors are normally calculated from first principles and can have an error of as much as 15-20 %. There are other important advantages to the ζ-factor method, such as simultaneous thickness determination, the possibility of performing absorption correction, and the possibility of determining ζ-factors from pure-element standards instead of special compounds.

A main pre-request of the ζ-factor method is that the beam current needs to be known. In this project, the beam current has been measured indirectly by using the charge-coupled device (CCD) used for imaging. Using a DigitalMicrograph script, the beam current on the JEOL 2100 was analyzed and verified to be stable enough for accurate ζ-factor measurements. In order to estimate the beam current, measurements should be done before and after EDX data collection. Furthermore, experimental settings affecting the measurements have been evaluated, and guidelines for consistent beam current measurements have been made.

In order to apply the ζ-factor method, ζ-factors must be known for every element to be quantified. ζ-factors with error terms have been determined for $\mathrm{Ga\,K_\alpha}$ and $\mathrm{As\,K_\alpha}$. Effects which influence the ζ-factors were studied. The stage tilt was found to cause consistent deviations in the ζ-factors due to shadowing effects beyond a critical angle, and the ζ-factors were independent of stage tilt if shadowing was absent. Furthermore, ζ-factors were found to vary when the sample was oriented close to a zone axis. For future ζ-factor determinations, it is recommended to avoid zone axes and to tilt the stage well beyond the critical angle where shadowing starts.

Finally, the experimentally determined ζ-factors were verified by applying the ζ-factor method to nanowires and nanoparticles with known composition. The ζ-factors were found to give similar or better results than the Cliff-Lorimer method in all studied cases. To further improve the quantification accuracy and practical use of the ζ-factor method, two refined approaches were demonstrated. The first approach is internal ζ-factors, which means that the standard to determine ζ-factors is within the analyzed area. Internal ζ-factors were demonstrated to give similar or better results than ζ-factors found in a calibration session. It is highly recommended to use internal ζ-factors in the cases where it is possible. In the second approach, a not yet determined ζ-factor, here $\mathrm{Sb\,L_\alpha}$, was found by using preknowledge on the overall composition. The indirectly determined ζ-factor was verified on a GaSb test sample.

The beam current measurement approach and the developed Python code for processing EDX data, as well as ζ-factors determined in this study, have been demonstrated to perform well compared with the Cliff-Lorimer method. However, more work is needed before the ζ-factor method can be used as conveniently as the Cliff-Lorimer method. ζ-factors need to be determined for more elements. The ζ-factors of missing elements can be found by estimation based on the experimentally determined ζ-factors and a model of the Z-dependence of ζ-factors. This way, a complete set of tabulated ζ-factors can be obtained. Furthermore, alternatives to using the CCD for indirect beam current measurements can be investigated. If this is done, the ζ-factor method should be an easy-to-use method, with better quantitative accuracy than the Cliff-Lorimer method today.

Sammendrag

For å forbedre nøyaktigheten til kvantitativ energispredningsspektroskopi (EDX) på transmisjonselektronmikroskoper (TEM), har tilnærminger for å bestemme ζ-faktorer blitt utviklet og deretter brukt for kvantifisering på en JEOL 2100 og en JEOL 2100F. For JEOL 2100 ble ζ-faktor-metoden brukt for første gang. ζ-faktor-metoden kan oppnå langt bedre kvantifiseringsnøyaktighet enn den vanligere tilnærmingen, som er å bruke Cliff-Lorimer-metoden med k-faktorer spesifisert av kommersiell EDX-programvare. Disse k-faktorene blir vanligvis regnet ut teoretisk, og kan ha feil på så mye som 15-20 %. Det er andre viktige fordeler ved ζ-faktor-metoden, for eksempel samtidig beregning av tykkelse, muligheten for absorpsjonskorreksjon, og muligheten for å bestemme ζ-faktorer fra standarder bestående av ett element i stedet for spesielle forbindelser.

En forutsetning for ζ-faktor-metoden er at elektronstrålestrømmen må være kjent. I dette prosjektet har elektronstrålestrømmen blitt målt indirekte ved å bruke en "charge-coupled device" (CCD) brukt for avbildning. Ved å bruke et skript i DigitalMicrograph ble elektronstrålestrømmen på JEOL 2100 analysert og verifisert til å være stabil nok for nøyaktig bestemmelse av ζ-faktorer. For å estimere elektronstrålestrømmen burde målinger utføres før og etter EDX-data blir tatt opp. Videre har eksperimentelle innstillinger som påvirker målingene blitt evaluert, og retningslinjer for måling av elektronstrålestrøm har blitt laget.

For å bruke ζ-faktor-metoden må ζ-faktorer være kjent for hvert element som skal kvantifiseres. ζ-faktorer med feilledd har blitt bestemt for $Ga\,K_{\alpha}$ og $As\,K_{\alpha}$. Effekter som påvirker ζ-faktorer har blitt studert. Det ble oppdaget at helningen til prøveholderen forårsaket konsistente avvik i ζ-faktorer på grunn av skyggelegging under en kritisk vinkel, og at ζ-faktorer var uavhengige av helningen når skyggelegging var fraværende. Videre ble det oppdaget at ζ-faktorene varierer når prøven var orientert nærme en soneakse. For fremtidige ζ-faktor-bestemmelser anbefales det å unngå soneakser, og å bruke en helningsvinkel på prøveholderen som er godt over den kritiske vinkelen der skyggelegging starter.

Til slutt ble eksperimentelt bestemte ζ-faktorer verifisert ved å bruke ζ-faktor-metoden på nanotråder og nanopartikler med kjent sammensetning. ζ-faktorene ble funnet å gi tilsvarende eller bedre resultater enn Cliff-Lorimer-metoden i alle studerte tilfeller. For å forbedre kvantifiseringsnøyaktigheten ytterligere ble to modifiserte tilnærminger demonstrert. Den første tilnærmingen er interne ζ-faktorer, som betyr at standarden brukt for ζ-faktor-bestemmelser ligger innenfor det analyserte området. Det ble demonstrert at interne ζ-faktorer gir tilsvarende eller bedre resultater enn ζ-faktorer bestemt fra en kalibreringsøkt. Det anbefales sterkt å bruke interne ζ-faktorer i de tilfeller det er mulig. I den andre tilnærmingen ble en ukjent ζ-faktor, i dette tilfellet $Sb\,L_{\alpha}$, funnet ved å utnytte kunnskap om sammensetningen til systemet som helhet. Den indirekte bestemte ζ-faktoren ble verifisert på en testprøve bestående av GaSb.

Tilnærmingen til elektronstrømstrålemålinger, Python-kode for prosessering av EDX-data, samt ζ-faktorer som har blitt bestemt i denne studien, har blitt demonstrert å gi gode resultater sammenlignet med Cliff-Lorimer-metoden. Allikevel kreves det videre arbeid før ζ-faktor-metoden kan brukes på en like enkel måte som Cliff-Lorimer-metoden. ζ-faktorer må bestemmes for flere elementer. ζ-faktorer for manglende elementer kan finnes ved estimering basert på eksperimentelt bestemte ζ-faktorer og en modell for Z-avhengigheten til ζ-faktorer. På denne måten kan et fullstendig sett av tabulerte ζ-faktorer bestemmes. Videre kan alternativer til å bruke en CCD for indirekte elektronstrømmålinger undersøkes. Hvis dette blir gjort, kan ζ-faktor metoden bli en metode som er lett å bruke, og som samtidig gir bedre kvantitativ nøyaktighet enn det Cliff-Lorimer-metoden gjør i dag.

Preface

This Master's thesis has been written as part of the Nanotechnology program at the Norwegian University of Science and Technology (NTNU), between January and June 2019. The thesis has been written for the TEM Gemini Centre, at the Department of Physics (IFY) at NTNU. The work has been supervised by professor Antonius T. J. van Helvoort and co-supervised by Ph.D. candidate Julie S. Nilsen. The datasets have been acquired by myself (for data on the JEOL 2100), Antonius T. J. van Helvoort (for data on the JEOL 2100F), postdoctoral fellow Dipanwita Chatterjee (for data on the 2100F) and Julie S. Nilsen (for data on the JEOL ARM-200F). All work has been done by myself, except for details on material and specimen preparation, which have been written by Antonius T. J. van Helvoort. The GaSb nanowires which have been used in this study were grown by Mazid Munshi, and prepared by Antonius T. J. van Helvoort and myself.

There are many people who deserve to be thanked. First of all, I would like to thank my supervisor, Antonius T. J. van Helvoort, for the great amount of support during this semester. He has helped me by numerous discussions, answering e-mails at any time, and spending many hours with me at the lab, for which I am very grateful. But most importantly, he has been an endless source of motivation. He has the ability to see possibilities in any area. After every meeting, I am inspired to take onto new challenges and make more progress.

A big thank you to my co-supervisor Julie Stene Nilsen for helping me on the microscope, for helpful discussions and for always being available for questions. Furthermore, I would like to thank Bjørn Soleim for performing beam current measurements which have been vital for this project. I am also grateful for the TEM training, and for always being available on TEM-related questions. Thanks to Ragnhild Sæterli for TEM training, and support when things go wrong. Furthermore, I would like to thank the many other Ph.D. students at the TEM Gemini Centre for discussing with me and showing interest in my project.

A great thank you to the developers of HyperSpy, which has been crucial for this work. Without HyperSpy, the data analysis in this work would not have been possible. I wish all the best for the further development of this highly important open source platform. Lastly, I would like to thank my family and friends for supporting me in life. This thesis would not have been a reality without their love and support.

I hereby declare that this Master's thesis is my own independent work and is in accordance with the regulations for the Master's degree program in Nanotechnology at NTNU.

Abbreviations

AEM	Analytical electron microscope
ADF	Annular dark-field
AES	Auger electron spectroscopy
ALCHEMI	Atom location by channeling-enhanced microanalysis
BF	Bright-field
CBED	Convergent-beam electron diffraction
CCD	Charge-coupled device
DF	Dark-dield
DP	Diffraction pattern
EDX	Electron-dispersive X-ray spectroscopy
EELS	Electron energy loss spectroscopy
FEG	Field emission gun
GIF	Gatan image filter
HAADF	High-angle annular dark-field
NIST	National Institute of Standards and Technology
NW	Nanowire
PCA	Principal component analysis
SAED	Selected area electron diffraction
SEM	Scanning electron microscopy
SDD	Silicon drift detector
STEM	Scanning transmission electron microscopy
TEM	Transmission electron microscopy
VLS	Vapor-liquid-solid
WDS	Wavelength-dispersive X-ray spectroscopy
WZ	Wurtzite
ZB	Zinc blende
ZOLZ	Zeroth order laue zone

Contents

Chapter 1

Introduction

In many studies of materials, it is essential to measure composition variations at high spatial resolution. For transmission electron microscopy (TEM), the most common technique for compositional analysis is energy-dispersive X-ray spectroscopy (EDX). TEM-EDX if often used to detect which elements are present in a sample (i.e., qualitative analysis); however, it can also be used for accurate quantitative analysis. The most commonly used EDX quantification method is the Cliff-Lorimer method [1]; however, this method has a number of serious drawbacks. A major issue is the accuracy of k-factors, which relate experimentally found X-ray intensities to composition. The most common method in practice is to use k-factors calculated from first principles by commercial EDX software. These k-factors typically have errors in the order of $\pm 20\%$. Experimental determination of k-factors is more accurate, but the procedure for doing this is tedious and inconvenient for many reasons. Furthermore, the Cliff-Lorimer method assumes there is no absorption in the sample, which is often not the case. It is possible to perform absorption correction; however, this is inconvenient as prior knowledge of the sample mass-thickness is required. Although the Cliff-Lorimer method fulfills the needs for many compositional analyses, the quantification accuracy could be improved.

An alternative EDX quantification method is the ζ-factor method [2], which overcomes many of the limitations of the Cliff-Lorimer method. Experimental determination of ζ-factors is more convenient than k-factors because only one factor per element is needed rather than one factor for each combination of elements. The accuracy of the ζ-factor method is far better than the usual method of using k-factors from commercial EDX software, once accurate ζ-factors are known. Moreover, the sample mass-thickness is determined simultaneously with the composition. This additional piece of information is highly useful, and allows for easy determination of important quantities such as the EDX spatial resolution and analytical sensitivity. Furthermore, absorption correction in the ζ-factor method is more convenient than for the Cliff-Lorimer method, as the sample mass-thickness does not need to

be known in advance.

Though the advantages of the ζ-factor method are clear, there are challenges in implementing it in practice. One aspect is the requirement that the beam current needs to be known. Most commercial TEMs do not have the capability of measuring the beam current directly. Moreover, although experimental ζ-factor determination is more convenient than k-factor determination, it is still a significant challenge. First, a suitable standard with known composition and mass-thickness is required. Then, a high number of measurements should be performed to ensure statistical confidence. Furthermore, there are many parameters related to the standard and the TEM setup which may influence the determination of ζ-factors.

In this project, the ζ-factor method will be implemented on a JEOL 2100 microscope as a practical and more accurate alternative to the more commonly used Cliff-Lorimer method. The overall goal is to improve the accuracy of quantitative TEM-EDX. To implement the ζ-factor method, the aforementioned challenges need to be targeted. A practical method for measuring beam current indirectly has to be established. ζ-factors need to be determined from standards with known composition and thickness. There are many factors which may influence the ζ-factor determination, such as the stage tilt, the crystal structure of the standard, and the TEM operating mode. These factors will be tested, so as to ensure the determined ζ-factors are robust. The found ζ-factors will then be verified by using the ζ-factor method to quantify samples with known composition. In order to verify the approach, ζ-factors will be determined and verified on another microscope as well: a JEOL 2100F. Furthermore, alternative approaches to the ζ-factor method will be demonstrated: If the composition is known at some region of the sample to be quantified, then these regions can be used for determining ζ-factors internally. Error terms cancel out, and the quantification accuracy can be significantly improved.

As a part of this work, Python code for determining ζ-factors is developed. The code is based on open-source software, which means that ζ-factor determination and quantification can be performed without relying on commercial, black-box software. The entire procedure of determining ζ-factors and applying the ζ-factor method is transparent, which means that errors can be tracked and subsequently fixed. The developed code is available as an attachment to this report. Furthermore, the code is generic, and can in principle be used for any TEM-EDX system.

The report is structured as follows. Chapter 2 introduces relevant theory for understanding TEM-EDX quantification, as well as the standards used for ζ-factor determination. Experimental details are presented in chapter 3. The results are presented in chapter 4, followed by the discussion in chapter 5. The work is concluded in chapter 6, and possible future work is suggested in chapter 7.

Chapter 2

Theory

2.1 TEM

The following theory is based on Williams and Carter [3]. In a transmission electron microscope (TEM), a beam of high energy electrons (typically, 100-300 keV) is sent through a thin ($\sim 100\,\text{nm}$) specimen, and various results of the beam-specimen interaction are detected. Electron microscopes differ from visible light microscopes in that electrons are used instead of visible light, which allows for higher spatial resolution as the wavelength of electrons is lower than that of visible light. In the TEM, the electrons are transmitted *through* the sample. For this reason, the sample needs to be thin, typically in the range of $100\,\text{nm}$. Figure 2.1 shows a schematic overview of a TEM column and the ray diagram in TEM mode and scanning transmission electron microscopy (STEM) mode. The electrons are generated in the electron gun and sent through a series of condenser lenses, before they hit and interact with the specimen atoms. Then, scattered electrons are then sent through a system of lenses which magnify the beam, and in the end, the electrons are recorded on a fluorescent viewing screen or a detector.

2.1.1 TEM modes

The electron beam can be converged or parallel when hitting the specimen (see figure 2.1(a) and 2.1(b), respectively). In TEM mode, the beam is approximately parallel, and a large specimen area is illuminated uniformly and recorded on a charge-coupled device (CCD) screen. On the other hand, in STEM mode, the electron beam is converged to a tiny spot. The spot is raster scanned over the specimen surface, and for each point, a detector records the measured electron intensity. The beam convergence is configured by adjusting the strengths of the
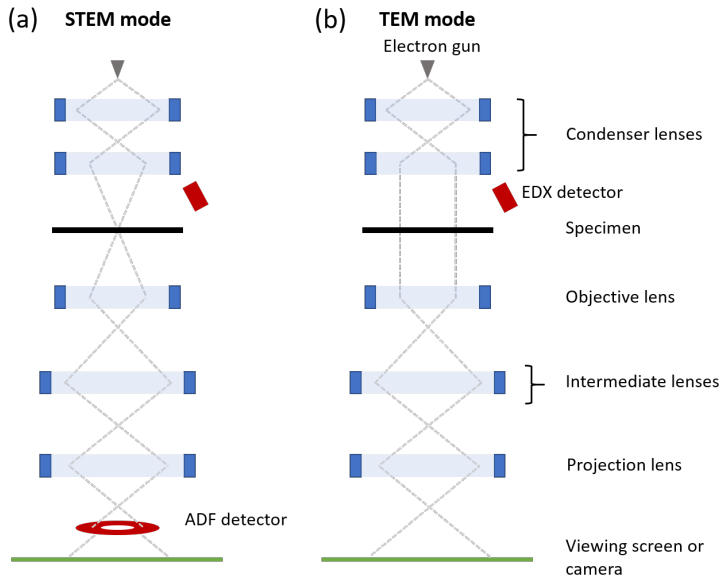
Figure 2.1: Schematic overview of the internals of a TEM, and the difference between (a) STEM mode and (b) TEM mode.

condenser lenses.

The contrast in TEM images depends on the mode and the detector being used. In bright-field (BF) imaging, only forward scattered electrons are being recorded. The background is then bright, and any material is dark. Conversely, in dark-field (DF) imaging, only scattered electrons are recorded, which leads to a dark background. In TEM mode, BF and DF imaging is performed by using an aperture to select diffraction spots in the objective plane. For BF images, only the central beam is let through, while for DF images one of the diffraction spots is chosen. In STEM mode, scattered electrons are selected by having different detector geometries. Figure 2.2 shows the main detectors geometries in STEM mode.

There exist electron microscopes other than TEM's, most prominently the scanning electron microscope (SEM). The SEM is used to study bulk specimens rather than thin, electron-transparent specimens. Electrons interact with the specimen atoms and are then reflected and analyzed by detectors above the specimen. The SEM always operates in scanning mode; only one pixel is considered at the time. Also, the SEM operates at lower voltages than the TEM, typically about $20\,\text{keV}$.
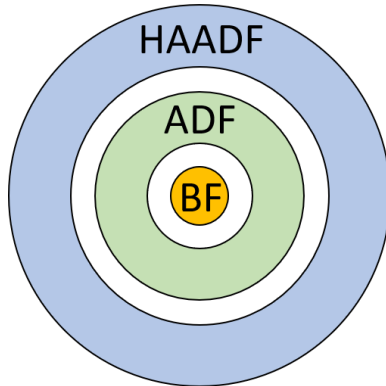
Figure 2.2: Top view of common STEM detectors. The BF detector detect electrons which are not scattered, while the annular dark field (ADF) and high-angle annular dark field (HAADF) detectors pick up electrons scattered at different angles.

2.1.2 The TEM column

Figure 2.1 shows a simplified schematic of a TEM column. Electrons are generated in the electron gun, travel down the column as they interact with the specimen, and finally hit the fluorescent viewing screen. The blue items on the figure are electromagnetic lenses. The lenses converge the electron beam the same way as optical lenses converge light rays. The electron beam is converged by a sequence of condenser lenses into a tiny beam which is transmitted through the specimen. The beam is then magnified by a series of intermediate lenses and finally passes through the projector lens before appearing on the fluorescent screen. The electromagnetic lenses consist of coils. When current flows through the coils, magnetic forces are induced, which affect and converge the electron beam. Due to the lenses being electromagnetic, it is possible to change their strength by changing the current in the coils. This cannot be done with conventional optical lenses.

In addition to lenses, there are many other components in the TEM column. *Stigmators* are used to correct for distortions of the beam by introducing compensating fields. *Deflectors* are used to shift or tilt the beam. Both stigmators and deflectors consist of coils, just like the lenses, and thus their strength can be adjusted. *Apertures* are used to limit the beam spread. An aperture consists of a metal plate with a circular hole. Apertures also reduce the beam intensity, as they prevent many electrons from traveling down the column. Before using the TEM, the TEM components should be properly aligned to ensure a high beam quality.

2.1.3 Recording electron signals

When operating the TEM, the transmitted beam is normally visible on a fluorescent viewing screen. In order to capture digital images from the microscope, a CCD camera can be used [3, p. 119]. The CCD is located either above or below the fluorescent viewing screen. The CCD camera consists of an array of millions of capacitor-based sensors, each of which detects incoming electrons and converts the input to electronic signals. The average number of CCD counts caused by a single incoming electron is termed the *conversion efficiency* of the detector. If the detector efficiency of the CCD is known, then it is possible to use the CCD as a detector for beam current. Ideally, all sensors respond in the same way to the same amount to incoming electrons; in practice, this is not the case. For this reason, it is useful to perform corrections. Important corrections have been described and visualized in appendix D.3.

2.2 Scattering

The following theory is based on Williams and Carter [3, ch. 2-4]. When the high energy electrons in the TEM electron beam interact with specimen atoms, various scattering events may happen. Scattering events which cause the electrons to lose energy are called *inelastic*. Conversely, if energy is conserved, then the scattering events are said to be elastic. Elastic scattering is the basis for bright- and dark-field imaging, as well as for diffraction. They are, thus, essential for most TEM studies. However, the main focus of this project is inelastic scattering, which gives very useful complementary information.

2.2.1 Scattering cross sections

The likelihood of a particular scattering event to happen is described by a quantity called the scattering cross section, conventionally denoted by σ, and in units of m^2 or Barn. Typical elastic and inelastic scattering events which happen in TEM samples are shown in figure 2.3.
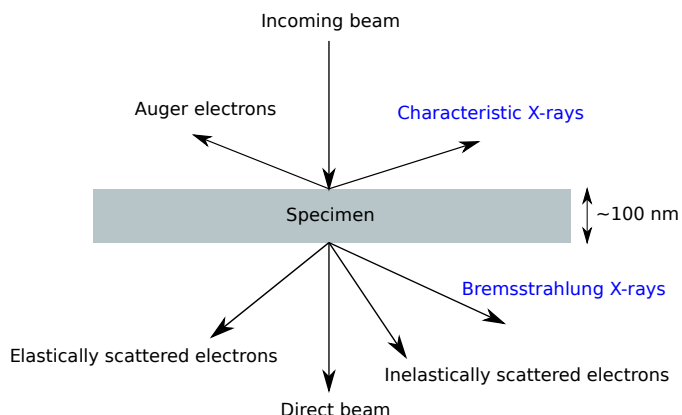
Figure 2.3: When the incoming electrons hit the thin TEM specimen, many interactions can happen; some of them are shown in this figure. Black labels indicate electrons, while blue labels indicate X-rays. The figure is adapted from Williams and Carter [3, p. 25].

The cross section often has an angular dependency; that is, the probability of scattering depends on the angle at which electrons are scattered. This angular dependency is described by the differential cross section, $d\sigma/d\Omega$. The total cross section is found by integrating the differential cross section over all solid angles. Cross sections represent complex physical phenomena which are difficult to describe accurately, but approximate expressions exist.

2.2.2 Inelastic scattering

When the incoming electrons interact inelastically with the specimen, they lose energy. Inelastic scattering processes can be classified into three types [3, p. 54]:

1. Processes involving the generation of X-rays

2. Processes involving the generation of secondary electrons

3. Processes resulting from collective interactions

A TEM which is able to detect the first type of processes, i.e., X-rays and the accompanying loss of incoming electrons, is called an analytical electron microscope (AEM). This involves two techniques: Electron-dispersive X-ray spectroscopy (EDX), which is used to study X-rays, and electron energy loss spectroscopy (EELS), which is used to study the energy loss of the incoming electrons. The second type of process is primarily studied in the SEM, where secondary electrons

are much more prominent. The third type includes plasmon and phonon scattering; the latter can be detected by EELS. This section focuses on X-ray generating processes.

A schematic of the process which causes the generation of X-rays is shown in figure 2.5. The likelihood of the ionization event in figure 2.5(a) is given by the K-shell ionization cross section. A commonly used expression for total ionization cross is given by equation 2.1 [3, p. 57]. Many cross section models are variants of Bethe's expression.

$$\sigma_T = \left(\frac{\pi e^4 b_s n_s}{E_0 E_c} \right) \log \left(\frac{c_s E_0}{E_c} \right) \tag{2.1}$$

E_0 is the beam energy, and E_c is the critical ionization energy. n_s is the number of electrons in the electron shell where ionization happens, while b_s and c_s are constants for that shell. e is the elementary charge. Note that there is no angular dependency, which means that X-ray emission is equally probable in all directions. The ratio of beam energy to critical ionization energy is termed *overvoltage*. The cross section is largest at an overvoltage of about 5.

Following ionization, the atom stabilizes its energy state by de-excitation of electrons (see figure 2.5(b)). This typically happens in an "avalanche manner": A transition from the L shell to the K shell is followed by a transition from the M shell to the L shell, and so on. These de-excitation events are followed by either the emission of Auger electrons or characteristic X-rays (see figure 2.5(c). The characteristic X-rays can be detected by an EDX. Auger electrons can be detected by Auger electron spectroscopy (AES) systems, which are typically not combined with TEMs.

The ratio of characteristic X-ray emission events to Auger electron emission events is called the *fluorescence yield*, and it depends on the atomic number. An approximate formula for the fluorescence yield is given by equation 2.2,

$$\omega = \frac{Z^4}{a + Z^4} \tag{2.2}$$

In this equation, Z is the atomic number, and a is a constant which depends on the X-ray family. Figure 2.4 shows the plot of the K-shell fluorescence yield for a range of atomic numbers. Equation 2.2 and figure 2.4 indicate a very strong Z-dependence. For low-Z materials, the fluorescence yield is very low, while characteristic X-ray emission becomes more dominant at higher atomic number. This means that light elements can be difficult to detect by the EDX. In such cases, it may be more convenient to use alternative techniques such as EELS, where electron energy loss is studied instead.
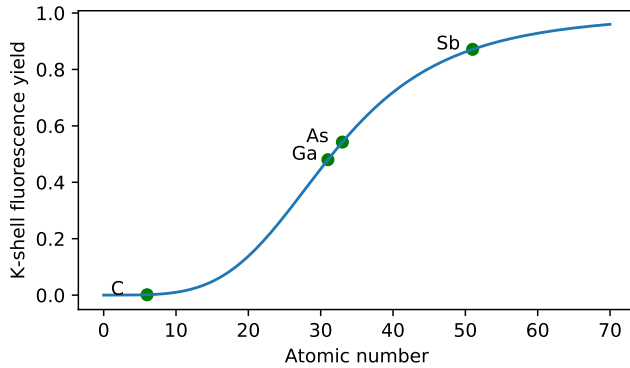
Figure 2.4: Fluorescence yield as calculated by equation 2.2 for the K-shell $(a \sim 10^6)$. Some elements which are important for this project are labeled. Note the very low fluorescence yield of carbon; this means that almost all ionization events are followed by Auger emission.
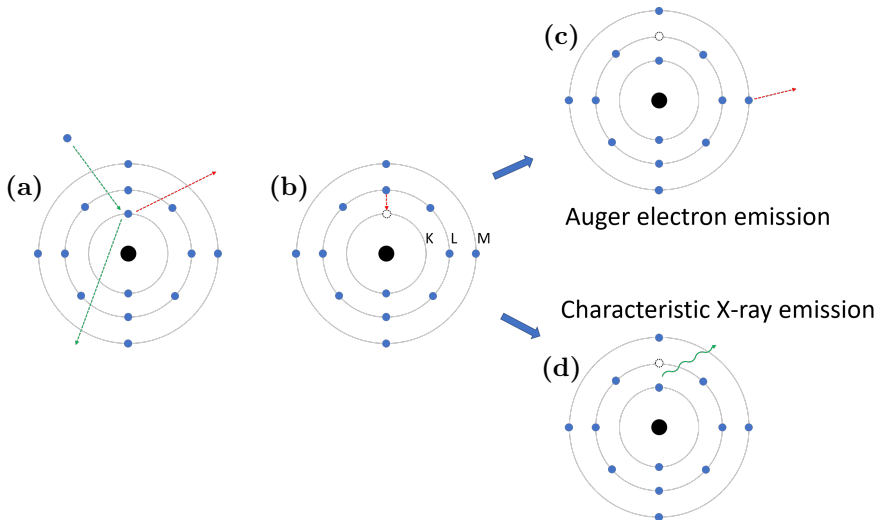
Figure 2.5: (a) An incoming electron causes the emission of a core electron. (b) A higher-energy electron is de-excited to the K shell. The energy from the de-excitation process is transferred either to (c) a characteristic X-ray or to (d) an Auger electron.

2.2.2.1 Characteristic X-rays

In figure 2.5, many different electronic transitions are allowed, giving rise to characteristic X-rays with different wavelengths. Figure 2.6 shows a few of them, as

well as the labeling of the X-ray lines.
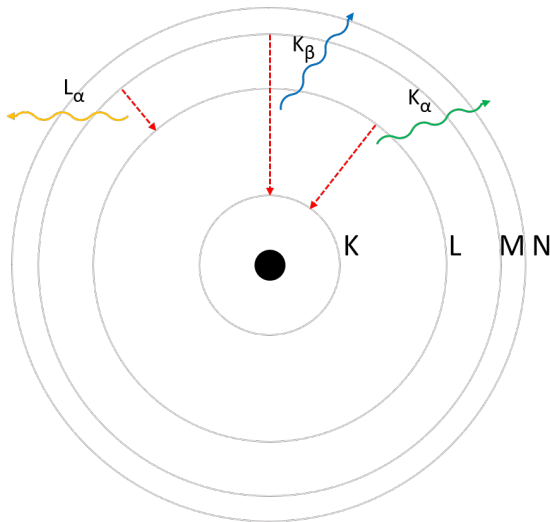
Figure 2.6: De-excitation of electron may cause emission of characteristic X-rays. The X-rays are labeled according to which shells the electrons are transitioned between.

Characteristic X-rays are labeled by a letter and a subscript. The letter tells about the *family* of the X-ray. X-rays are grouped into families based on which shell the electrons end up at. For example, the K-family of X-ray lines consists of all X-ray lines for which the electrons end up in the K shell. The subscripts tell about which shell the de-excited electrons come from. As a main rule, α means that the electron has jumped one shell, while β means that the electron has jumped two shells. However, there are many exceptions to this rule. In reality, each shell consists of a number of subshells. To denote subshells, one can add indices to the subscripts such as $K_{\alpha 1}$ and $K_{\alpha 2}$. However, due to the limited energy resolution of the EDX detector, subshells are often indistinguishable. This topic is further complicated by the fact that not all transitions are allowed - this is all explained by quantum mechanical rules.

It turns out that the relative intensities of X-ray lines within the same family are fairly constant. This constant is termed the *relative transition probability*, and labeled a. A database of transition probabilities can be found in the EPQ library [4], which is a project by the National Institute of Standards and Technology (NIST), and is available through HyperSpy [5]. It should be noted that there are some inconsistencies in the literature for the absolute values of the transition probabilities. Table 2.1 summarizes the $Ge\,K_{\beta}$ / $Ge\,K_{\alpha}$ ratios from different sources in the literature.

Table 2.1: Ratio of the line intensities of $Ge\,K_\beta$ to $Ge\,K_\alpha$, from different sources in the literature.

Reference	$Ge\,K_\beta$ / $Ge\,K_\alpha$
EPQ library [4]	0.1322
Scofield, 1 [6]	0.1504
Scofield, 2 [7]	0.1321
Salem [8]	0.147

2.2.2.2 Bremsstrahlung X-rays

There is another type of X-rays which is generated in the specimen, namely Bremsstrahlung X-rays. The origin of Bremsstrahlung X-rays is fundamentally different from characteristic X-rays. Incoming electrons can interact strongly with the atomic nuclei in the specimen and undergo a substantial change in momentum. During this process of electron acceleration, X-rays are emitted - these are called Bremsstrahlung X-rays. As the electron can undergo any change in momentum, the Bremsstrahlung energy spectrum is continuous. This is in contrast to characteristic X-rays, which are sharply defined. The intensity of the Bremsstrahlung depends on the energy, and a common approximation for the energy dependence is given by Kramers' cross section:

$$N(E) = \frac{KZ(E_0 - E)}{E} \tag{2.3}$$

K is Kramers' constant, Z is the atomic number of the ionized atom, E_0 is the beam energy, and E is the Bremsstrahlung energy. Figure 2.7 shows the typical shape of a Bremsstrahlung spectrum. Note that equation 2.3 predicts an intensity approaching infinity at low energies, a trend which is not present in figure 2.7. The reason for this is limited EDX detection efficiency at low energies (see section 2.3).
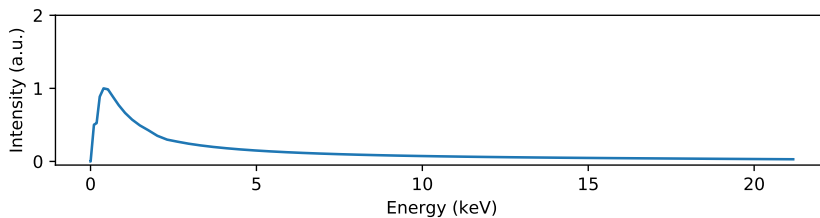

Figure 2.7

2.3 The EDX detector

The following theory is based on Williams and Carter [3, ch. 32]. X-rays in the TEM chamber can be detected by a technique called electron-dispersive X-ray spectroscopy (EDX). In short terms, the EDX detector records intensities of each X-ray energy, resulting in EDX spectra. The topic of this section is the EDX detector itself; qualitative and quantitative EDX analysis are described in section 2.5 and 2.4, respectively. The generation of X-rays has been described in the section on scattering (section 2.2).

The EDX detector detects incoming X-rays and converts the information to electronic signals, which are subsequently processed and converted into an EDX spectrum. There are various types of EDX detectors, but the basic principle is the same: Incoming X-rays hit a semiconductor material, causing the creation of electron-hole pairs. The magnitude of the resulting current pulse is proportional to the energy of incoming X-rays. Because the X-ray energy is much higher than the semiconductor band gap, one single X-ray can create thousands of electron-hole pairs.

The real linewidths of the X-rays are only a few eV because the atomic energy levels are sharply defined; however, EDX detectors measure X-ray linewidths in the order of 100 keV. The reason for the limited energy resolution is fluctuations in the number of electron-hole pairs, and limitations in the processing electronics. This can be improved by using wavelength-dispersive spectroscopy (WDS). The WDS discriminates X-rays based on their *wavelength* rather than their energy, using the principle of Bragg diffraction. As only a small range of wavelength is recorded at the same time, the energy resolution is much higher. However, the approach is much more time-consuming. The WDS is normally not readily available for installation on TEM's.

The detector needs finite time to process an incoming X-ray, and the detector is switched off during this very short time, which is referred to as *dead time*. The time for which the detector is waiting for X-rays is called *live time*. The *real time* is the sum of the live time and the real time. In many cases, it is the live time which is of interest, as it does not include the time when the detector is idle. In STEM mode, the beam is scanned from pixel to pixel. The time spent on one single pixel is referred to as the *dwell time*. The full set of pixels in the area chosen for EDX analysis is called a *frame*.

There are various types of EDX detectors. Traditionally, Si(Li) detectors have been used. They consist of Si as the semiconductor material, as well as a small amount of Li to neutralize acceptor impurities. A reverse bias is applied to separate positive and negative charges more easily, resulting in an intrinsic region with shallow junctions on either side. Some detectors use germanium as the semiconductor material. Ge detectors are advantageous because their energy resolution is better than for Si detectors, and their detector efficiency is higher for heavy elements. While the Si detector efficiency starts to drop at about 20 keV, Ge detectors have a reasonable

efficiency even at 80 keV. More recently, silicon drift detectors (SDD) have become common. These are CCD devices with p-doped regions organized in concentric circles, and allow for much higher throughput than Si(Li) detectors.

2.3.1 Detector efficiency

The detector efficiency (ϵ_A) is the ratio of X-rays which are detected by the EDX detector, and it is dependent on the X-ray energy. The detector efficiency depends heavily on absorption in layers in front of the detector. As seen in figure 2.8, the detector often contains a window in front, an anti-reflective coating layer, and an electrode. All of these additional layers may absorb X-rays before they reach the intrinsic region where the actual detection is happening. Low energies are more readily absorbed, which means that the detector is less efficient at low energies. Ideally, all X-rays should be absorbed within the active, intrinsic semiconductor layer. However, high energy X-rays are less subject to absorption and may be transmitted straight through the detector. The result is a reduction in detector efficiency at high energies.
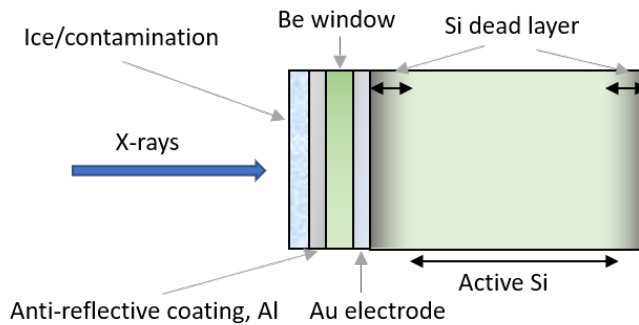
Figure 2.8: Schematic of a typical EDX detector. The X-rays go through a number of layers before entering the active Si region, where the actual detection happens. These layers reduce the detector efficiency. The figure is adapted from Williams and Carter [3, p. 585].

Absorption can be described by Beer-Lambert's law,

$$I = I_0 \exp\left(- \left[\mu/\rho\right]_{\mathrm{B}}^{A} * \rho t\right) \tag{2.4}$$

I_0 is the original signal intensity, and I is the intensity after undergoing absorption. $\left[\mu/\rho\right]$ is the absorption coefficient of the A X-ray line in element B, and ρt is the sample mass-thickness. The detector efficiency can be estimated by applying the Beer-Lambert law repeatedly,

$$\epsilon_A = \exp\left(-\left.\frac{\mu}{\rho}\right]_{\text{Be}}^{A} \rho_{\text{Be}} t_{\text{Be}}\right) \exp\left(-\left.\frac{\mu}{\rho}\right]_{\text{Au}}^{A} \rho_{\text{Au}} t_{\text{Au}}\right)$$

$$\exp\left(-\left.\frac{\mu}{\rho}\right]_{\text{Si}}^{A} \rho_{\text{Si}} t_{\text{Si}}\right) \left\{1 - \exp\left(-\left.\frac{\mu}{\rho}\right]_{\text{Si}}^{A} \rho_{\text{Si}} t'_{\text{Si}}\right)\right\} \quad (2.5)$$

The first three factors account for absorption in the layers in front of the active layer, while the last factor accounts for the intensity which is *not* absorbed in the active layer. The terms in the equation should be substituted for the actual layers in the detector. For example, in order to describe the detector in figure 2.8, the equation should have additional terms for the anti-reflective coating and the ice/-contamination layer. A detector efficiency of 1 means that all X-rays are absorbed in the active region only. The detector efficiency can be calculated theoretically if all absorption coefficients and the lengths of the layers are known (which they are usually not). Figure 2.9 shows the typical shape of the detector efficiency.
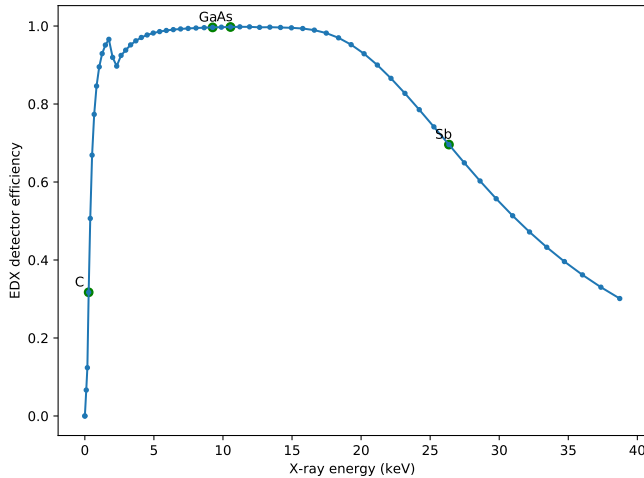
Figure 2.9: Detector efficiency, as calculated for a hypothetic EDX system using equation 2.5. Plausible values for the different thicknesses were used. The efficiency drops at low energies because of absorption before reaching the detector active region, and at high energies because the X-rays go straight through the detector. Some elements important for this study are indicated.

2.3.2 Detector geometry

The detector is mounted on a fixed angle relative to the horizontal plane; this angle is called the *elevation angle*. The *take-off angle* is defined as the detector

angle relative to the specimen plane. The take-off angle is thus dependent on the specimen tilt. There is a distinction between the *stage tilt* and the *specimen tilt*. The TEM operator only controls the stage tilt, while the specimen does not need to lay flat on the stage plane. Another important quantity is the detector *solid angle*. This is the solid angle spanned by the detector, defined with the specimen at the origin. The solid angle should be as high as possible, so as to increase the number of X-ray counts. The solid angle can be increased by placing the detector as close as possible to the specimen. The different angles are visualized in figure 2.10.
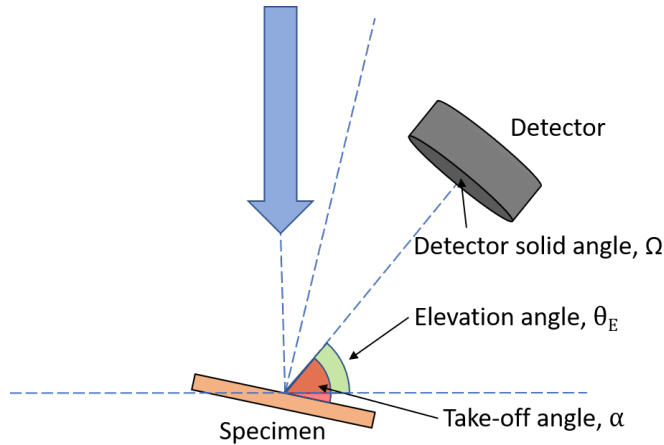
Figure 2.10: Visualization of important angles in EDX.

The EDX detector is usually located above the specimen (see figure 2.1). The reason for this is related to differential cross sections. Bremsstrahlung X-rays are mainly generated at low angles relative to the direction of the incoming electron beam. However, characteristic X-rays are emitted with equal probability in all directions. Thus, by locating the EDX detector on top of the specimen, the amount of Bremsstrahlung is minimized, so that the characteristic X-rays experience less distortion.

2.3.3 Shadowing

There may not be a free path between the specimen and the detector. The path can be blocked by the specimen holder or the grid, as shown in figure 2.11. In the figure, only the specimen holder contributes to shadowing as the Cu grid is facing downwards. It is possible to avoid shadowing by tilting the stage against the detector, as shown in figure 2.12.
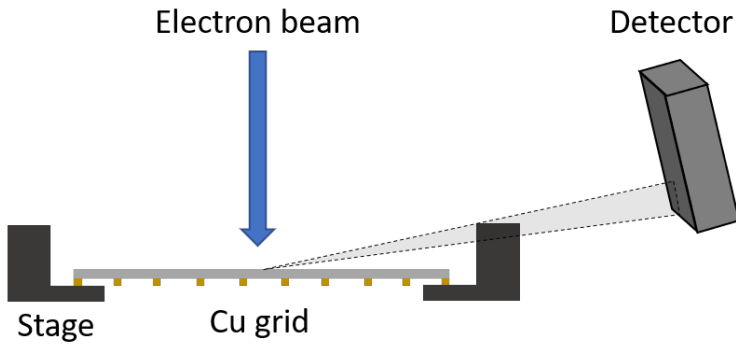
Figure 2.11: The specimen is shadowed by the stage, so that the effective solid
angle of the detector is reduced.
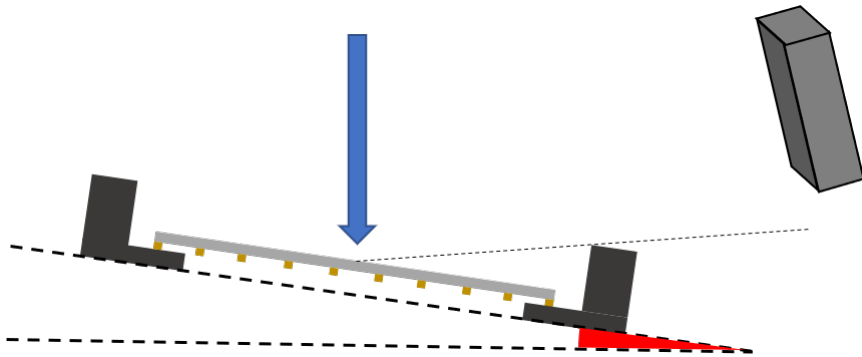
Figure 2.12: Shadowing can be avoided by tilting the specimen against the
detector

2.4   Qualitative EDX

The following theory is based on Williams and Carter [3, ch. 34]. EDX can be
used to perform qualitative elemental analysis, that is, determining which elements
are present in the sample. This is done by analyzing the peaks of EDX spectra.
Figure 2.13 shows an example of an EDX spectrum from a GaAs specimen.
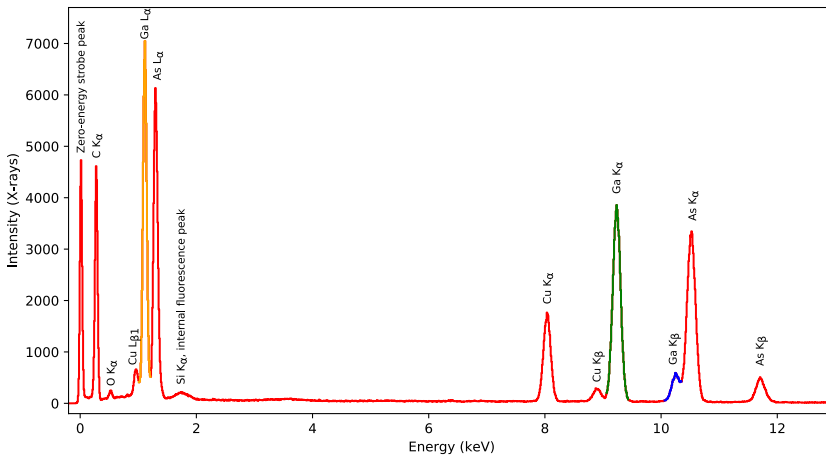
Figure 2.13: EDX spectrum of a GaAs specimen. EDX spectra consist of characteristic X-rays superimposed on a slowly varying background from Bremsstrahlung X-rays. The colored Ga peaks originate from the transitions in figure 2.6.

All EDX spectra have two distinct features. Firstly, there are sharp peaks originating from characteristic X-rays. For example, note the colored X-ray lines on the spectrum, which all originate from Ga atoms. These X-ray lines correspond to the highlighted transitions on figure 2.6. Secondly, there is a slowly varying background, on which the peaks are superimposed. The Bremsstrahlung X-rays are not prominent in figure 2.13 (which is good, as they distort the characteristic X-rays), but they are usually more prominent on SEM-EDX spectra.

The characteristic X-rays can be used to analyze which elements exist in the specimen, that is, to perform a *qualitative elemental analysis*. There must be some statistical evidence that a peak originates from an actual element and not just random noise. All EDX spectra have some noise, being Poisson distributed (see e.g., [9, p. 291]), and the noise level is higher when the X-ray count rate is low. A common criterion to evaluate whether an element A is present is shown below [3, p. 632]:

$$I_A > 3\sqrt{I_A^b} \tag{2.6}$$

I_A is the peak intensity and I_A^b is the intensity at the background, both integrated over the same energy width. If this criterion is satisfied, then there is a 99 % statistical confidence that the peak is physical.

Qualitative EDX analysis is challenging because some peaks may not be real. Table 2.2 lists common artifacts on EDX spectra.

Table 2.2: Common artifacts on EDX spectra

Artifact	Description
Escape peaks	If an incoming X-ray fluoresces a Si atom in the active region which then escapes from the specimen, then the X-ray will effectively lose that amount of energy. This results in an *escape peak* with energy 1.74 keV less than the real peak.
Internal fluorescence peak	Si (or Ga) in the dead layer can be fluoresced and then detected as characteristic peaks.
Sum peaks	If two photons enter the detector in virtually the same time, so that the detector cannot distinguish them, then a sum peak of the photons will be recorded.
Spurious X-rays	X-rays originating from the specimen, at regions which have not been illuminated by the electron beam.
System X-rays	X-rays from anywhere in the TEM chamber apart from the specimen.

The spectrum at figure 2.13 contains some of these artifacts. Normally, escape peaks and sum peaks are only visible when the total spectrum count is very high. They are not present on this spectrum. The spectrum does contain a Si internal fluorescence peak. The Cu in the spectrum comes from the sample grid and is considered a system X-ray. A small sign of a peak at 6.4 eV indicates the presence of Fe, which likely would be a system X-ray originating from the polepiece.

Besides, all EDX spectra contain a zero-energy strobe peak, which originates from the electronic noise in the detector [10]. This is removed automatically by some EDX software, but it has not been removed in figure 2.13.

2.5   Quantitative EDX

A common use case of EDX is to quantify the elements present in the specimen. EDX quantification is possible because the composition C_A of an element is directly related to its X-ray line intensities I_A in EDX spectra. The relation is given by equation 2.7 [2], where A denotes a specific X-ray line of a given element.

$$I_A = D_e \rho t C_A \frac{N_V}{M_A} Q_A \omega_A a_A \left(\frac{\Omega}{4\pi} \right) \epsilon_A \qquad (2.7)$$

The equation is valid under the thin-film approximation, which means that absorp-

tion and fluorescence effects are negligible. This is a reasonable approximation for very thin samples and for heavy elements. The individual terms in equation 2.7 are listed below:

- D_e: Electron dose applied by the electron beam. It is further given by $D_e = N_e I_p \tau$, where the constant N_e is the number of electrons per unit charge, I_p is the beam current and τ is the acquisition time.

- ρt: Mass-thickness of the specimen.

- C_A: Composition of element A.

- N_V: Avogadro's number

- M_A: Atomic mass of element A.

- Q_A: Ionization cross section. Discussed in section 2.2.2.

- ω_A: Fluorescence yield. Discussed in section 2.2.2.

- a_A: Relative transition probability. Discussed in section 2.2.2.1.

- $\Omega/4\pi$: Detector solid angle. Discussed in section 2.3.2.

- ϵ_A: Detector efficiency. Discussed in section 2.3.1.

Two methods for quantitative EDX are presented in the proceeding sections. Table 2.3 summarizes important equations for each method.

Table 2.3: Comparison of the Cliff-Lorimer method and the ζ-factor method. All symbols have been defined in the list above.

	Cliff-Lorimer	**ζ-factor method**
Factor definition	$k_{AB} = \frac{M_A}{M_B} \frac{Q_B \omega_B a_B}{Q_A \omega_A a_A} \frac{\epsilon_B}{\epsilon_A}$	$\zeta_A = \frac{M_A}{N_V Q_A \omega_A a_A \left(\frac{\Omega}{4\pi}\right)\epsilon_A}$
Experimental factor determination	$k_{AB} = \frac{C_A/C_B}{I_A/I_B}$	$\zeta_A = \frac{\rho t C_A D_e}{I_A}$
Determining composition	$\frac{C_A}{C_B} = k_{AB} \frac{I_A}{I_B}, \sum_i C_i = 1$	$C_A = \zeta_A I_A, \sum_i C_i = 1$

2.5.1 The Cliff-Lorimer method

The Cliff-Lorimer quantification method [1] is a *ratio technique*, which means that compositions are always found relative to each other. Consider a specimen with

two elements, A and B. Using the Cliff-Lorimer method, elemental compositions can be found by the following equation,

$$\frac{C_A}{C_B} = k_{AB} \frac{I_A}{I_B} \tag{2.8}$$

The ratio of the compositions is proportional to the ratio of the intensities, with a correction factor k_{AB} in front. To find the actual composition, it is assumed that A and B sum up to 100 %:

$$C_A + C_B = 100\% \tag{2.9}$$

The method can be trivially extended to any number of components by imposing additional constraints in the form of 2.8, and extending equation 2.9 to include all new elements.

The number k_{AB}, normally called the k-factor, relates the compositions of A and B. It is not a proper constant, but it is referred to as a *sensitivity factor*. It depends on the particular AEM system, the voltage, and analysis conditions in general. An expression for k_{AB} can be found by combining equation 2.8 with equation 2.7:

$$k_{AB} = \frac{M_A}{M_B} \frac{(Q\omega a\epsilon)_B}{(Q\omega a\epsilon)_A} \tag{2.10}$$

Importantly, some factors are canceled out from equation 2.15. This includes D_e, which means that the Cliff-Lorimer method is entirely independent of beam current. Also, the factor $\Omega/4\pi$ has been canceled out. This means that shadowing of the EDX detector (see section 2.3.3) is not an issue.

In most EDX software, k-factors are calculated from first principles based on equation 2.10. This introduces large errors, in particular because there is large uncertainty in the absolute value of the ionization cross section (see e.g. Watanabe [2]). Theoretical k-factors typically have an uncertainty of $\pm$ 20 %.

It is possible to determine k-factors experimentally, which reduces errors dramatically. However, the procedure is rather tedious. A central part of the challenge is to find a sample with known composition, containing the exact same elements as the material being analyzed. Furthermore, the sample should be thin enough for absorption to be neglected, and it should be prepared without introducing contaminations.

k-factors are usually specified relative to a given element, typically Si. Si is then called a pivot element. The k-factor $k_{A,Si}$ is then labeled just k_A. In order to

obtain a proper k-factor from relative k-factors, the following relation is used:

$$k_{AB} = \frac{k_A}{k_B} \tag{2.11}$$

2.5.1.1 Absorption correction

The following theory is based on Williams and Carter [3, p. 654]. Equation 2.8 is only valid under the thin-film approximation. It is, however, to some degree possible to adjust the k-factor to account for absorption. Then, a corrected factor k_{AB}^* is defined,

$$k_{AB}^* = k_{AB} \cdot \text{ACF} \tag{2.12}$$

ACF is an *absorption correction factor*. In the case of a thin film, an expression for ACF is given below:

$$\text{ACF} = \frac{\int_0^t \left\{ \varphi_B\,(\rho t) \exp\left[-\left(\mu/\rho\right)_{\text{sp}}^B \rho t \csc \alpha \right] \right\} \mathrm{d}\rho t}{\int_0^t \left\{ \varphi_A\,(\rho t) \exp\left[-\left(\mu/\rho\right)_{\text{sp}}^A \rho t \csc \alpha \right] \right\} \mathrm{d}\rho t} \tag{2.13}$$

$\varphi_B\,(\rho t)$ denotes the distribution of the depth of X-ray production. $\left(\mu/\rho\right)_{\text{sp}}^A$ is the absorption coefficient of X-ray line A in the specimen, and α is the take-off angle. The remaining terms are defined in the beginning of section 2.5. Assuming $\varphi_B(\rho t) = 1$, the expression can be simplified to

$$\text{ACF} = \frac{\left(\mu/\rho\right)_{\text{sp}}^A \left(1 - \exp\left[\left(\mu/\rho\right)_{\text{sp}}^B \rho t \csc \alpha \right] \right)}{\left(\mu/\rho\right)_{\text{sp}}^B \left(1 - \exp\left[\left(\mu/\rho\right)_{\text{sp}}^A \rho t \csc \alpha \right] \right)} \tag{2.14}$$

It is important to note that the absorption correction term requires the mass-thickness ρt to be known.

Note the term $t \csc \alpha$ in equation 2.14, which is the *absorption length*, often denoted by t'. The absorption length depends on the take-off angle α, shown in figure 2.14.
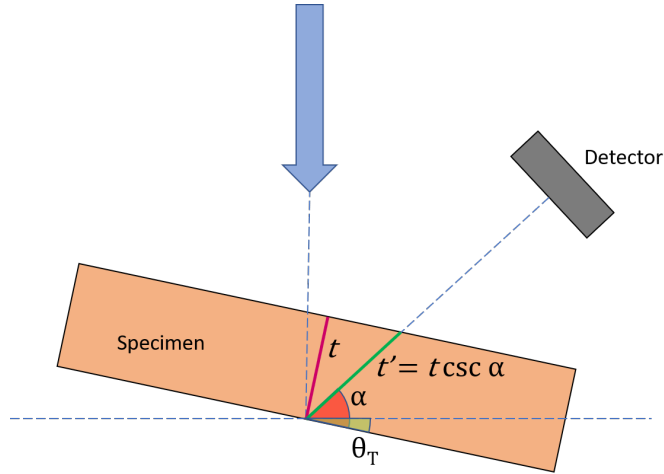
Figure 2.14: Absorption in the specific case of a thin film foil, tilted by an angle θ_T relative to the reference plane defined by the electron beam. t' is the absorption path length, t is the real specimen thickness and α is the take-off angle.

2.5.2 The ζ-factor method

The following section is based on Watanabe [2]. The ζ-factor method is based on absolute intensities and compositions rather than ratios. The composition of a given element is directly related to the intensity of the corresponding X-ray lines in the EDX spectrum. The relation is given below:

$$\rho t = \zeta_A \frac{I_A}{C_A D_e} \qquad (2.15)$$

Equation 2.15 relates the intensity and composition with the mass-thickness and the electron dose, which are all measurable quantities. There is a proportionality constant ζ_A, referred to as a ζ-factor. By comparing with equation 2.7, the ζ-factor is given by

$$\zeta_A = \frac{M_A}{N_V Q_A \omega_A a_A \left[\Omega/\left(4\pi\right)\right]\epsilon_A} \qquad (2.16)$$

The ζ-factor contains terms which generally do not change from one EDX experiment to the next. Thus, the ζ-factor is a constant for a given element and a given EDX system.

Equation 2.15 can be combined with the fact that all compositions sum up to unity.

The result is shown in the expression below.

$$\rho t = \frac{1}{D_e} \sum_{j}^{N} \zeta_j I_j, \quad C_A = \frac{\zeta_A I_A}{\sum_{j}^{N} \zeta_j I_j}, \quad \ldots, \quad C_N = \frac{\zeta_N I_N}{\sum_{j}^{N} \zeta_j I_j}, \tag{2.17}$$

These equations can be used to find the composition of any n-ary system from EDX spectra, once ζ-factors are known. If the electron dose is known as well, then the mass-thickness can be determined simultaneously. Applying the ζ-factor method is straightforward once accurate ζ-factors are known; however, the challenge is to find accurate ζ-factors. This is discussed in section 2.5.2.2.

2.5.2.1 Absorption correction

The ζ-factor method can be trivially extended to account for absorption. For each element j, an absorption-correction term A_j is defined [2],

$$A_j = \frac{\left(\mu/\rho\right)_{\mathrm{sp}}^{j} \rho t \csc \alpha}{1 - \exp\left[-\left(\mu/\rho\right)_{\mathrm{sp}}^{j} \rho t \csc \alpha\right]} \tag{2.18}$$

Absorption correction is included by multiplying each factor ζ_j in equation 2.17 by the corresponding correction factor A_j. The resulting equations are given below

$$\rho t = \frac{1}{D_e} \sum_{j}^{N} \zeta_j I_j A_J, \quad C_A = \frac{\zeta_A I_A A_A}{\sum_{j}^{N} \zeta_j I_j A_j}, \quad \ldots, \quad C_j = \frac{\zeta_N I_N A_N}{\sum_{j}^{N} \zeta_j I_j A_j}, \tag{2.19}$$

Note that the correction term includes ρt itself. For this reason, it is necessary to use an iterative procedure to solve the equations. However, just as for the non-absorption case ρt is found simultaneously with the compositions. This is very important, as it means that no prior knowledge of the specimen thickness and density is required to perform absorption correction. This is in contrast to Cliff-Lorimer absorption correction, which requires the mass-thickness to be known (see equation 2.14). Actually, absorption correction was a primary motivation for introducing the ζ-factor method in the first place.

Being able to calculate the specimen mass-thickness is an advantage in itself, but it also opens up for other applications. For example, it is possible to calculate rough estimates of the detector resolution and the minimum detection limit [2].

2.5.2.2 Determining ζ-factors experimentally

Before applying the ζ-factor method, ζ-factors need to be determined. By determining ζ-factors experimentally, it is possible to achieve much better accuracy than theoretical calculations; however, doing this in practice is a challenging task. In the ζ-factor method, only one ζ-factor is necessary for each element. This is in contrast to Cliff-Lorimer, which in principle requires one k-factor for every combination of elements.

Equation 2.15 can be rearranged to an equation from which ζ-factors can be determined experimentally from standards:

$$\zeta_A = \frac{\rho t C_A D_e}{I_A} \tag{2.20}$$

Thus, to determine ζ-factors, it is necessary to have a standard with known thickness t and composition C_A. Furthermore, the electron dose D_e must be known. This is a fundamental limitation to the ζ-factor method because the beam current cannot be measured directly on all TEMs. The accuracy of the ζ-factors is directly related to the accuracy of the thickness, composition, and electron dose.

On the other hand, the Cliff-Lorimer method needs neither the specimen thickness or the electron dose to be known when determining k-factors. However, the Cliff-Lorimer method has a limitation: Pure-element standards cannot be used to determine k-factors. This is because k-factors are always specified as a ratio between two elements. For the ζ-factor method, both pure-element and multielemental compounds can be used.

Absorption

Equation 2.20 is only valid under the thin-film approximation. As a consequence, absorption should be negligible when determining ζ-factors. However, this condition is not always true. Figure 2.15 shows the critical specimen thickness at which there is 5 % absorption, which is considered negligible. Most K-lines are free of absorption; however, many L-lines and M-lines have non-negligible absorption. In the corresponding plot by Watanabe [2] (attached in appendix E), many more K-lines and L-lines are shown to be subject to non-negligible absorption. For these lines, determining ζ-factors is a much more challenging task. Absorption is mainly an issue when *determining* ζ-factors. When *applying* the ζ-factor method, absorption can be taken into account by using equation 2.19.

It should be noted that the general trends in figure 2.15 and the plot by Watanabe [2] are the same. However, there are differences in the absolute values of the critical thicknesses. The two plots are based on absorption coefficients from different databases.
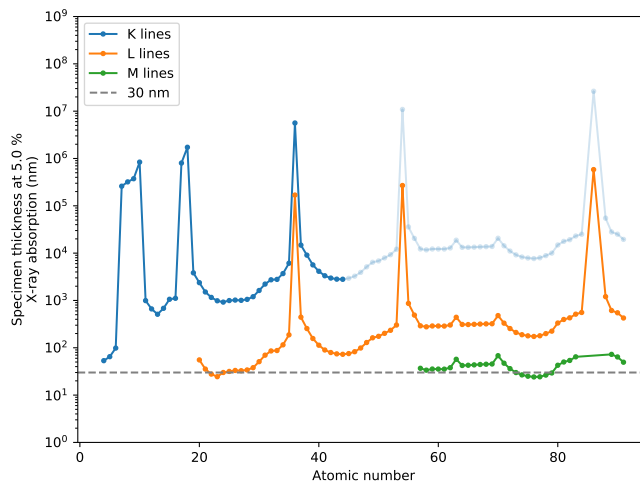
Figure 2.15: Plot of specimen thickness at 5 % self absorption, based on
Watanabe [2] and recreated in HyperSpy [5] using the database by Chantler
et al. [11]. The Python code to create the plot is attached in appendix E. The
shaded data points have energy higher than 20 keV, and are often difficult to
detect due to a limited detector efficiency (see section 2.3).

Channeling

As discussed by Watanabe [2] and De Graef [12, p. 418], in crystalline samples there
are channeling effects. When the sample is oriented close to a zone axis, then X-rays
of some elements may be favored over other elements due to the systematic atomic
positions in the crystal. This leads to offsets in the measured X-ray intensities. The
general advice is to avoid zone axes when doing quantitative EDX [3]. However, as
pointed out by Watanabe [2], in principle it is possible to incorporate "channeling
correction" if the crystal orientation is known exactly.

Shadowing

As discussed in section 2.3.3, the path to the detector can be blocked by the
specimen holder or the TEM grid at certain stage tilts. This effectively reduces
the detector solid angle $\Omega/4\pi$ (see equation 2.7). When determining ζ-factors, this
effect needs to be taken into account. In contrast, for the Cliff-Lorimer method,
the detector solid angle is canceled out and does affect the k-factor.

The shadowing effect on ζ-factors can be described mathematically. First, define
the active detector ratio ΔA is the ratio of the detector area which is not being

blocked. The ζ-factors can be expressed as a function of the active detector ratio,

$$\zeta(\theta) = \frac{1}{\Delta A(\theta)} \cdot \zeta_0, \qquad (2.21)$$

ζ_0 denotes the ζ-factor with no shadowing. As a simple approximation, ΔA depends linearly on the tilt angle. The entire detector is shadowed at angles below θ_1, and there is no shadowing at angles greater than an angle θ_2. Mathematically, equation 2.22 describes the approximate detector active ratio:

$$\Delta A(\theta) = \begin{cases} 0 & \theta \leq \theta_1 \\ \frac{\theta - \theta_1}{\theta_2 - \theta_1} & \theta_1 < \theta < \theta_2 \\ 1 & x \geq \theta_2 \end{cases} \qquad (2.22)$$

Actually, a similar approach has been used by Garmannslund to determine the shape of the EDX detector [13].

2.5.2.3 Estimating ζ-factors

It is tedious to determine the ζ-factor experimentally for every element in the periodic table. Instead, as devised by Watanabe [2], a more practical approach is possible: If ζ-factors are known accurately for some elements, then the remaining ζ-factors can be estimated by fitting to a model based on equation 2.7. For such a model, some unknown parameters need to be optimized. This typically includes a scaling factor to the ionization cross section and the thickness of layers in the EDX detector (see section 2.3.1). For the ζ-factor estimation to be representative, the known ζ-factor should have a reasonable spread in atomic number. ζ-factor estimation has been successfully demonstrated by Watanabe [2], who used the NIST SRM 2063a standard thin film sample as standard, containing Mg, Si, Ca, Fe and O [2]. Garmannslund [13] demonstrated the same approach, on the basis of ζ-factors from C, Al, Ga and As. Note that ζ-factor estimation must be performed for each X-ray family separately.

2.6 Crystallography and diffraction

The theory in this chapter is based on Kittel [14].

2.6.1 Crystallography

A crystal is a solid material whose microscopic constituents are arranged in a periodic manner. The counterpart of crystals is amorphous materials, which do not have any periodic structure at the microscopic level. All crystal structures can be described by *Bravais lattices*. A Bravais lattice is defined as all points which can be reached by a vector $\mathbf{R}$,

$$\mathbf{R} = m \cdot \mathbf{a_1} + n \cdot \mathbf{a_2} + o \cdot \mathbf{a_3} \tag{2.23}$$

The unit vectors $\mathbf{a_i}$ span the crystal structure, and they do not need to be orthogonal to each other. In three dimensions, there exist 14 distinct Bravais lattices. The repetitive units of crystals are called *unit cells*. Unit cells have the property that when placed in every lattice point of the Bravais lattice, they cover all of space, without leaving any voids. Four common Bravais lattices are shown in figure 2.16.
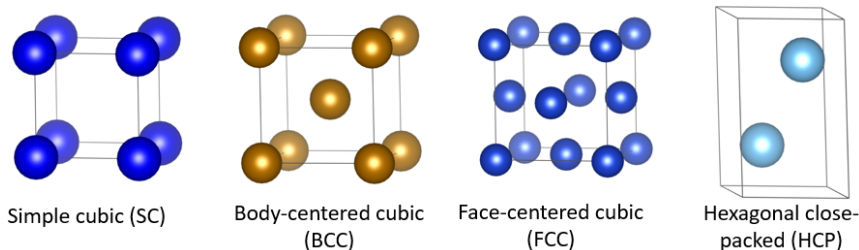
Figure 2.16: Conventional unit cell of common crystal Bravais structures.

Unit cells containing only one atom or molecule are called *primitive unit cells*. It is possible to define a primitive unit cell for every crystal structure. In many cases, it is convenient to define *conventional unit cells*. Conventional unit cells are typically non-primitive and cubic.

It is convenient to have notations for specifying coordinates, directions, and planes when dealing with crystalline materials. Consider a unit cell spanned by the vectors $\mathbf{a}$, $\mathbf{b}$ and $\mathbf{c}$. Crystallographic points are specified as fractions of the lengths of the unit cell vectors. For instance, the red spot in figure 2.17 has the coordinates $\frac{1}{2}10$. Negative indices are denoted by a bar over the number. Crystallographic directions are specified as vectors from the origin (denoted by O in figure 2.17) to a given point, surrounded by square brackets. In figure 2.17, the red vector is denoted $\left[\frac{1}{2}10\right]$. Crystallographic planes are denoted as (hkl), and they are orthogonal to the directions having the same coordinates. h, k and l are termed *Miller indices*. Miller indices can be found by looking at the intersection of the plane and the crystallographic axes, and taking the inverse. Fractions are eliminated by multiplying with the greatest common divisor. In the special case of cubic crystal systems,

many directions and planes are equivalent. Any pair of indices can be switched and indices can be replaced by their negative, and the resulting direction/plane is equivalent to the original direction/plane. The set of equivalent planes is called a *family of planes*, and denoted $\{klm\}$. Likewise, the set of equivalent directions is called a family of directions and denoted $\langle klm \rangle$.
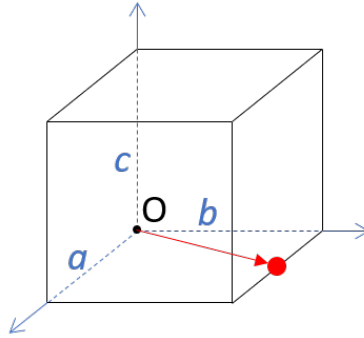
Figure 2.17

With each Bravais lattice point, there is an associated *basis*. Each basis consists of a number of atoms, and the atomic positions are specified relative to the lattice points.

Two common crystal structures are zinc blende (ZB) and wurtzite (WZ). Their conventional unit cells are shown in figure 2.18. The ZB structure is based on the FCC structure, with two atoms of a different type in basis. The second type is located in the tetrahedral sites relative to the first type. This corresponds to the atomic positions 000 and $\frac{1}{4}\frac{1}{4}\frac{1}{4}$. The WZ structure is based on the HCP structure. WZ crystals also have two different atoms in basis, with the second type on the tetrahedral sites of the first type. The ZB and WZ crystal structures are typical for semiconductor NWs. The GaAs NWs used in this project have phases of ZB and WZ (see section 3.1).
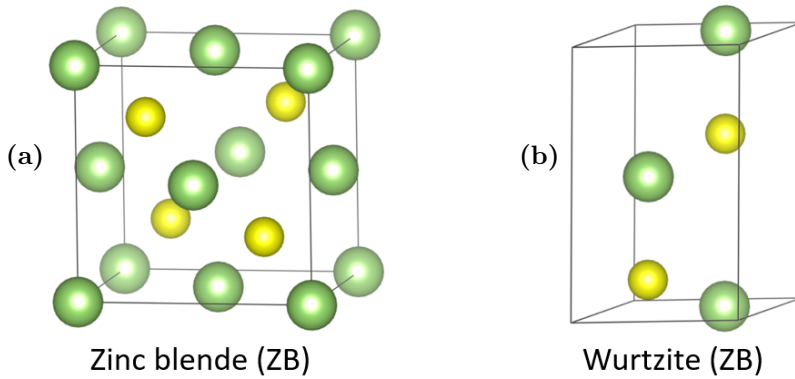
Figure 2.18: (a) ZB and (b) WZ crystal structures. The crystal structures have been acquired from Materials Project [15], and are visualized in VESTA [16]

2.6.2 Diffraction

When an electron wave hits atoms, electrons are scattered inelastically. In a crystal, this gives rise to diffraction patterns (DP). Diffraction happens when electron waves which are scattered at different planes interfere constructively. In figure 2.19, it can be seen that this happens when Bragg's diffraction condition is met,

$$n\lambda = 2d\sin(\theta) \tag{2.24}$$
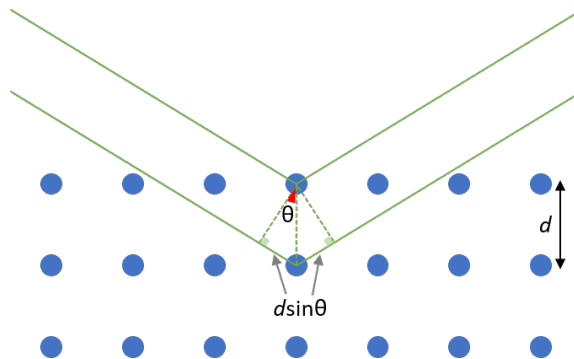
Figure 2.19: Diffraction happens when scattered electron waves interfere constructively. This happens when Bragg's diffraction condition is met (see equation 2.24).

In this section, only kinematic scattering is considered, which relies on the approximation that each electron undergoes only one scattering event. The more general

case of multiple scattering events per electron is considered in dynamical scattering theory.

Diffraction is closely related to the reciprocal space. The *reciprocal lattice* is defined by the reciprocal lattice vectors,

$$\mathbf{b_1} = 2\pi \frac{\mathbf{a_2} \times \mathbf{a_3}}{V} \qquad \mathbf{b_2} = 2\pi \frac{\mathbf{a_3} \times \mathbf{a_1}}{V} \qquad \mathbf{b_3} = 2\pi \frac{\mathbf{a_1} \times \mathbf{a_2}}{V} \tag{2.25}$$

$$V = \mathbf{a_1} \cdot \mathbf{a_2} \times \mathbf{a_3} \tag{2.26}$$

Any point in the reciprocal lattice can be reached by the reciprocal lattice vector,

$$\mathbf{G} = h \cdot \mathbf{b_1} + k \cdot \mathbf{b_2} + l \cdot \mathbf{b_3} \tag{2.27}$$

Consider an incoming electron with wavevector $\mathbf{k}$, which is scattered to a new wavevector $\mathbf{k'}$. When the electron is scattered, it undergoes a change in momentum $\Delta \mathbf{k} = \mathbf{k'} - \mathbf{k}$. The scattering intensity distribution depends on $\Delta \mathbf{k}$, and it is given by the scattering amplitude:

$$F = \int_V \rho(\mathbf{r}) e^{-i \Delta \mathbf{k} \cdot \mathbf{r}} dV \tag{2.28}$$

Using equation 2.28, it can be shown that scattering is at the maximum when the following condition is met:

$$\Delta \mathbf{k} = \mathbf{G} \tag{2.29}$$

In other words, diffraction spots appear when the momentum difference coincides with a reciprocal lattice point. This condition, which is called the Laue condition, is the reciprocal space equivalent of Bragg's diffraction condition. This is visualized in figure 2.20.

It is possible to use equation 2.28 to find the intensities of the diffraction spots of crystalline materials based on the unit cell structure. The *structure factor* of the basis is given by the equation below

$$S_{\mathbf{G}} = \sum_{j=1}^{N} f_j \exp\left(-i\mathbf{G} \cdot \mathbf{r}_j\right) \tag{2.30}$$
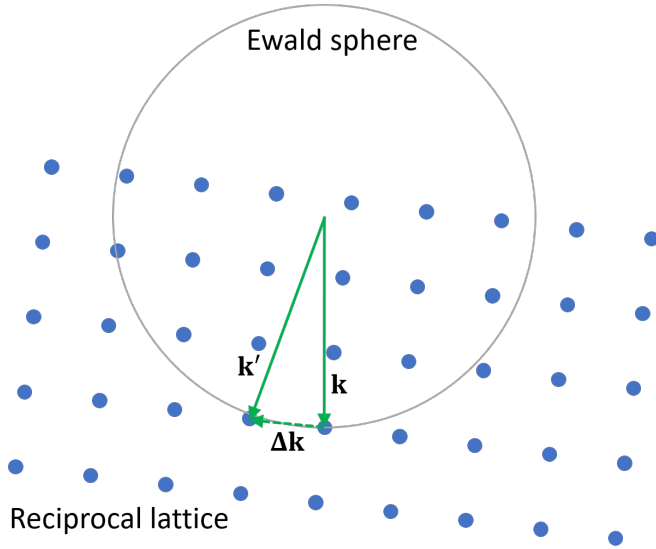
Figure 2.20: Visualization of the Laue diffraction condition. Diffraction spots appear when the momentum difference coincides with a spot in the reciprocal lattice.

$\mathbf{r}_j$ is the position of the j'th atom in the unit cell. f_j is the atomic form factor, which depends on the specific type of atom.

$$f_j = \int n_j(\boldsymbol{\rho}) \exp\left(-i\mathbf{G} \cdot \boldsymbol{\rho}\right) \tag{2.31}$$

$n_j(\boldsymbol{\rho})$ is the density distribution centered about the $j'th$ atom.

DPs can be seen in a TEM. When the beam is parallel and a limited area in real space is chosen for analysis, the resulting DP is called a selected area electron diffraction (SAED) pattern. However, when the beam is convergent, diffraction spots appear as discs. This type of diffraction is referred to as convergent-beam electron diffraction (CBED). If the sample is thick, then Kikuchi lines may appear due to dynamical scattering, both in SAED and CBED patterns.

In the real world, figure 2.20 is three-dimensional; the Ewald sphere is a real sphere, and the reciprocal lattice has three dimensions. This means that DPs in a TEM is the intersection of the reciprocal lattice with the Ewald sphere. SADPs usually contain many diffraction spots in the ZOLZ (zeroth order Laue zone), unlike in figure 2.20. This is because the radius of the Ewald sphere is very large, which is due to the low wavelength of electrons.

When the sample is oriented at a zone axis, the direct beam is at the center of

the ZOLS. The DP at the zone axis can then be used to determine the crystal orientation of the specimen. Figure 2.21 shows SADPs at different zone axes of ZB and WZ GaAs, which correspond to different crystal orientations.
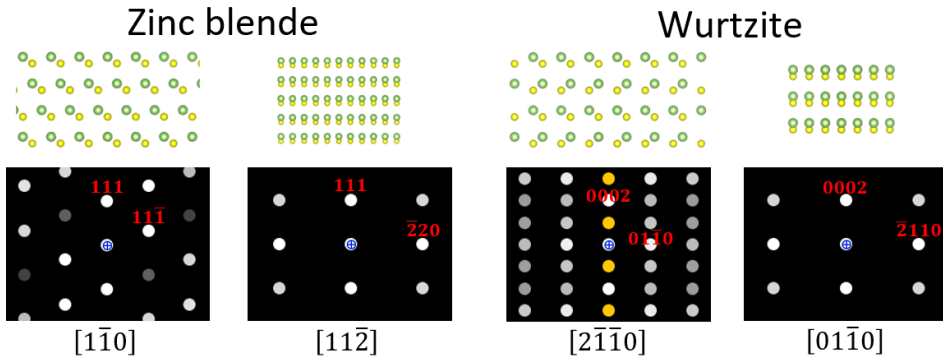
Figure 2.21: Crystal orientation and corresponding DP for ZB and WZ, at two different zone axes. The blue markers indicate the central beam. The yellow spots appear because of dynamical diffraction. The crystal structures have been acquired from Materials Project [15] and visualized in VESTA [16], and the DPs have been simulated in JEMS [17].

2.6.3 NW geometry

The nanowires (NW) studied in this project are shaped as prisms with a hexagonal cross section. Figure 2.22 shows crystallographic directions in the NWs, with respect to the ZB and WZ crystal structures.
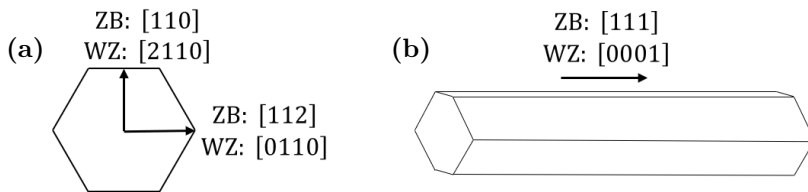
Figure 2.22: Crystallographic directions in the NWs studied in this project. (a) Hexagonal cross section. (b) Side-view of the NW.

Figure 2.23 shows a closer look at the hexagonal cross section. It is of interest to relate the width w to the thickness t of the NW, because then the projected width can be used to estimate the NW thickness. The sample thickness is necessary for determining the ζ-factor (see section 2.5.2.2).
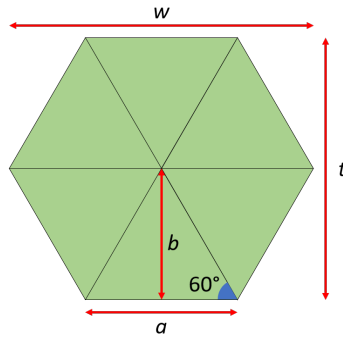
Figure 2.23: Hexagonal geometry

The hexagon consists of six equilateral triangles. From basic trigonometry, the relationship between the width and the height of an equilateral triangle is:

$$b = \frac{\sqrt{3}}{2}a \tag{2.32}$$

From the figure, it is obvious that $w = 2a$ and $t = 2b$. Thus, the NW width and thickness have the following relation:

$$t = \frac{\sqrt{3}}{2}w \tag{2.33}$$

It should be noted that the NW cross sections are not perfectly hexagonal. Thus, equation 2.33 is not an exact relation.

When *tilting* the sample by an angle θ, the effective thickness changes according to figure 2.24.
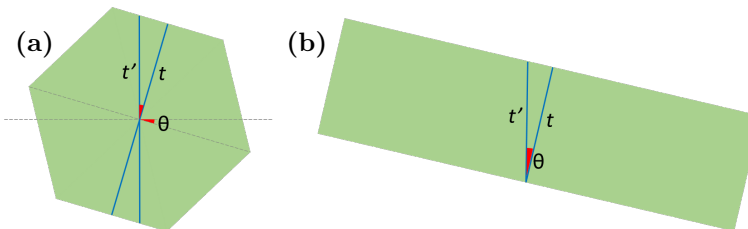
Figure 2.24: The effective thickness t' changes when tilting a NW. (a) Tilting against the [111] axis. (b) Tilting against the [112] axis.

In figure 2.24(b) (and any other thin film), the effective thickness t' can be found by simple trigonometry:

$$t'(\theta) = \frac{t}{\cos\theta} \qquad (2.34)$$

However, for the hexagonal structure in figure 2.24(a), equation 2.34 is only valid for $\theta \in [-30°, 30°]$. Furthermore, this relation repeats for angles outside of this range. The effective thickness can be defined recursively:

$$t'(\theta) = t'(\theta + n \cdot 60°), \qquad n \in \mathbb{Z} \qquad (2.35)$$

$$t'(\theta) = \frac{t}{\cos\theta}, \qquad \theta \in [-30°, 30°] \qquad (2.36)$$

Things get more complicated by the fact that the beam has a finite width, which reduces the effective thickness of the sample (see figure 2.25). Also, the beam width changes as the beam is subject to beam broadening in the sample. Furthermore, the concept of beam width is inherently inaccurate, as the beam in reality has an intensity distribution (which is approximately Gaussian). To account for these effects, it is reasonable to introduce an approximate beam width correction.
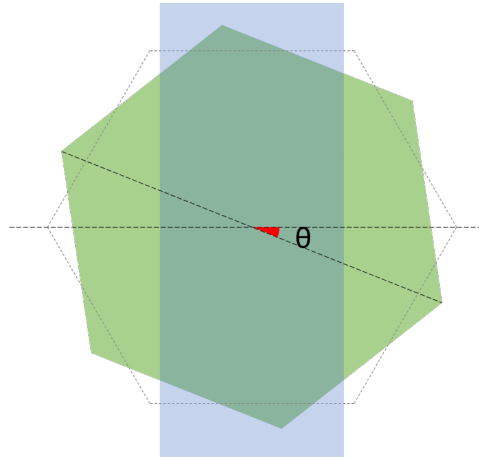
Figure 2.25: When the beam width increases, the effective NW thickness decreases.

In the beam width corrected expression, a parameter p has been introduced. At $p = 0$, the effective thickness is unaffected from equation 2.34, which corresponds to an infinitely small beam width. At $p = 1$, the effective thickness equals the NW thickness, independent on the tilt angle. This corresponds to a large beam width.

For $0 < p < 1$, the effective thickness scales linearly between the two edge cases. The mathematical expression is shown below,

$$t'(\theta) = t \cdot \left(\left(\frac{1}{\cos \theta} - 1 \right) \cdot (1 - p) + 1 \right) \tag{2.37}$$

Figure 2.26 shows the effective thickness when different corrections have been applied.
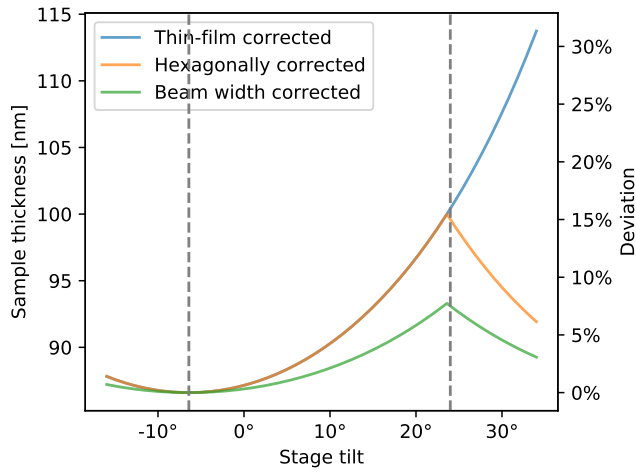
Figure 2.26: Effective thickness dependence on stage tilt. The blue graph corresponds to equation 2.34. The orange graph corresponds to equation 2.35. The green graph is beam width corrected (equation 2.37), with $p = 0.5$.

Chapter 3

Experimental

3.1 Material and specimen preparation

3.1.1 Self-catalyzed GaAs NWs with $GaAs_{1-y}Sb_y$ insert

The NWs consist of pure GaAs with ZB structure and growth direction [111] in the bottom part, an axial GaAsSb insert and pure GaAs with WZ structure and [0001] growth direction in the top part. The growth substrate was Si(111). A schematic is shown in figure 3.1. The NWs were grown with the vapor-liquid-solid (VLS) method in a Varian Gen II Modular MBE system by Mazid Munshi. The growth details are given in table 3.1 and described in detail in [18].

The NWs were removed from the substrate by scratching with a 60 µm diamond scraper at an angle of about 60° in isopropanol. A droplet with NWs was transferred to a 300 mesh Cu TEM-grid with a holey carbon film. The TEM-grid was plasma cleaned prior to some of the experiments, in order to avoid carbon contamination.

This sample was previously analyzed by Garmannslund [13] by EDX on a JEOL ARM 200F and also by Kauko et. al. [19] by HAADF STEM on a JEOL 2010F, and hence the known structure with several phases is an ideal test structure in the present study.
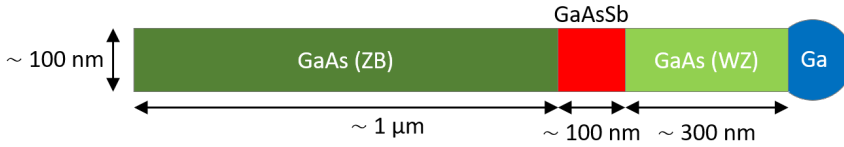
Figure 3.1: Schematic of self-catalyzed GaAs NWs with GaAsSb insert. The lengths are only indicative, and vary between the different NWs.

Table 3.1: Growth parameters for the self-catalyzed GaAs NWs with GaAsSb insert

	Ga flux [ML/s]	As$_2$ flux [Torr]	Sb$_2$ flux [Torr]	Time
GaAs, bottom part	0.7	4.2E-6	-	20 min
GaAsSb insert	0.7	4.2E-6	1.1E-6	1 min
GaAs, top part	0.7	4.2E-6	-	5 min

3.1.2 GaAs and GaSb particles

GaAs and GaSb particles were made from $\sim 5 \times 10$ mm pieces of a 111 GaAs and a 111 GaSb 2" wafer. The pieces was scrapped on the polished side with a 60 µm diameter diamond scriber. A 300 mesh Cu holey carbon TEM-grid with a drop of isopropanol was swiped over it. The preparation procedure is described in [20].

3.1.3 Self-catalyzed GaAs NWs with multiple GaAs/GaAs$_{1-y}$Sb$_y$ superlattices

The NW growth was done in a Veeco GEN 930 Molecular Beam Epitaxy (MBE) system at NTNU, Department of Electronic Structures. The growth of the NW cores followed a self-catalyzed VLS mechanism [21]. The process happened at a temperature of 625 °C

Initially, Ga was predeposited to form catalyst droplets. Then, a stem of GaAsSb was grown at the sites of the droplets. The stem causes the ZB phase to stabilize and increases the nucleation yield of NWs. Following this, six superlattices were grown. GaAs was grown in front of each superlattice so to as to separate the superlattices. Each superlattice was formed by growing alternating layers of GaAsSb and GaAs, up to a total of 10 GaAsSb quantum wells. After the growth of the superlattices, further nucleation was prevented by stopping the flux of Ga, causing the droplet to solidify. Lastly, an AlGaAs shell and a GaAs cap were grown in

order to prevent oxidation and passivate surface states. The final length of the NWs was approximately $10 \, \mu m$, and the thickness was about $400 \, nm$. A summary of growth parameters is shown in in table 3.2

Table 3.2: Growth parameters of the GaAsSb NWs. The steps marked 1 were repeated 6 times. The steps marked 2 were performed alternately.

	Ga flux [ML/s]	As$_2$ flux [Torr]	Sb$_2$ flux [Torr]	Al flux [Torr]	Time
Ga droplet formation	0.7	-	-	-	45 s
GaAsSb stem	0.7	2.5×10^{-6}	1×10^{-7}	-	1 min
GaAs spacer[1]	0.7	2.5×10^{-6}	-	-	5 min
10xGaAsSb[1,2]	0.7	1×10^{-6}	2.5×10^{-5}	-	20 s
9xGaAs barrier[1,2]	0.7	2.5×10^{-5}	-	-	20 s
Ga droplet consumption	-	1×10^{-5}	-	-	15 min
AlGaAs shell	0.2	1×10^{-5}	-	0.1	30 min
GaAs cap	0.2	1×10^{-5}	-	-	15 min

3.2 TEM experiments

3.2.1 Instrument details

For acquiring EDX data, a JEOL 2100 with a LaB$_6$ electron gun was used, operating at $200 \, keV$. The attached EDX detector was an Oxford X-Max^N 80T SDD, with a solid angle of $0.23 \, sr$. For TEM imaging and beam current measurements, an Orius^{TM} SC 200D CCD (Model 833) was used. This CCD is located above the viewing screen.

Additionally, a JEOL JEM-2100F with a Schottky field emission gun (FEG) was used, operating at $200 \, keV$. The attached EDX detector was an Oxford X-Max $80 \, mm^2$ SDD, with a solid angle of $0.23 \, sr$. For TEM imaging and beam current measurements, a Gatan 2k UltraScan CCD was used. This CCD is located below the viewing screen.

To verify the developed approaches and code, data from double corrected JEOL JEM-ARM 200F with a cold FEG was used, operated at $200 \, keV$. It had a JEOL Centurio EDX system and a nominal solid angle of $0.98 \, srad$. The beam current was measured via an ammeter in the Gatan image filter (GIF).

3.2.2 Experiment details

Table 3.3 summarizes the details of the TEM experiments performed on the GaAs NWs.

Table 3.3: Details on the TEM experiments performed on GaAsSb NWs. C.A. denotes "condenser aperture", and S.S. denotes "spot size".

ID	Instr.	Mode	Scan mode	Tilt axis	Live time	C.A.	S.S.
E1	2100	TEM	Spot	[112]	60 s	C1 (150 μm)	#5
E2	2100	TEM	Spot	[111]	60 s	C2 (70 μm)	#5
E3	2100	STEM	Spot	[111]	60 s	C3 (50 μm)	A2
E4	2100F	STEM	Spot	[112]	60 s	C3 (40 μm)	A3
E5	2100	STEM	Map	-	∼35 min	C3 (50 μm)	A2
E6	2100F	STEM	Map	-	∼15 min	C3 (40 μm)	A3

3.2.3 Beam current measurements

The beam current on the JEOL 2100 and the JEOL 2100F were measured using the attached CCD camera. The CCD count rate was measured using a DigitalMicrograph script, which was developed as part of this project. The script is described in detail in appendix B. In order to obtain the actual beam current, the CCD conversion efficiency must be known. The conversion efficiency of the JEOL 2100 CCD camera was found using a Faraday cup. The conversion efficiency of the JEOL 2100F CCD camera was known prior to this project.

3.3 Data processing

All data processing, analysis of EDX spectra and plotting has been done in Python (version 3.7.2) [22]. The open source library HyperSpy [5] has been used for processing of EDX data. TEM images have been analyzed in ImageJ and DigitalMicrograph.

The Python code for data analysis which has been developed, along with details on the implementation, is described in appendix C. The code itself is added as an attachment to this report. There are some main points to mention: All intensities have been found by model fitting (see section C.2.3). All EDX maps have been preprocessed by binning and principal component analysis (PCA) (see section C.2.4).

Chapter 4

Results

In this chapter, the experimental results are given. Section 4.1 gives the results of beam current measurements. Section 4.2 deals with the determination of ζ-factors, and how the ζ-factors are affected by experimental parameters. Finally, in section 4.3 the determined ζ-factors are applied to various datasets. In addition to the conventional ζ-factor method, alternative approaches (internal ζ-factors and tuned ζ-factors) are demonstrated.

4.1 Beam current measurements

This section presents results related to the measurement of the TEM beam current. Beam currents have been measured using the CCD screen attached to the TEM. In section 4.1.1, the CCD conversion efficiency is calculated. Section 4.1.2 shows line profiles of the electron beam when imaged on the CCD. Section 4.1.3 shows the beam current stability over time. Finally, section 4.1.4 tests the robustness of the CCD beam current measurements when settings are changed.

4.1.1 Conversion efficiency

The conversion efficiency of the Gatan Orius CCD camera on the JEOL 2100 has been measured for a range of spot sizes and condenser apertures. The beam current at each spot size and condenser aperture is shown in figure 4.1(a). The calculated conversion efficiencies are visualized in figure 4.1(b) and tabulated in figure 4.1. For all beam current measurements on the JEOL 2100, the overall average of 1.47 counts per electron was used (the reason for this is discussed in section 5.1.1).
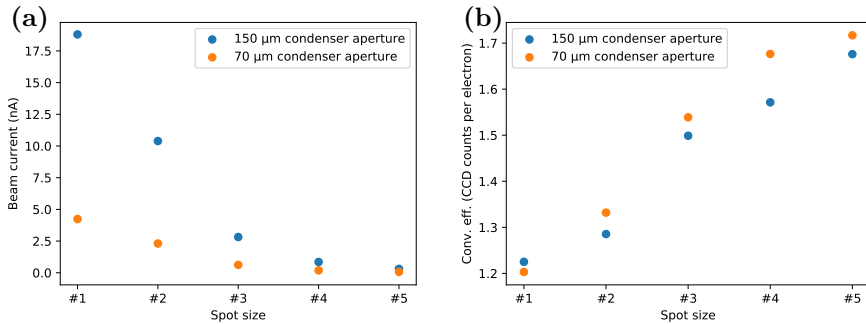
Figure 4.1: (a) Beam current as a function of condenser aperture and spot size. (b) Calculated conversion efficiencies. The measurements were done on the Gatan Orius CCD camera on the JEOL 2100.

Table 4.1: Tabulated conversion efficiencies of the Gatan Orius CCD camera on the JEOL 2100.

Spot size Cond. ap. diameter	#1	#2	#3	#4	#5
70 µm	1.20	1.33	1.54	1.68	1.72
150 µm	1.23	1.29	1.50	1.57	1.68

The conversion factor for the Gatan UltraScan CCD camera on the JEOL 2100F was measured by B. Soleim to be 4.96 counts per electron. Beam current measurements on the JEOL ARM-200f were measured by an ammeter within the GIF.

4.1.2 Line profiles of the electron beam

The beam current was measured by acquiring images of the beam on the CCD. This section shows examples of beam current images and corresponding line profiles. The line profiles give useful information because the intensity distribution of the beam may influence the quality of the beam current measurements.
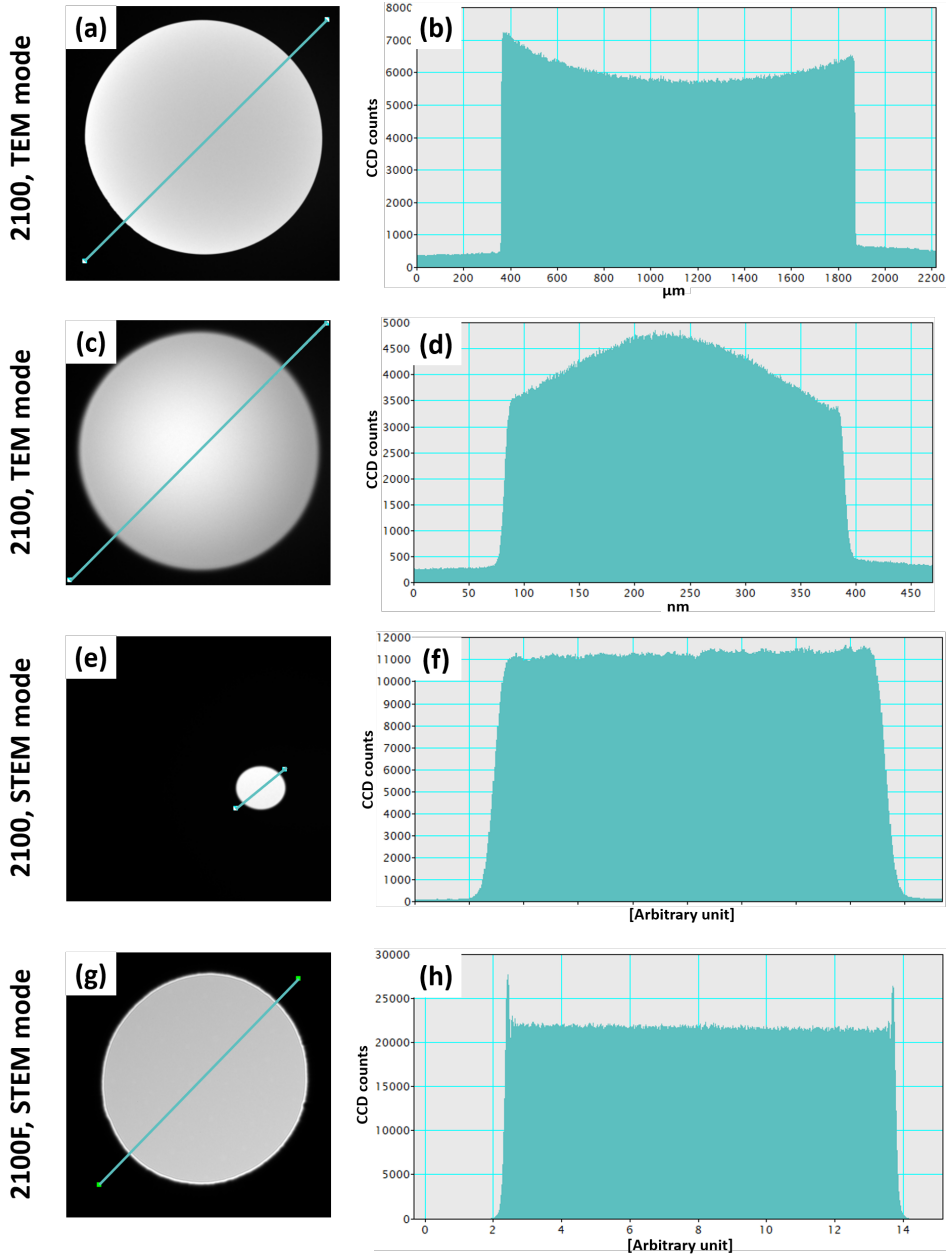
Figure 4.2: The left part shows beam current as measured on a CCD, using different microscopes and different configurations. The right part shows line profiles taken at the corresponding blue lines on the left-hand side. Additional experimental details are given here: (a)-(b): 150 µm condenser aperture, spot size 5. (c)-(d): Experiment E1. (e)-(f): Experiment E4. (g)-(h): Experiment E6. Condenser apertures and spot sizes for these experiments are given in table 3.3.

4.1.3 Beam current stability

The beam current on the JEOL 2100 was measured for about 40 min with an interval of about 5 s, to indicate the beam current stability. Figure 4.3 shows the results. Furthermore, the beam current was measured regularly during most EDX experiments in this project. Figure 4.4 shows examples of these measurements, to verify the beam current stability during a typical TEM session.
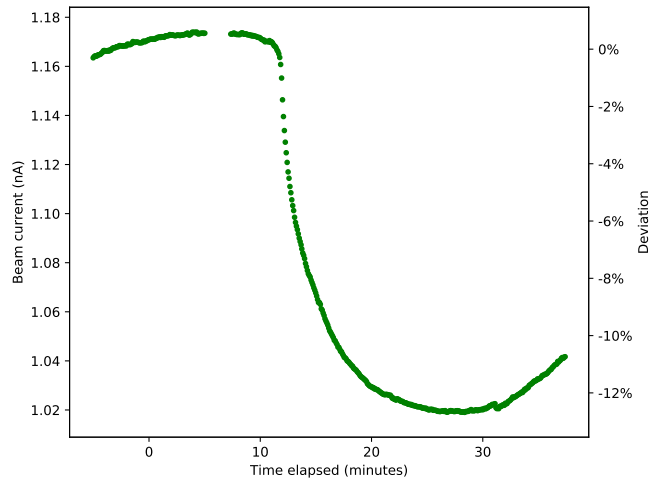
Figure 4.3: Beam current variation over time on the JEOL 2100. The 150 μm condenser aperture and spot size 1 were used. The deviation on the right axis is relative to the beam current in the beginning of the experiment.
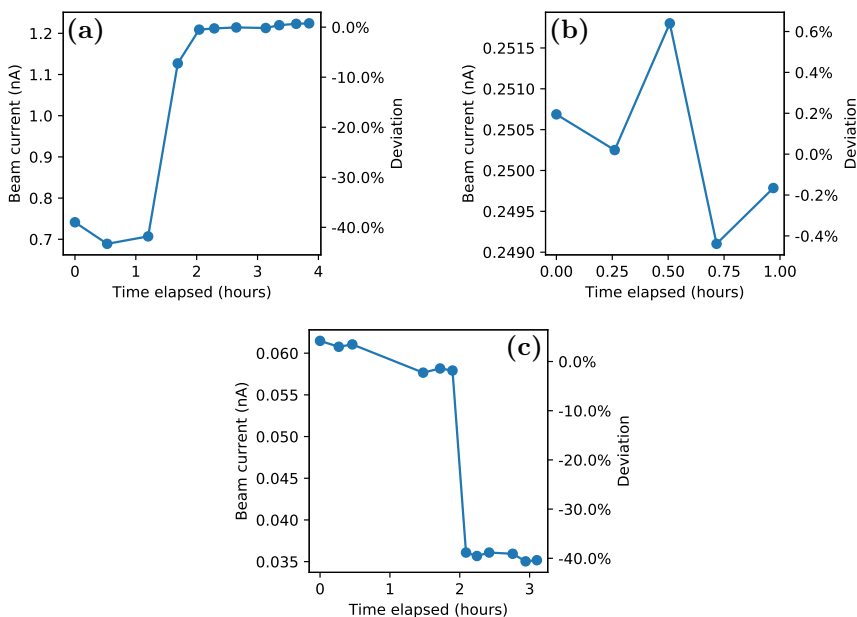
Figure 4.4: Beam current measurements of some experiments. (a) Experiment E1. (b) Experiment E2. (c) Experiment E3. The rapid $\sim 40\,\%$ changes in (a) and (c) are due to changes in aperture. The labels E1, E2 and E3 denote the experiment; details can be found in table 3.3.

4.1.4 Robustness of beam current measurements

There are some settings which have to be chosen when doing beam current measurements. The beam current should be independent of these settings. One parameter is the size of the beam on the CCD screen, measured as the ratio of the beam diameter to the frame width. For example, on figure 4.2(a) this ratio is ~ 0.9. The relation between beam current and beam size is shown in figure 4.5(a). Also, the beam current should be independent of the average CCD pixel counts. The relation between beam current and saturation level is shown in figure 4.5(b). Lastly, the beam current should be independent of the magnification. The relation between beam current and magnification is shown in figure 4.5(c).
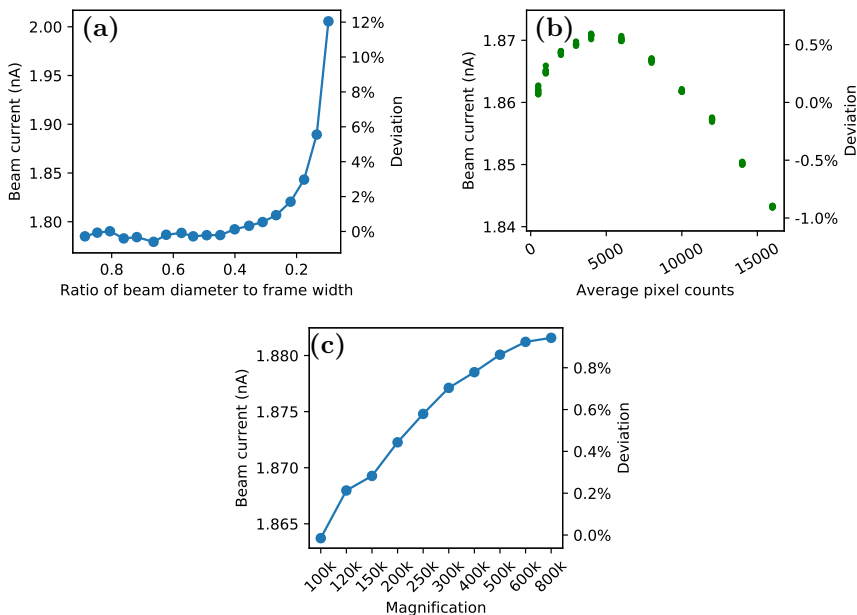
Figure 4.5: Measured variations in beam current on the JEOL 2100, as function of (a) beam size on the CCD screen, (b) average CCD counts per pixel and (c) magnification. The measurements were done with the 50 μm condenser aperture and spot size #1.

4.2 Effects on ζ-factor determination

This section shows $Ga\,K_\alpha$ and $As\,K_\alpha$ ζ-factors which have been determined on the JEOL 2100, and how these ζ-factors depend on various experimental parameters. For all measurements, GaAs NWs have been used as standards. Section 4.2.1 shows the effect of stage tilt, section 4.2.2 shows the effect of crystal structure and orientation, and lastly, section 4.2.3 shows the effect of TEM vs. STEM mode. To confirm the trends, similar measurements were done on another microscope: The JEOL 2100F. The results for the JEOL 2100F are summarized in section 4.2.4.

4.2.1 Dependence on stage tilt

ζ-factors of $Ga\,K_\alpha$ and $As\,K_\alpha$ have been found for a range of stage tilts angles. The result is plotted in figure 4.6. It is the α-tilt (also called x-tilt) which was varied. The NWs were oriented on the [110] zone relative to the ZB NW segment, and the stage was tilted with steps of approximately 5˚. Figure 4.7 shows BF-TEM images

of the NWs which were used, with red markers indicating the regions which were used for ζ-factor determination. The ζ-factor determination was done when tilting about different NW axes, and both for TEM and STEM mode. The NW tilt axis and the TEM mode are indicated on the figure. Thickness corrections were applied, as described in section 2.6.3.

Figure 4.6: ζ-factors of $Ga\,K_\alpha$ and $As\,K_\alpha$ as function of stage tilt. The ζ-factors have been calculated as an average of the ZB, WZ and pure Ga regions. The labels E1, E2 and E3 indicate the experiment; details can be found in table 3.3. Measurements done at zone axes are indicated by circles.
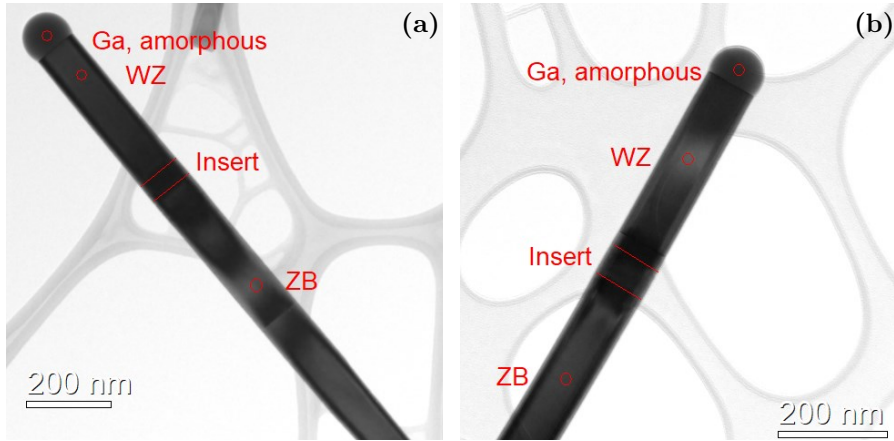
Figure 4.7: BF-TEM images of NWs used as standards for
ζ-factor-determination. The red circles indicate the regions which were used for
ζ-factor determination. (a) Experiment E1. (b) Experiment E2 and E3. Details
on the experiments are shown in table 3.3.

4.2.2 Dependence on crystal orientation and crystal structure

ζ-factors of Ga and As have been calculated both on and off zone axes and at
different crystal structures, to see whether this has any effect on the measurements.
Figure 4.8(a) and (b) show the result of two such experiments on the JEOL 2100.
The zone axes are labeled and indicated by vertical dashed lines. DPs of the ZB
and WZ segments when the NWs are oriented on zone are shown as inserts.
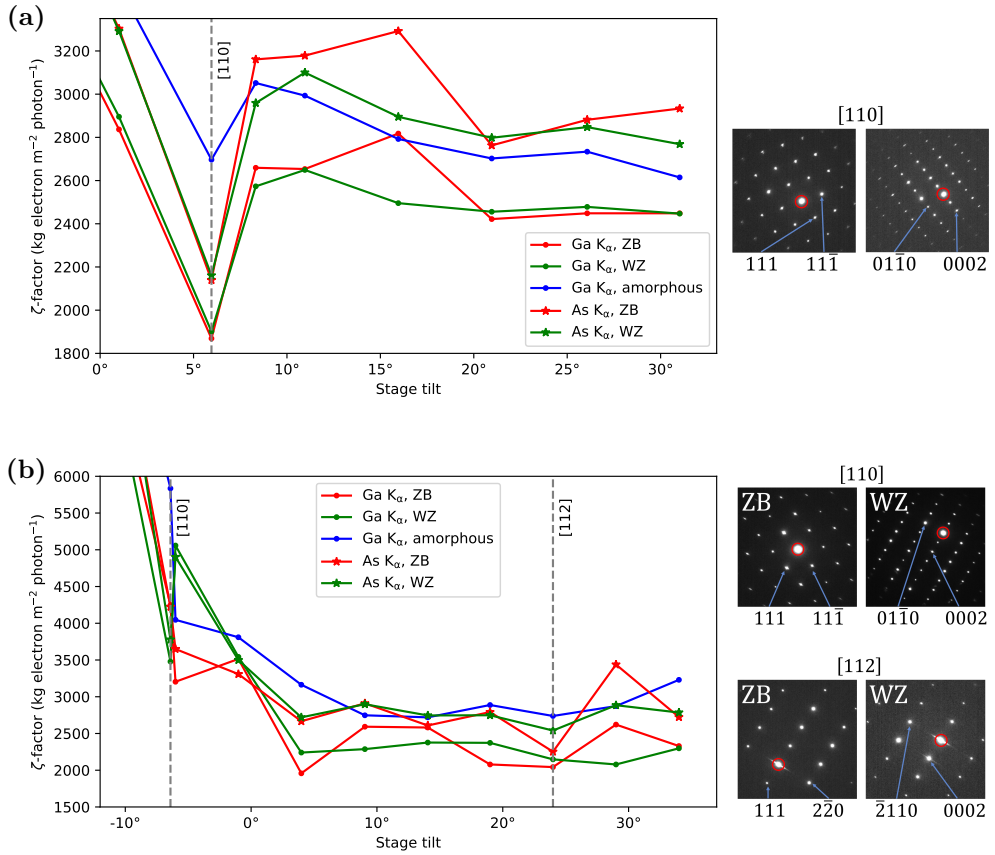
Figure 4.8: ζ-factor of $\mathrm{Ga\,K_\alpha}$ and $\mathrm{As\,K_\alpha}$ as function of stage tilt, calculated from different crystal structures and at different crystal orientations. The zone axes (relative to the ZB crystal) have been indicated by vertical dashed lines. Indexed DPs at each zone are shown as inserts. (a) Experiment E1. (b) Experiment E3. Details on the experiments can be found in table 3.3.

The effects of crystal orientation has been investigated in more detail by acquiring EDX maps of a GaAs NW close a zone axis. Details and experimental results can be found in appendix D.2.

4.2.3   TEM vs. STEM mode

ζ-factors were measured both in TEM and STEM modes, as the operation mode could affect the ζ-factor determination. The measurements were done using the exact same NW during the same TEM session. Figure 4.9 shows the calculated ζ-factors as function of stage tilt.
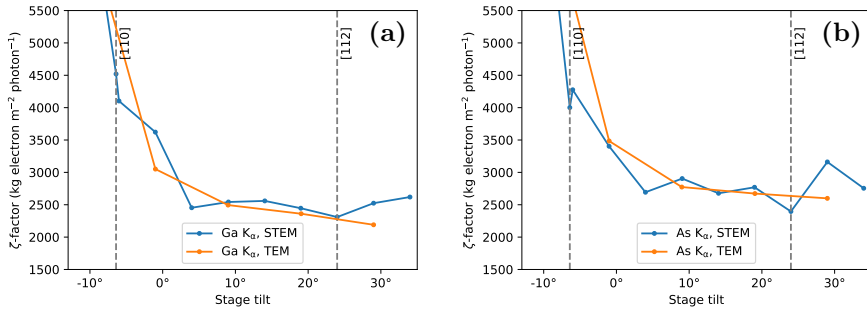
Figure 4.9: ζ-factor as function of stage tilt for STEM mode vs. TEM mode. (a) ζ-factor for $Ga\,K_\alpha$. (b) ζ-factor for $As\,K_\alpha$. The ζ-factors have been calculated as an average of the ZB, WZ and pure Ga regions. Zone axes are indicated.

4.2.4 Different microscopes

Until this point, all measurements have been carried out on the JEOL 2100. To see whether the effects and trends are general, similar measurements were performed on the JEOL 2100F as well. All measurements were done in STEM mode, when tilting against the [112] axis of the GaAs NW. Figure 4.10 shows the effect of stage tilt on the ζ-factors (corresponding to figure 4.6 for JEOL 2100). Figure 4.11 shows the effect of crystal structure and crystal orientation (corresponding to figure 4.8 for JEOL 2100).
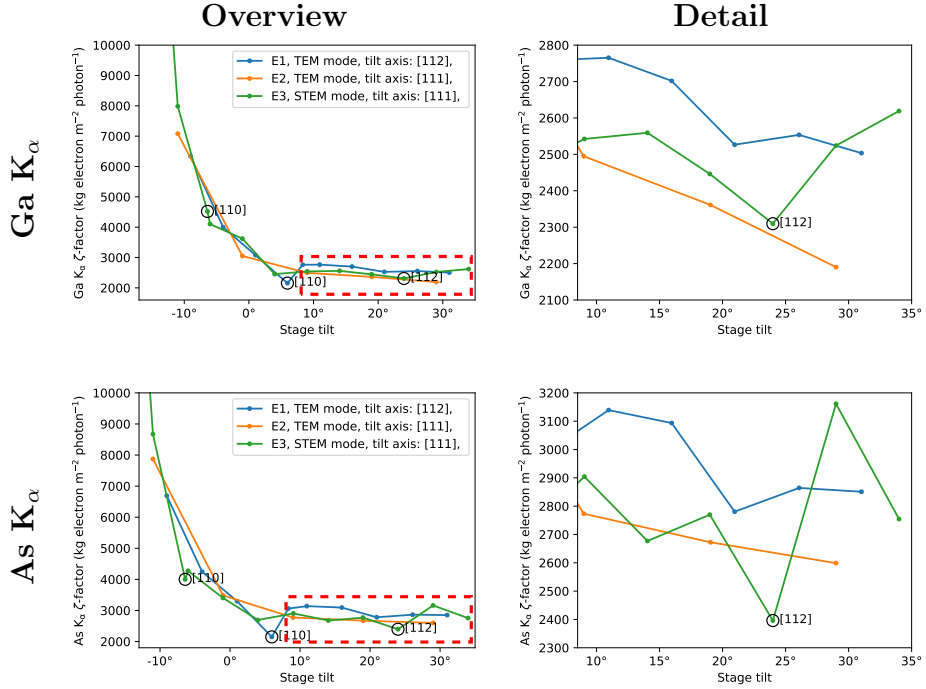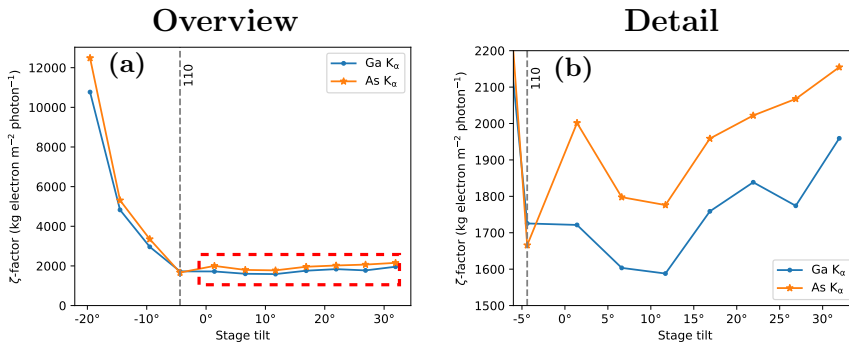

Figure 4.10: ζ-factors of $Ga\,K_\alpha$ and $As\,K_\alpha$ as function of stage tilt. The ζ-factors have been calculated as an average of the ZB, WZ and pure Ga regions.
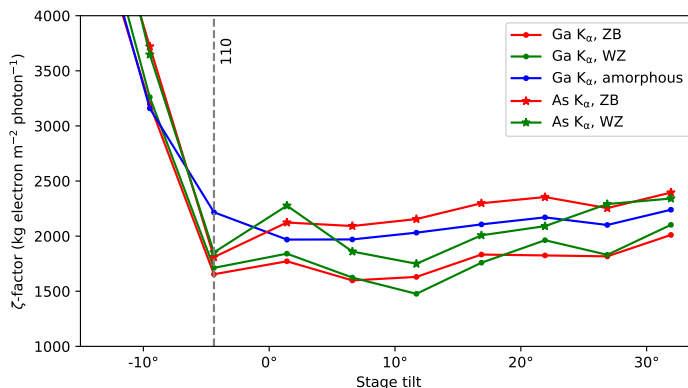
Figure 4.11: ζ-factor of $\mathrm{Ga\,K_\alpha}$ and $\mathrm{As\,K_\alpha}$ as function of stage tilt, calculated from different crystal structures and at different crystal orientations. The zone axes have been indicated by vertical dashed lines.

4.3   Applying the ζ-factor method

Using the ζ-factors calculated from GaAs NWs in section 4.2 (referred to as *tabulated* ζ-factors), the ζ-factor method has been applied to various datasets and compared with the commonly used Cliff-Lorimer method. Tabulated ζ-factors have been found using the approach described in section 5.3.6. k-factors used in the Cliff-Lorimer method were specified by the commercial EDX software AZtec. The composition of all datasets are known, which makes it possible to assess whether the tabulated ζ-factors are well calibrated, and how they compare with the Cliff-Lorimer k-factors. In addition to the tabulated ζ-factors, alternative approaches are demonstrated. These approaches are described in further detail in section 5.4.2 and 5.4.3. As a summary, *internal* ζ-factors are calculated from an area in an EDX map with known composition, and then applied to other areas on the same EDX map with unknown composition. *Tuned* ζ-factors are found by utilizing knowledge on the overall composition of the sample. Table 4.2 shows an overview of the samples which have quantified, and which quantification techniques have been applied to them. Furthermore, table 4.3 and 4.4 lists all k-factors and ζ-factors which have been used for quantification.

Note that all ζ-factors have been calculated in terms of weight percentages, which is the convention in the EDX literature as well as in HyperSpy. In the final step, the compositions have been converted to atomic percentages.

Table 4.2: Overview of samples which have been quantified in this section, and which quantification methods have been applied to each sample.

	Cliff-Lorimer	Tabulated ζ-factors	Internal ζ-factors	Tuned ζ-factors	Section
GaAs particles	✓	✓			4.3.1
GaAs NW, WZ region	✓	✓	✓		4.3.2
GaAs NW, WZ, ZB and GaAsSb insert	✓	✓	✓	✓	4.3.3
GaSb particles	✓	✓		✓	4.3.3
GaAsSb NW, external dataset	✓		✓	✓	4.3.3

Table 4.3: Overview of k-factors and ζ-factors used for quantification. k-factors are unitless, while ζ-factors have unit kg electron m^{-2} photon^{-1}.

	JEOL 2100			JEOL 2100F		
	$Ga\,K_\alpha$	$As\,K_\alpha$	$Sb\,L_\alpha$	$Ga\,K_\alpha$	$As\,K_\alpha$	$Sb\,L_\alpha$
k-factors	1.346	1.502	1.948	1.444	1.636	1.935
Tabulated ζ-factors	2393	2848		1628	1963	
Internal ζ-factors	2505	2987		1958	2342	
Internal and tuned ζ-factors	2521	3042	4800	1964	2325	3070

Table 4.4: ζ-factors used for quantification on the JEOL ARM-200F. ζ-factors have unit kg electron m^{-2} photon^{-1}.

	JEOL ARM-200F		
	$Ga\,K_\alpha$	$As\,K_\alpha$	$Sb\,L_\alpha$
Internal and tuned ζ-factors	5656	7128	10500

4.3.1 Quantification by tabulated ζ-factors

ζ-factors determined for the JEOL 2100F (referred to as *tabulated* ζ-factors) were verified by applying the ζ-factor method to GaAs particles with known composition.

Quantification was done both in spot mode and for an EDX map, and the results are shown in figure 4.12(a) and (b), respectively. For reference, figure 4.13 shows one of the particles which was quantified.
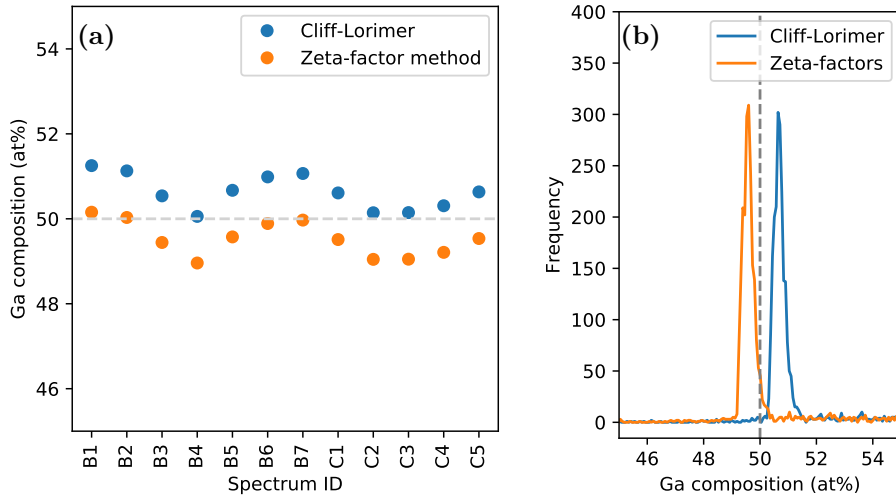
Figure 4.12: Calculated Ga composition of multiple GaAs particles. (a) shows the calculated compositions from multiple spectra taken at different sites. The letters denote the site, while the numbers denote separate spectra taken at the given site. (b) shows the composition calculated from an EDX map of a GaAs particle as a histogram.

Figure 4.13: HAADF-STEM image of a GaAs particle acquired on the JEOL 2100F, from which single EDX spectra were taken. The labeled spots on the particles correspond to the labels in figure 4.12.

4.3.2 Quantification by internal ζ-factors

An EDX map was acquired on the ZB and WZ regions of a GaAs NW. The WZ region was quantified using tabulated ζ-factors, and compared with the Cliff-Lorimer method. The NW was confirmed to be off zone, so as to ensure there are no crystal orientation effects, which may cause an offset in the measurements (see section 4.2.2). An alternative approach to tabulated ζ-factors was demonstrated: Internal ζ-factors. Internal ζ-factors were calculated from the ZB region of the same NW. The internal ζ-factors were taken from the same NW and the same EDX scan as the WZ area, which means that any effect of thickness, beam current and shadowing are canceled out. The various quantification methods are compared in figure 4.14. Separate experiments were performed on the JEOL 2100 and the JEOL 2100F.
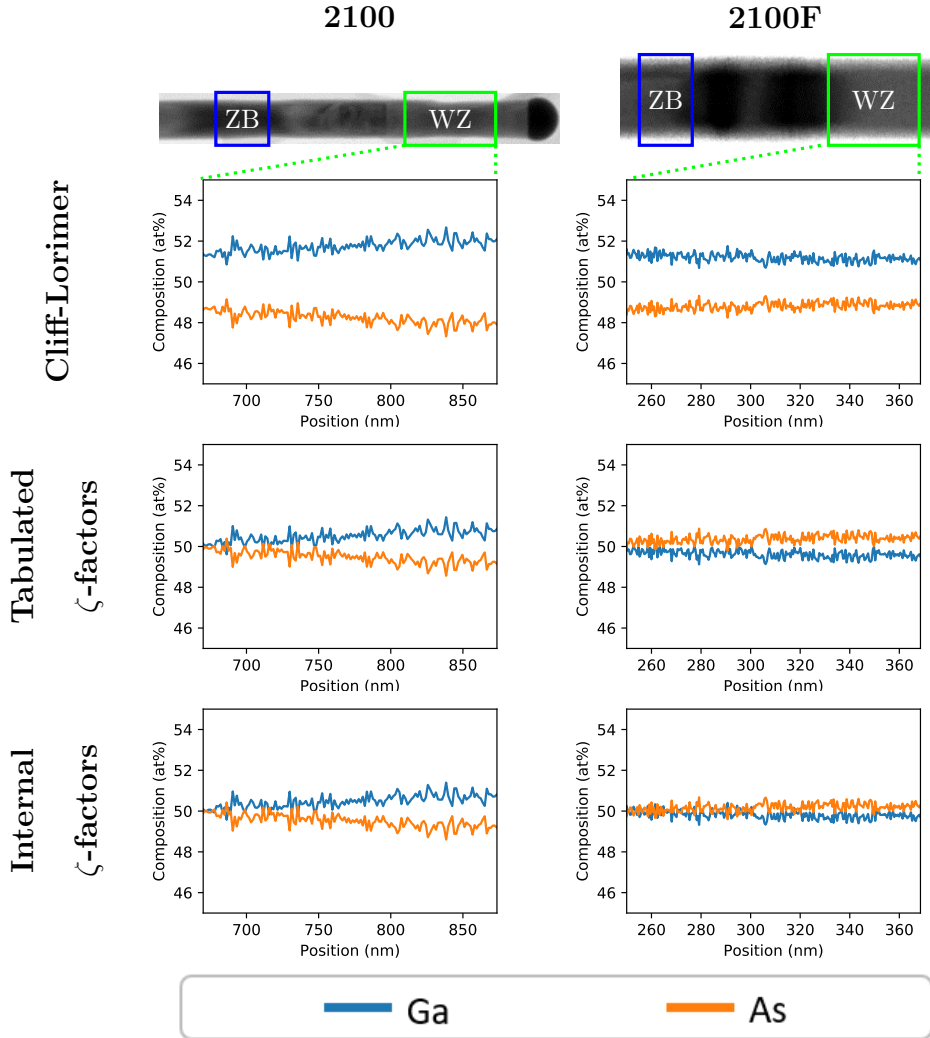
Figure 4.14: The WZ region of GaAs NWs (shown by green rectangles) have been quantified by the ζ-factor method and the Cliff-Lorimer method. Both tabulated ζ-factors and internal ζ-factors have been used. The internal ζ-factors are acquired from the ZB region (shown by blue rectangles).

4.3.3 Quantification by tuned ζ-factors

In section 4.3.2, only the WZ segment of the GaAs EDX map was quantified. This section deals with quantification of the entire EDX map, including both the ZB and WZ GaAs segments, as well as the GaAsSb insert. For this case, the tabulated ζ-factors could not be used, as the $\mathrm{Sb\,L_\alpha}$ ζ-factor has not yet been calculated from

standards. Instead, an alternative approach termed ζ-*factor tuning* was used. The Sb L_α ζ-factor was tuned so as to satisfy the condition that the Ga composition should be 50 % at all positions, including the GaAsSb insert. The Sb ζ-factor is tuned so as to satisfy this condition. This approach is described further in section 5.4.3. The Ga K_α and As K_α ζ-factors were determined internally; the Ga K_α ζ-factor from the total EDX map, and the As K_α ζ-factor from the ZB and WZ regions (see figure 4.15). The tuned ζ-factor approach is compared with the Cliff-Lorimer method in figure 4.16.
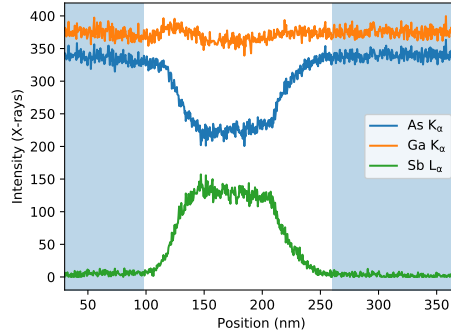
Figure 4.15: Raw intensities of the EDX map of a GaAs NW, as function of position on the x axis. The blue region was used to determine the As K_α ζ-factor internally, and the complete region was used for determining the Ga K_α ζ-factor internally.
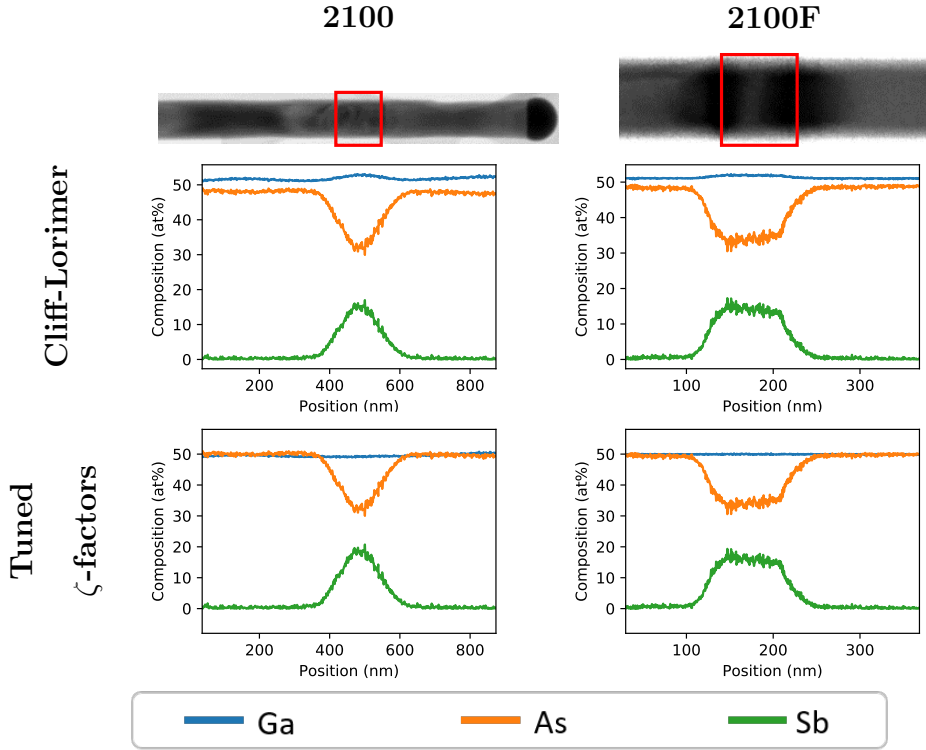
Figure 4.16: EDX maps of GaAs NWs with a GaAsSb insert were quantified by the ζ-factor method and the Cliff-Lorimer method. As an experimental $Sb\,L_\alpha$ ζ-factor is not currently known, an alternative approach termed ζ-factor tuning was used to estimate the $Sb\,L_\alpha$ ζ-factor (see section 5.4.3).

The combination of the internally determined $Ga\,K_\alpha$ and $As\,K_\alpha$ ζ-factors and the tuned Sb ζ-factor seemed to work well qualitatively in quantifying GaAs NWs with GaAsSb insert. However, the Sb composition at the insert is not known, and thus, it is still not known whether the set of ζ-factors are correct. In order to test the validity of the ζ-factors, they were used to quantify GaSb particles with a known 50-50% composition. EDX was performed for a number of different GaSb particles with different orientation and shape, and multiple spectra were acquired for each particle. The experiment was performed both on the JEOL 2100 and the JEOL 2100F. Furthermore, and EDX map was performed on the JEOL 2100F. The ζ-factors were compared with the commonly used Cliff-Lorimer method. The results of the quantification are shown in figure 4.17. For reference, figure 4.18 shows some of the GaSb particles which were quantified.
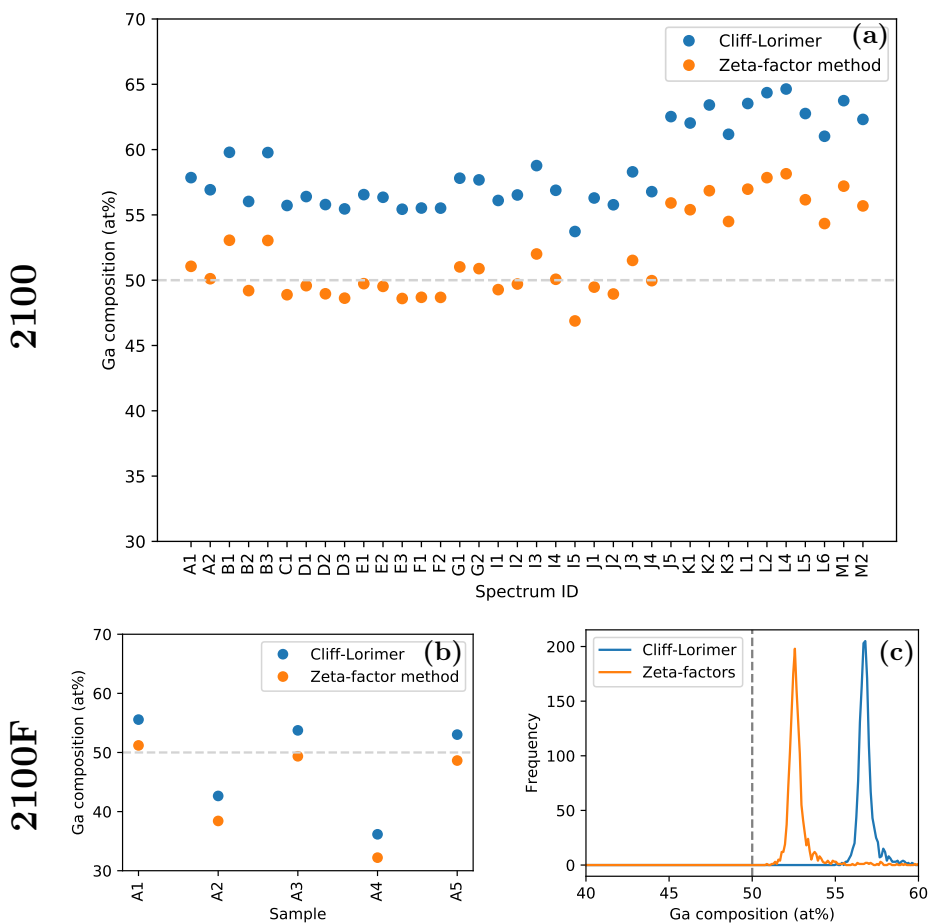
Figure 4.17: Calculated Ga composition of multiple GaSb particles. The compositions were found using the Cliff-Lorimer method and the ζ-factor method; the latter using a Sb L_α ζ-factor tuned to an internally determined Ga K_α ζ-factor. (a) and (b) were taken by EDX spot mode. The letters denote different GaSb particles, and the numbers denote separate spectra taken at the given particle. (c) shows the composition calculated from an EDX map of a GaSb particle as a histogram.
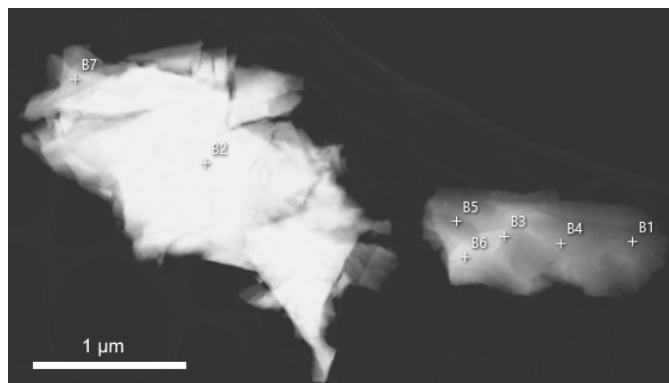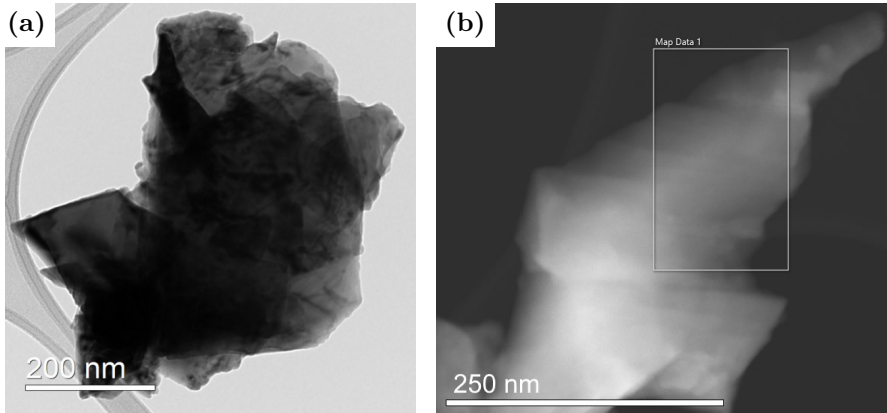
Figure 4.18: (a) BF-TEM image of a GaSb particle acquired on the JEOL 2100, labeled C on figure 4.17(a). (b) HAADF-STEM image of a GaSb particle acquired on the JEOL 2100F, from which the EDX map at figure 4.17(c) was taken. The EDX map area is indicated on the figure.

In order to test the generality of the approach of ζ-factor tuning, the procedure was applied to an entirely different dataset, acquired on a JEOL ARM-200F. The leftmost 30 nm were used to determine the $Ga\,K_\alpha$ and $As\,K_\alpha$ ζ-factors internally, and the $Sb\,L_\alpha$ ζ-factor was tuned to the Ga compositional profile, which is known to be 50 % everywhere. Figure 4.19 shows the results.
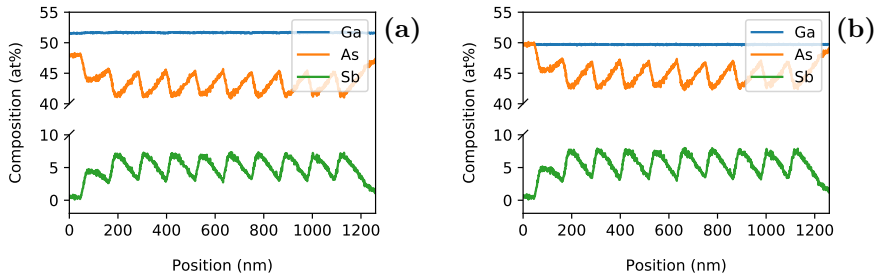
Figure 4.19: Compositional profiles of a GaAsSb NW, calculated by (a) Cliff-Lorimer and (b) the ζ-factor method with tuning of the $Sb\,L_\alpha$ ζ-factor.

One of the advantages of the ζ-factor method is the fact that the specimen mass-thickness can be calculated at the same time as the composition (see equation 2.17). To demonstrate this advantage, a thickness map from the EDX map at figure 4.18(b) has been attached in figure D.5

Chapter 5

Discussion

In this chapter, the results presented in the previous chapter are discussed and linked together. The first part deals with beam current measurements, which is a crucial part of implementing the ζ-factor method. The second part deals with ζ-factor determination. ζ-factors have been determined through a series of measurements, and the robustness of the ζ-factors is discussed by taking into accounts effects such as stage tilt and crystal orientation. Then, errors in the ζ-factor are discussed, and values for ζ-factors are given. Lastly, the ζ-factor method has been applied to various samples using the JEOL 2100 and JEOL 2100F microscopes, and the results are compared with Cliff-Lorimer to see whether the ζ-factor method gives better accuracy. Furthermore, alternative approaches to conventional, tabulated ζ-factors are discussed.

5.1 Beam current measurements

Beam current measurements are essential for the ζ-factor method. The beam current is used to calculate the electron dose, which is necessary when determining ζ-factors experimentally (equation 2.20) and when finding the sample mass-thickness (equation 2.17). However, the beam current cannot be measured directly on all commercial TEMs, including the JEOL 2100 used in this project. Instead, an alternative method has been used: The beam current has been measured indirectly through the CCD. In order to make beam current measurements consistently and conveniently, a DigitalMicrograph script has been created as part of this project. All beam currents in this project have been measured through this script. The script is attached in section B, along with instructions on how to use it and details on how it works.

Using this method, the beam current can still not be measured at the same time

as EDX is performed. This is a fundamental limitation of any approach which does not measure the beam current in situ. The developed method is, however, a practical way of measuring beam current compared with alternatives such as incidental measurements by a Faraday cup, and the method should enable frequent monitoring of the beam current.

5.1.1 Conversion efficiency

The output of a CCD measurement is the total number of CCD counts per second. In order to calculate the beam current (electrons per second), it is necessary to find the conversion efficiency of the CCD camera, i.e., the average number of counts one electron produces. The conversion efficiency of the Gatan Orius CCD attached to the JEOL 2100 has been calculated for different beam currents, by changing the spot size and condenser aperture. A Faraday cup was used to measure the beam current. Figure 4.1(a) shows how the beam current varies with spot size and condenser aperture. The resulting conversion efficiencies are shown in figure 4.1.

Ideally, the conversion efficiency should be a constant, independent on beam current. However, figure 4.1(b) shows a strong dependence on spot size and a weak dependence on condenser aperture. The conversion factors vary from 1.2 to 1.7, that is, almost $\pm\,20\,\%$ as the spot size is varied. The Gatan Orius CCD datasheet specifies the conversion factor to be in the range of 1-1.5 counts per primary electron [23]. The documentation does not state the conditions for which the count rate varies.

The dependence of conversion efficiency on spot size and condenser aperture is unphysical. There might be issues with one or more of the corrections performed on the CCD camera. Figure 4.2(a) and (b) show a closer look on one of the beam current images acquired by the CCD camera, taken when the CCD conversion factor was calculated. Note the scale of the beam width, which is in the order of millimeters. The profile is not what is expected of a Gaussian beam, and this may be an artifact of corrections performed on the CCD camera. Furthermore, there is non-zero background noise outside of the beam, which indicates issues with dark correction. This is problematic if the corrections depend on exposure time. During the experiment, the exposure time was varied between 0.17 s to 5 s, in order to utilize the full capacity of the camera.

Figure 4.2(c) to (h) show CCD images and profiles from beam current measurements acquired during EDX sessions. The profiles are very different from figure 4.2(b), which was used for calibration. The difference in the profile is probably related to the convergence angle of the beam; when performing EDX, the beam is converged to a tiny spot, and the brightness is not changed when measuring beam current. The beam convergence is indicated by the scale of the beam width, which is much smaller.

Due to the difference in line profiles between the calibration and the actual experiments, the calibration data in table 4.1 does probably not correspond well to the measurements. For this reason, it has been chosen to use a fixed value for the conversion efficiency, no matter the spot size and condenser aperture. The chosen value is the average of all measurements, shown in table 5.1. For the future, it is suggested to perform calibration of the CCD using a similar beam convergence angle as in the actual experiments. If updated calibration data are available, the results in this report can easily be updated. The conversion efficiency is a simple parameter in the Python scripts used for analyzing the ζ-factors, and can easily be changed. Furthermore, all beam current measurements in this study have been done using similar spot sizes and condenser apertures. This means that the measurements are correct relative to each other, and thus, findings in this report should not be affected by the conversion efficiency.

Table 5.1: Calculated conversion efficiency of the Gatan Orius CCD attached to the JEOL 2100.

Conversion efficiency (CCD counts per primary electron)
1.47

As a side note, the original CCD image has been saved for all beam current measurements. This is done automatically by the DigitalMicrograph script described in appendix B. Thus, it is possible to make corrections to the measured beam currents if issues with image corrections are discovered.

5.1.2 Beam current stability

The JEOL 2100 microscope has a LaB_6 thermionic emission electron gun. According to Williams and Carter [3, p. 77], thermionic sources should vary less than $\pm$ 1 %/hour. In this section, the real beam current variation on the JEOL 2100 microscope is discussed.

The beam current was measured for a period of about 40 min and for intervals of about 5 s, using the DigitalMicrograph script described in section B. The beam current as function of time is plotted in section 4.1.3. The plots show that the beam current changes smoothly with time over small ($\sim$ 5 s) time intervals. Most variations on this length scale are less than $\pm$ 0.01 %. However, it is observed that the beam current can change more drastically over larger time periods. In the middle of the experiment, the beam current was reduced with about 10 % during a period of 5 min. The large variation may be related to changes in the environment, such as the liquid nitrogen tank attached to the microscope.

Figure 4.4 shows the measured beam current variation in a range of experiments

performed during this project. In most experiments, the beam current variation is in the order of $\pm\,1\,\%$/hour. This is in line with the expected variation for LaB_6 sources as stated above. There are two rapid changes in the beam current of about $40\,\%$, in figure 4.4(a) and (c), respectively. However, these were caused by changes to the aperture settings and not by beam instability.

As a conclusion, the beam current is generally stable; however, some deviations may occur. This means that the beam current should be measured as frequently as possible. If EDX is performed in spot mode and the beam current is measured with an interval of, say, ten minutes, then the measured beam current is most likely accurate. On the contrary, if EDX maps are acquired and the beam current is measured on an hourly basis, then the beam current estimate may be more inaccurate. Note that the JEOL 2100F, which has FEG, is expected to have a more stable beam current.

5.1.3   Effect of various parameters on CCD measurements

Section 4.1.4 shows how various parameters affect the beam current. These parameters are often changed when performing beam current measurements, and ideally, they should not affect the measurement. In this section, it is discussed whether these parameters have any significant impact on the beam current measurements.

According to figure 4.5(a), the measurement is constant up to $\pm\,1\,\%$ when the beam diameter is greater than $30\,\%$ of the frame width. When the beam is smaller, the measurement quickly starts to deviate. Accordingly, the beam current should be as large as possible on the CCD screen, but of course, it should not extend it. Note that for the smallest beam sizes, the exposure time is only a few ms. Thus, the capacity of the camera is poorly utilized (both in terms of detector area and exposure time), which may explain the deviation.

Figure 4.5(b) shows how the beam current varies with CCD saturation level. There seems to be a correlation between these quantities. However, the correlation is very weak; in the same order as random fluctuations in the beam current. This means that the detector response is approximately linear. However, when the CCD saturation is small, then the *spread* in the beam current measurements is generally larger. For this reason, it is advisable to use a high CCD saturation level.

Figure 4.5c shows how the beam current varies with magnification. Again, there seems to be a weak correlation, which is in the same order as random beam current fluctuations. Even though the correlation is small, it is advisable to use a constant magnification when performing beam current measurements.

To ensure beam currents measurements are performed consistently, a list of suggested guidelines have been made. The list is shown below:

- The beam should cover most of the screen.

- The magnification should have a constant value throughout the measurements, typically 250kx.

- The average pixel counts should have a constant value throughout the measurements, typically between $50\,\%$ and $100\,\%$ of the maximum pixel counts. This is enforced by the beam current script.

- The beam should be focused on a hole on the film, and it should be in a reasonable distance from any material.

- The hole should be in reasonable proximity of the material of interest.

To conclude the beam current discussion, a procedure for measuring beam current has been developed and verified. The procedure includes a script for measuring beam current along with suggested guidelines for performing the measurements. This allows for consistent and frequent measurements of beam current, which subsequently improves the accuracy of the ζ-factors. The beam current has been verified to be stable enough for accurate ζ-factor determination; however, the beam current should still be regularly monitored. There are still issues with finding the correct CCD conversion efficiency for different spot sizes and condenser apertures. To ensure measurements are correct relative to each other, they need to be taken at the same spot size and condenser aperture. This is not an optimal solution, and thus more work is needed on the conversion efficiency, or alternative beam current measurement methods should be considered (see section 7.1).

5.2 Effects on ζ-factor determination

In order to use the ζ-factor method, ζ-factors need to be determined for every element being quantified. This is a drawback compared with the conventional method of performing Cliff-Lorimer quantification with k-factors estimated by commercial EDX software. This section discusses how to find accurate ζ-factors in a practical way, and how the ζ-factors are affected by effects such as stage tilt and crystal orientation. This allows for accurate ζ-factor determination, which subsequently leads to more accurate EDX quantification. The discussion is in context of determining ζ-factors for $Ga\,K_\alpha$ and $As\,K_\alpha$ from GaAs NWs

5.2.1 Dependence on stage tilt

Figure 4.6 shows the $Ga\,K_\alpha$ ζ-factor as function of stage tilt (x-tilt). By observation, the behavior is different at low vs. high tilt angles. At low tilt angles, the ζ-factors increase as the stage tilt decreases. However, at high tilt angles, the ζ-factors are

approximately constant, independent on stage tilt. The trend is the same for all three experiments, no matter the tilt axis or whether the experiments were done in TEM or STEM mode. Also, the trend does not depend on whether $Ga\,K_\alpha$ or $As\,K_\alpha$ ζ-factors are used. The trend can be explained by detector shadowing, which is described in section 2.3.3. For low tilt angles, the path to the EDX detector is blocked by the sample stage, which causes the effective detector area to decrease. The ζ-factors are then increased to compensate for the decrease in the effective detector area. For high tilt angles, the effective detector area is constant, and hence also the ζ-factors. The trend is in agreement with Watanabe et al. [24], who tested both the effect of x-tilt and y-tilt with EDX detectors located relative to x-tilt axis and y-tilt axis. From this, and from the knowledge of the EDX detector geometry of the JEOL 2100 and JEOL 2100F (see figure 5.1), it can be concluded that β-tilt has no effect on the ζ-factors; only the α-tilt matters.
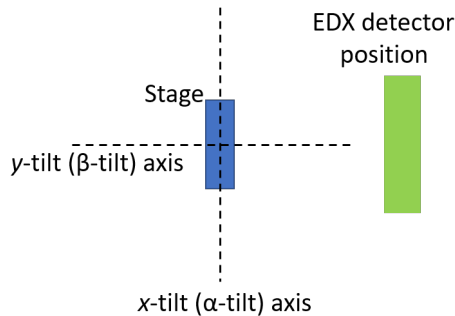
Figure 5.1: Top view of the EDX detector geometry of the JEOL 2100 and JEOL 2100F.

It is possible to fit the measured ζ-factors to a mathematical model of the shadowing effect. The fitted model can be used to estimate the angle at which shadowing starts, and to estimate ζ-factors in the shadowing region. The ζ-factors were fitted to a simple, linear model described equation 2.21 and 2.22. This was done for each of the $Ga\,K_\alpha$ and $As\,K_\alpha$ ζ-factors of experiment E1, E2 and E3. Figure 5.2 shows an example of a model-fitted curve. Table 5.2 summarizes the results.
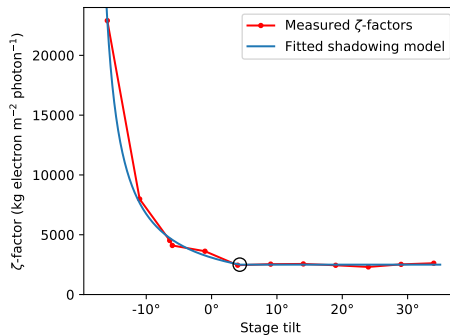
Figure 5.2: Fitting of a shadowing model to experimentally determined $\mathrm{Ga\,K_\alpha}$ ζ-factors of experiment E3. The circle denotes the stage tilt angle at which shadowing starts.

Table 5.2: Parameter values when fitting experimental $\mathrm{Ga\,K_\alpha}$ and $\mathrm{As\,K_\alpha}$ ζ-factors to a shadowing model. Θ_1 denotes the angle of complete detector shadowing, and Θ_2 denotes the angle where shadowing starts.

θ_1	θ_2
$-18.6 \pm 0.9°$	$3.9 \pm 1.2°$

The fitted models predict the onset of shadowing at approximately 4°. This is in good agreement with Nylund [25, p. 42], who reports this angle to be 4.3° on the same instrument but with a different sample. Therefore, in order to ensure there is no shadowing, the stage should be tilted to an angle larger than 4°. Furthermore, it is possible to calculate ζ-factors from shadowing regions as long as the tilt angle is known. This is done by applying equation 2.21 and 2.22 with the estimated values of θ_1 and θ_2.

Table 5.2 should not be trusted blindly. For example, the position of the sample on the TEM grid square may affect the shadowing effect, and different types of grids and grid defects all affect shadowing. The model gives only a rough estimate of the shadowing effect. If the model is used to find ζ-factors at the shadowing region, then additional error terms are introduced. Furthermore, the shadowing model which has been used is only a very simple, linear model. It is possible to use a more complex model based on the real detector geometry, such as demonstrated by Yeoh et al. [26] and Garmannslund [13].

The right-hand side of figure 4.6 shows a closer look on the $\mathrm{Ga\,K_\alpha}$ ζ-factors at the non-shadowing region. There seems to be a weak dependence on stage tilt; the ζ-factor generally decreases slightly when the stage tilt increases. However, in figure 4.10, which is for an experiment on the 2100F microscope, the trend is opposite. Ideally, there should be no stage tilt dependence on ζ-factor. The weak

trend of stage tilt dependence may be related to inaccurate thickness determination and deformation of the NW, as discussed in section 5.3.1.2. However, there is no evidence to make any conclusion on this.

As a conclusion, the ζ-factors depend on x-tilt because of shadowing effects. It is recommended to stay away from x-tilts with shadowing when determining ζ-factors. There is no dependence on y-tilt, which can be chosen freely. It is possible, but not recommended, to estimate ζ-factors in the shadowing region by compensating the shadowing effect using a fitted shadowing model.

5.2.2 Dependence on crystal orientation and crystal structure

5.2.2.1 Crystal structure

Ideally, ζ-factors should depend only on elements and not on the crystal structure. In figure 4.8(a), 4.8(b) and 4.11, ζ-factor calculated from crystal structures are plotted separately. The different crystal structures are ZB and WZ GaAs, as well as amorphous Ga.

There seems to be no consistent difference between ζ-factors measured at the WZ and ZB crystal structures. There are variations at individual points, but the variations do not correlate with the crystal structure. This means that the ζ-factor does not depend on whether the ZB or WZ region has been used as reference. This is expected from the definition of the ζ-factor (equation 2.16); in the definition, there are no terms which depend on crystal structure for the ZB crystal structure vs. the WZ crystal structure.

However, the ζ-factors calculated from the amorphous Ga catalyst droplet are consistently higher than the Ga ζ-factors from ZB and WZ. The offset is in the order of 10%. The offset is most probably caused by errors in the thickness measurements. The ZB and WZ ζ-factors have been calculated from the MBE-grown GaAs NW, and the pure Ga ζ-factor has been calculated from the NW itself. There may be errors in the thickness measurements of both the tip and the NW - this has been further discussed in section 5.3.1.

The error could have been caused by the Ga catalyst droplet not being pure. Figure 5.3 shows an EDX spectrum acquired at the Ga droplet by the JEOL 2100 in TEM mode. The $Ga\,K_\alpha$ and $As\,K_\alpha$ peaks are prominent, however, there are no signs of either As or Sb peaks. There is a small $O\,K_\alpha$ peak, however, not enough to account for 10% deviation in the $Ga\,K_\alpha$ ζ-factor. This means that the droplet is probably pure, and droplet contamination is not the cause of the offset in ζ-factor.
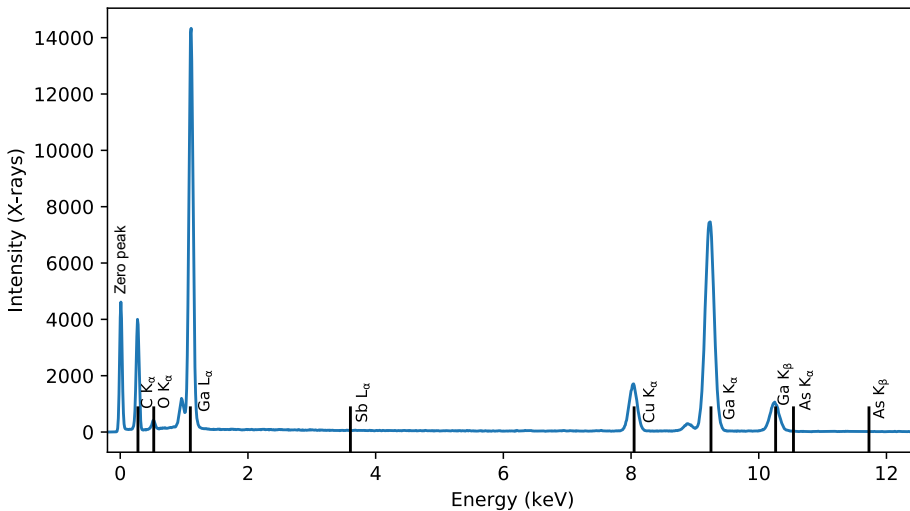
Figure 5.3: Ga spectrum acquired from a Ga catalyst droplet. The main peaks are labeled, including some As and Sb peaks, which are not present in the spectrum.

This is an example that pure-element standards may not always be the best option, although Watanabe [2] mainly considers this type of standards. It all depends on the properties of the standard, such as whether how accurately the thickness is known. In some cases, finding ζ-factors from multielemental compounds may be more convenient.

5.2.2.2 Crystal orientation

In figure 4.8(b) at the [110] zone, there are rapid changes in the ζ-factors of both $Ga\,K_\alpha$ and $As\,K_\alpha$. For example, the ζ-factors at the WZ zone change by $\sim 30\,\%$ over a tilt range of $\sim 1°$. A possible explanation for this trend is variations in channeling (see section 2.5.2.2). The DPs at the [110] zone show that the ZB segment is very close to zone while the WZ is slightly off zone; this means that channeling is likely for both segments. However, for channeling conditions, one would expect the Ga and As ζ-factors to vary in anti-phase. This is not the case for the ζ-factors being discussed, which vary in phase. Note that the Ga ζ-factor from the amorphous Ga catalyst droplet experiences a large offset as well. As this ζ-factor is from an amorphous material, it is not affected by channeling. However, this ζ-factor is very sensitive to position on the Ga catalyst droplet because of thickness measurements, and the measured ζ-factor could experience an offset because of this.

At the [112] zone in figure 4.8(b), the $Ga\,K_\alpha$ ζ-factor from the ZB segment experiences a drop, while the corresponding $As\,K_\alpha$ ζ-factor is approximately constant. The DP shows that the ZB segment is slightly off zone. Thus, the variation could

be due to channeling. On the other hand, at the WZ region (which also is slightly off zone) there are no significant variations.

At the [110] zone in figure 4.8(a), there are similar trends as the [110] zone in figure 4.8(b). There are large offsets in both the $Ga\,K_\alpha$ and $As\,K_\alpha$ ζ-factors from ZB and WZ, and the DPs show that the crystals are slightly off zone. Note that the Ga ζ-factor from the amorphous drops experiences a drop as well; however, the drop in the ζ-factor at ZB and WZ is much larger. This indicates that the deviation is due to channeling. However, the $Ga\,K_\alpha$ and $As\,K_\alpha$ ζ-factors vary in phase, which is not expected from channeling. Similar observations can be made in figure 4.11, which is for the JEOL 2100F.

The preceding discussion shows that are strong variations in ζ-factors close to zone axes, where variations in channeling are likely. However, the trends are inconsistent, and sometimes, there are no variations. Concluding these observations, the general advice is confirmed: Avoid zone axes when performing quantitative EDX. Specifically, it has been recommended to avoid the [110] zone axis in the case of GaAs, for which channeling is known to be strong [12, p. 435].

It is worth noting ζ-factors were acquired for crystal orientations between the [110] and [112] zone axes. In figure D.2, this condition is referred to as "partially on zone"; the crystal is one zone relative to one tilt axis, but not the other. Figure D.2 shows that there are large variations in the measured ζ-factors when the crystal is oriented partially on zone. This can explain some of the large deviations in ζ-factor measurements in figure 4.8 and 4.11 when the stage tilt is not at [110] or [112] zone axes. For future ζ-factor measurements, it is advised to tilt away from zone axes both in the x and y directions. Furthermore, as a strategy for reducing channeling effects, it is possible to perform EDX by precessing the electron beam. By doing this, channeling effects are canceled out. This approach has been demonstrated by Liao and Marks [27].

In this section, channeling has been regarded as a negative effect which should be avoided. However, channeling can be used constructively as well - a noteworthy example is a technique called "atom location by channeling-enhanced microanalysis" (ALCHEMI) [28]. This technique can be used to characterize the position of substitutional impurities in crystals, by looking at intensity differences due to variations in channeling when a crystal is tilted close to zone.

5.2.3   TEM vs. STEM mode

EDX can be performed both in TEM mode and STEM mode. Figure 4.9 shows $Ga\,K_\alpha$ and $As\,K_\alpha$ ζ-factors determined from single EDX spectra of GaAs NWs in both modes. The figure reveals no significant differences between ζ-factors acquired in the different modes. This is promising, as it means ζ-factor determined in TEM and STEM modes can be used interchangeably. Also, it means that beam current

measurements using the CCD can be applied reliably both in TEM mode and STEM mode.

Now, the question is which operating mode provides the most convenient and accurate way of determining ζ-factors. In TEM mode, it is quick to align the microscope and acquire some spectra. STEM mode requires more complex alignment, which is more time-consuming. However, it is easier to control the exact position of the EDX spot. Furthermore, acquiring multiple EDX spectra at the same stage tilt is trivial. The beam width in STEM mode is smaller, which means that it is easier to illuminate only the desired area. Compared with TEM mode, it is easier to perform consistent measurements.

However, there are some disadvantages to using EDX in spot mode. There is a chance that the spot is positioned in a non-representative region of the specimen. This could be a contaminated region, a region containing crystal defects or a region which is damaged otherwise. Also, when the beam is focused on the same spot for a long time, there is a chance this region is undergoing changes. As an alternative, it is possible to acquire EDX maps. When acquiring EDX maps, there is less chance of sample damage because the beam is quickly moving from one position to the next. Furthermore, as a much large area is considered as a whole, outliers are easy to spot.

As a conclusion, there are many advantages to using STEM mode for determining ζ-factors. For consistent determination of multiple ζ-factors, it is suggested to either acquire EDX spots in STEM mode or EDX maps. Williams and Carter [3, p. 584] also recommends using STEM mode for all AEM techniques.

5.2.4   Different microscopes

In this study, two different instruments have been used to determine ζ-factors: A JEOL 2100 and a JEOL 2100F. Each microscope needs its own set of ζ-factors in order to apply the ζ-factor method.

The main difference between the two instruments is the electron gun. While the JEOL 2100 has a LaB_6 thermionic emission gun, the JEOL 2100F has a FEG. The FEG electron beam has a higher degree of coherency than thermionic sources, and thus the spatial resolution is better. This is evident from figure 4.16: The GaAsSb insert has a much sharper edge to the ZB and WZ segments in the JEOL 2100F than in the JEOL 2100. Other than this, the results shown in section 4.2.4 are similar to the results for the JEOL 2100. This confirms that the effects of stage tilt and crystal orientation are general trends, which should be taken into account for the ζ-factor determination in any TEM-EDX setup.

If spatial resolution is important, such as if determining the Sb composition at the insert as shown in figure 4.16, then the JEOL 2100F is preferred. Otherwise, it is

just as well to use the JEOL 2100.

5.3 Uncertainty of the determined ζ-factors

The ζ-factors should be determined with as high accuracy and precision as possible, which means that the errors should be minimized. ζ-factors are found by equation 2.20, which is reproduced below:

$$\zeta_A = \frac{\rho t C_A D_e}{I_A} \qquad (5.1)$$

The error in a single ζ-factor measurement is given by the following expression [29, p. 77], where δx denote the error in term x,

$$\frac{\delta \zeta}{\zeta} = \sqrt{\left(\frac{\delta \rho}{\rho}\right)^2 + \left(\frac{\delta t}{t}\right)^2 + \left(\frac{\delta C_A}{C_A}\right)^2 + \left(\frac{\delta D_e}{D_e}\right)^2 + \left(\frac{\delta I_A}{I_A}\right)^2} \qquad (5.2)$$

In order to determine the error of the ζ-factor, the error of each individual term needs to be considered. Each error term is discussed in the following subsections. Following this, absorption effects are discussed. The section concludes with the determination of $Ga\,K_\alpha$ and $As\,K_\alpha$ with error terms from a series of measurements, for two different microscopes.

5.3.1 Thickness

5.3.1.1 Thickness measurements

The thickness of the NWs has been estimated from the projected NW width, by using equation 2.24. When the NW was tilted, equation 2.34 or 2.35 was used to estimate the thickness, depending on the tilt axis. Figure 5.4 illustrates the effect of thickness correction on ζ-factor measurements.
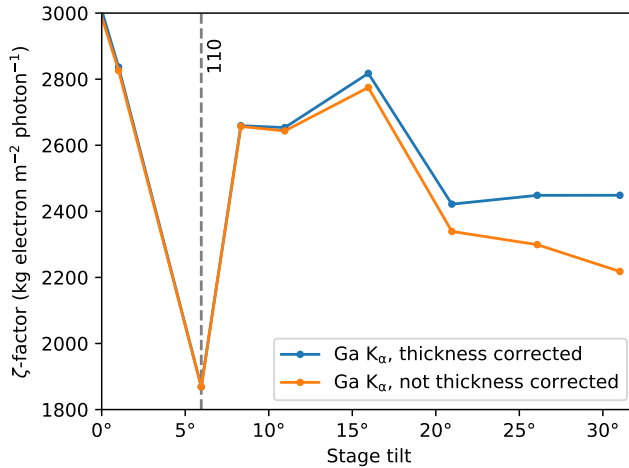
Figure 5.4: Effect of thickness correction on experiment E1.

The width of the NWs and the Ga catalyst droplets have been estimated by visual inspection of BF-TEM or HAADF-STEM images in DigitalMicrograph. Finding the width is challenging, as the border between the NW and the background is not clear-cut. This may introduce systematic errors in thickness determination. However, in order to ensure consistency between the different experiments, the widths have been found using the same procedure: through line profiles, similar to figure 5.6. However, there may be systematic errors in the width determination.

Note that the Ga catalyst droplet is particularly prone to errors in the positioning of the electron beam. This is a reason the error in thickness determination of the droplet is believed to be larger than the error in the thickness estimate of the NW.

5.3.1.2 Nanowire geometry

For the thickness estimation, the NWs are assumed to be perfectly shaped. The NWs are assumed to be perfect hexagonal prisms, and the NW tips are assumed to be perfectly spherical. However, this may not be the case, and this introduces errors to the ζ-factor measurements.

To illustrate this, figure 5.5 shows the cross section of AlGaAs/GaAs core-shell NWs. The GaAs core is very similar to the GaAs NWs which have been used in this study, and they have been synthesized using a similar procedure. In some cases, the NWs are almost perfectly hexagonal, whereas in other cases they may be heavily deformed. This may be the case for the NWs of this study as well.
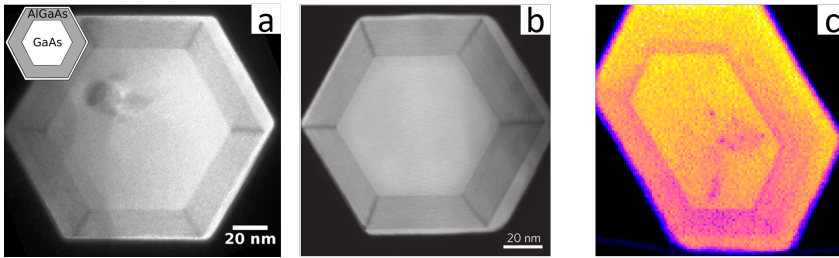
Figure 5.5: Cross section of AlGaAs NWs from (a) Kauko [30, p. 46], (b) Munshi [31, p. 38] and (c) Garmannslund [13, p. 34].

It is a challenging task to find cross sections similar to figure 5.5 of the NWs studied in this project. However, it is possible to use methods to verify the shape indirectly. This has been done in the following paragraphs.

HAADF-STEM images

HAADF-STEM images can be used as an indicative measure of thickness [30]. Because the sample has a homogeneous composition, the contrast is only due to mass-thickness. Figure 5.6 shows a STEM image and a line profile from experiment E4. In an ideal NW, the ratio of the edge part to the middle part is 0.5. In figure 5.6(b), the ratios are 0.55 and 0.57, which is an offset of about 10 %. This indicates a slight asymmetry. However, the border separating the edge from the central part is not well-defined, and any definite conclusion on the symmetry of the cannot be made from this image.

For the JEOL 2100 microscope, which has a thermionic electron gun, the spatial resolution is significantly less. Thus, ADF-STEM images on the JEOL 2100 cannot be used to make conclusions on the NW geometry.
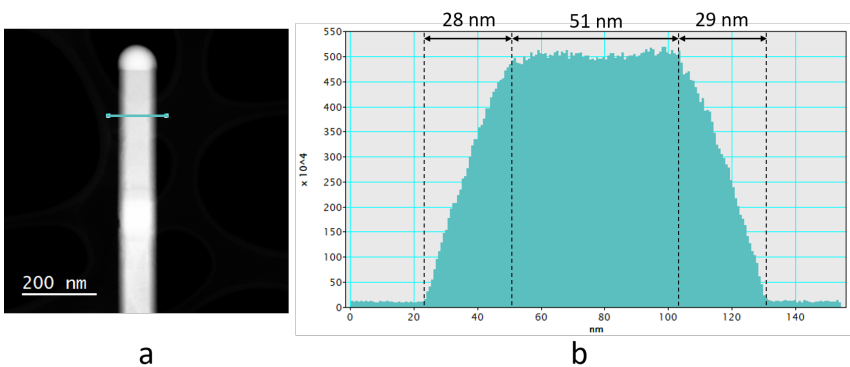
Figure 5.6: STEM image and line profile of a NW from experiment E4.

Projected NW width at different stage tilts

TEM images taken at the [110] and the [112] zone axes can be used to indicate the symmetry of the NWs. The ratio of the projected widths at these zone axes is well-defined (see figure 5.7), and given by equation 2.33. Measurements were performed on the NW used in experiment E2 and E3, and the results are shown in table 5.3. The table also includes the width of the Ga catalyst droplet, which ideally does not depend on stage tilt. Figure D.1 shows the images from which thicknesses were estimated.
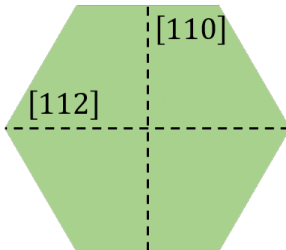
Figure 5.7

Table 5.3: Projected NW width at zones [110] and [112], taken from the NW used in experiment E2 and E3.

	NW width	Tip width
[110]	99 nm	104 nm
[112]	93 nm	109 nm
Ratio	0.94	1.05
Predicted ratio	0.87	1
Offset	-7 %	5 %

Table 5.3 indicates that both the NW and the NW tip are slightly deformed. Such deformations can cause a significant offset in the value of the ζ-factors. This is a possible explanation for the abnormal stage tilt dependence in the right-hand side of figure 4.6 and 4.10, which was measured on this exact NW.

Thickness determination is one of the major error terms in determining ζ-factors from NWs. This has also been recognized by Garmannslund [13], who did similar measurements on another TEM microscope.

5.3.2 Electron dose

The electron dose D_e is related to the beam current I_p by the following equation,

$$D_e = N_e I_p \tau \tag{5.3}$$

N_e is a constant (the number of electrons per unit charge), and the acquisition time τ is known precisely. Thus, the error in electron dose equals the error in beam current.

During the experiments, the beam current was monitored about every 10 minutes. Note that the beam current at each EDX spectrum was determined by interpolation, as described in appendix C.2.2. As discussed in section 5.1.2, the beam current variation is generally $\sim 1\,\%$/hour. This means that the estimated beam current should represent the real beam current well. Thus, there is assumed to be no error in the beam current estimate.

5.3.3 Intensity

X-ray intensities in EDX spectra are found by model fitting in HyperSpy. The exact procedure is described in appendix C.2.3; it has been necessary to make some sophisticated adjustments in order to ensure high-quality fitting. Figure C.4 in the appendix shows the result of model fitting to one single spectrum. The model is very well aligned with the measured peaks, and thus, the model fitting procedure is assumed to introduce no error to the intensity term. As a side note, when *applying* the ζ-factor method, X-ray intensities should be found using the same procedure as when the ζ-factors were determined, so as to minimize the error. Thus, it is recommended to use model fitting rather than the window method when applying the ζ-factors found in this study.

A common alternative to model fitting is the window method. For this method, a line is drawn from the left to the right side of the peak, the background is removed, and then the peak is integrated. This method is less accurate when there are overlapping peaks, as is the case for the $\text{As}\,\text{K}_\alpha$ (see figure C.4). The model fitting procedure can deconvolute overlapping peaks, which is one of the reasons model fitting is the preferred method for extracting intensities.

Even though the number of X-rays can be known exactly, there will always be fluctuations in the X-rays reaching the detector. These variations affect the precision of ζ-factor measurements. The fluctuations follow a Poisson distribution (see e.g. [9, p. 291]), and are reduced if the EDX illumination time is increased as long as it does not damage the sample. As a test of random fluctuations in EDX spot mode, the intensity ratio of $\text{Ga}\,\text{K}_\alpha$ to $\text{As}\,\text{K}_\alpha$ has been plotted for one of the experiments

76

(see figure 5.8). This ratio should be constant, no matter the stage tilt, specimen thickness or beam current.
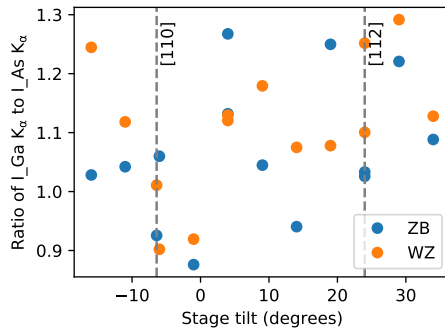
Figure 5.8: Ratio of the intensities of $\mathrm{Ga\,K_\alpha}$ to $\mathrm{As\,K_\alpha}$, as function of stage tilt. The crystal orientation varies with stage tilt, and zone axes are indicated. The data is taken from experiment E3, for which the EDX live time was $60\,\mathrm{s}$. The ZB and WZ regions have been plotted separately; both contain 50-50 % GaAs.

The figure shows that the ratio is far from constant, but varies approximately $\pm$ 20 %. Some of these variations may be due to random fluctuations, as discussed above. However, a more likely explanation for the large deviations is variations in channeling, as discussed in section 5.2.2.2. Other possible causes are a wrong position of the beam on the sample or sample contamination.

5.3.4   Density and composition

The density ρ has been determined from the HyperSpy library, or from other literary sources. It is assumed to have no error. The density does have a temperature dependence, but all samples have measured at a constant temperature.

The composition C_A of the GaAs NW which has been used for ζ-factor determination is assumed to be known exactly. GaAs has a 50-50 at% stoichiometrically ratio of Ga to As. There may be an error in composition due to contamination and sample degradation; however, this effect is considered negligible.

5.3.5   Absorption effects

As pointed out by Watanabe [2], for accurate ζ-factor determination, absorption of X-ray lines in the sample needs to be negligible. Figure 2.15 shows *self-absorption* of the elements; however, this table cannot be used directly for the multielemental

standards used in this study. Instead, absorption has been calculated using Beer-Lambert's law (see equation 2.4) for the Ga Kα and As K_α X-ray lines in 50-50 % GaAs, using linear-density absorption coefficients in HyperSpy, which are retrieved from the database by Chantler et al. [11]. Figure 5.9(a) shows the results.
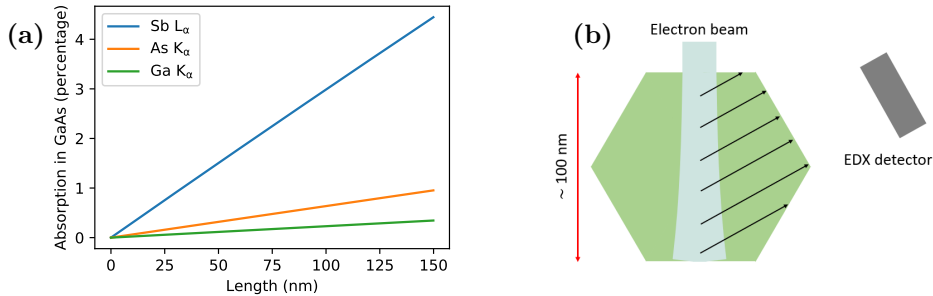
Figure 5.9: (a) Percentage absorption of X-ray lines in GaAs. (b) The black arrows indicate the path of the X-rays to the detector. The absorption length depends on where the X-rays are created.

The studied NWs have a thickness of about 100 nm. However, the absorption length (visualized in figure 5.9(b)) is less than the thickness; as an estimate, it is about 50 nm. The Sb L_α X-rays is absorbed the most: At 50 nm absorption length, the absorption is about 1.5 %. In the case of Ga K_α and As K_α, the absorption is much less than 1 % at the same absorption length. Thus, absorption is considered to be a negligible effect for the ζ-factor determination of Ga K_α and As K_α.

5.3.6   Determining ζ-factors with errors

This section shows how ζ-factors with errors have been determined through a series of measurements. Watanabe [2] devises a thorough method for doing so using the Student's t distribution, and by settings a desired confidence interval. By using t-statistics, the error is well estimated because the standard deviation of the population is unknown. However, for this project, the simpler approach of estimating the mean and standard deviation of the dataset has been used. When the number of measurements is large, the difference between the two approaches is small. For the measurements, only the intensity term is varying - all other terms are assumed to be known precisely. Still, there may be systematic errors, for example in the thickness measurements (discussed in section 5.3.1).

ζ-factors were found by collecting individually determined ζ-factors from different experiments, and removing outliers manually. For the JEOL 2100, three experiments were used as sources for ζ-factors: Experiment E1, E2 and E3. For the 2100F, experiment E4 was used. See table 3.3 for details on each experiment. As

the first step, all ζ-factors determined in the shadowing region were rejected. Then, outliers were removed manually by visual inspection. Figure 5.10 and 5.11 show the distribution of ζ-factors on the JEOL 2100, plotted for each experiment and each region separately
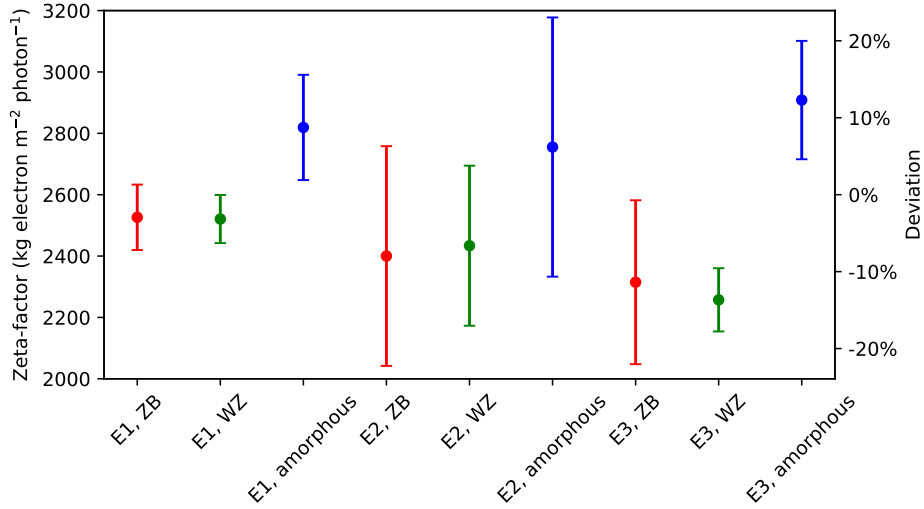
Figure 5.10: Overview of determined $Ga\,K_\alpha$ ζ-factors for the JEOL 2100. The ζ-factors are sorted on experiment and crystal structure. The index indicates the experiment (refer to table 3.3 for details on each experiment). The index can be used to deduce where ζ-factors come from; for example, refer to figure 4.8(b) for the data points used to calculate the ζ-factors for experiment E3.
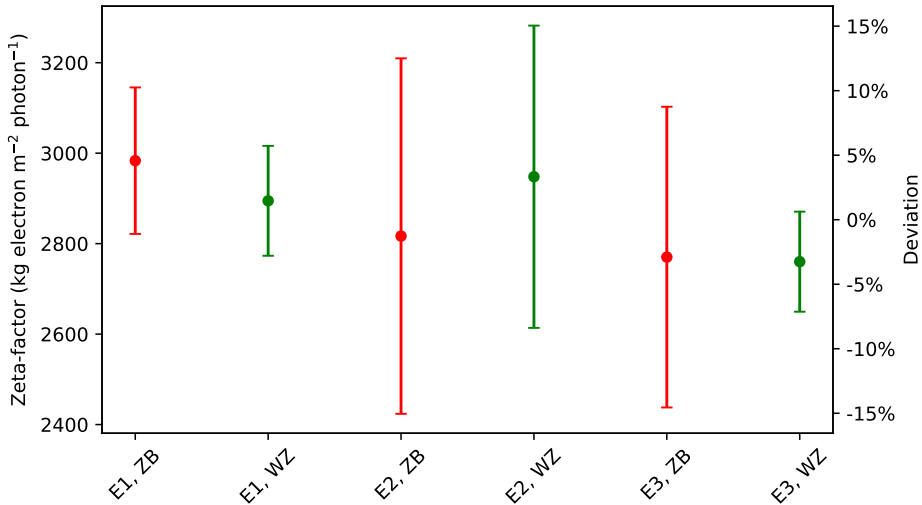
Figure 5.11: Overview of determined $As\,K_\alpha$ ζ-factors for the JEOL 2100F. The ζ-factors are sorted on experiment and crystal structure. The index indicates the experiment (refer to table 3.3 for details on each experiment).

It was observed that the Ga ζ-factors from catalyst droplets (termed "amorphous" in figure 5.10) were consistently higher than the ζ-factors from the GaAs NW. It was chosen to exclude these ζ-factors because the uncertainty in thickness determination of the droplet was believed to be larger than for the thickness determination of the NW. The mean and standard deviation of the remaining ζ-factors are tabulated in table 5.4.

Table 5.4: Determined ζ-factors for the JEOL 2100 and JEOL 2100F

ζ-factor (kg electron m^{-2} photon^{-1})	JEOL 2100	JEOL 2100F
$Ga\,K_\alpha$	$2.40 \pm 0.24 \times 10^3$	$1.63 \pm 0.16 \times 10^3$
$As\,K_\alpha$	$2.85 \pm 0.27 \times 10^3$	$1.96 \pm 0.18 \times 10^3$

The error terms in table 5.4 can be used to estimate upper and lower bounds for the compositions when quantifying using these ζ-factors. The relative errors of the Ga and As ζ-factors on the JEOL 2100 are 10.0 % and 9.5 %, respectively. Now, the error when quantifying by the ζ-factor method equals the error when quantifying by the Cliff-Lorimer method, using the k-factor $k_{AB} = \frac{\zeta_A}{\zeta_B}$. By error propagation, $\epsilon_{k,AB} = \sqrt{(10.0\%)^2 + (9.5\%)^2} = 13.8\%$. According to Williams and Carter [3, p. 657], the error when quantifying by the Cliff-Lorimer method is given by 5.4,

provided the errors in intensities I_A and I_B are negligible.

$$\left(\frac{\epsilon_C}{C_A/C_B} \right)^2 \approx \left(\frac{\epsilon_{k,AB}}{k_{AB}} \right)^2 \tag{5.4}$$

For the specific case of a specimen with 50-50% GaAS composition, the ratio between the compositions is in the range $C_A/C_B = 1 \pm 13.8\%$. This corresponds to Ga compositions in the range $50.0 \pm 3.2\%$. Note that this calculation is based on a confidence interval given by the standard deviation (68 %).

For comparison with values in the literature, Williams and Carter lists experimental k-factors from various sources. The experimentally determined k-factor for Ge (which is close to both Ga and As in the periodic table) had an error of 28 %. For other elements, such as for Ni, some sources report errors of less than 1 %.

An alternative approach for determining ζ-factor was tested for the JEOL 2100 experiments: ζ-factors were found by fitting the measured values to a shadowing model, using the same approach as described in section 5.2.1. The ζ-factor can be trivially extracted from the fitted model, as the ζ-factor is one of the parameters used for fitting. The fitting was done for the ZB and WZ regions individually. Table 5.5 shows the results.

Table 5.5: ζ-factors determined for the JEOL 2100, by fitting to a shadowing model.

ζ-factor (kg electron m^{-2} photon^{-1})	JEOL 2100
Ga K$_\alpha$	$2.33 \pm 0.09 \times 10^3$
As K$_\alpha$	$2.77 \pm 0.09 \times 10^3$

Using this approach, the standard deviation is much smaller. This is probably because an average value was used for each experiment. However, as table 5.5 is based on a more robust statistical procedure, this error is probably a better estimate of the real ζ-factor error.

Note that all ζ-factor in this section are all given in terms of weight percentages rather than atomic percentages. Consequently, the output of the quantification routine has units of weight percentages. These can subsequently be converted to atomic percentages - this has been done in this project.

To conclude the sections on ζ-factor determination, a set of suggested guidelines for measuring ζ-factors from NW standards has been made. The guidelines are based on the preceding discussion and experiences made as part of this project. The guidelines are listed below.

- Use STEM mode and acquire EDX spectra in spot mode. If the microscope allows it, it is recommended to perform EDX with precession.

- Use a large spot size, so as to acquire data from a large area and reduce the risk of sample damage.

- Use $\sim 1\,\text{min}$ EDX exposure time.

- Work at stage tilt angles well above the critical angle at which shadowing starts.

- Find a zone axis for which the sample surface is orthogonal to the electron beam. For the ZB crystal structure, this is the [110] zone axis. This allows for estimating the thickness based on the projected NW width.

- Tilt some degrees off the zone axis (e.g., 5°) both in the x and y direction before acquiring EDX spectra, to reduce the risk of channeling.

- Acquire EDX spectra at different stage tilts. For example, use tilt intervals of ~ 3°. Make sure to record each stage tilt, to enable subsequent thickness estimates.

- Acquire many EDX spectra (e.g., 10) for each tilt.

5.4 Applying the ζ-factor method

This study has aimed at improving the accuracy of quantitative EDX, by introducing the ζ-factor method. This has been done by considering the beam current, analyzing factors which affect ζ-factors and estimating ζ-factors through a series of measurement. In this section, the estimated ζ-factors (referred to as *tabulated ζ-factor*) have been verified by applying the ζ-factor method to different samples.

Section 5.4.1 compares tabulated ζ-factors with the Cliff-Lorimer method. Following this, section 5.4.2 and section 5.4.3 demonstrate two alternative approaches to tabulated ζ-factors, which may perform better than tabulated ζ-factors in certain cases. The approaches are termed *internal ζ-factors* and *tuned ζ-factors*, respectively.

5.4.1 Tabulated ζ-factors

To assess the performance of the tabulated ζ-factor in table 5.4, they were applied in the quantification of GaAs particles from a different dataset. The experiment was performed on the JEOL 2100F. As shown in figure 4.12 both the Cliff-Lorimer method and the ζ-factor method give Ga compositions which are close to real composition of 50 at%. Both figure 4.12(a) and (b) show that the ζ-factor slightly

underestimates the composition while the Cliff-Lorimer method gives a small over-estimate; however, both methods have an offset of about 1% relative.

Furthermore, the tabulated ζ-factors for both the JEOL 2100 and JEOL 2100F were applied to the WZ region of GaAs NWs (see figure 4.14). The offset of the Cliff-Lorimer method is $\sim 3\%$ relative, while the offset of the ζ-factor method is $\sim 1\%$ relative. This is true both for the JEOL 2100 and the JEOL 2100F.

To sum up, the ζ-factor method gives quantification results within 1 % relative both for the JEOL 2100 and the JEOL 2100F, and for multiple experiments on the 2100F. The ζ-factor determinations on the JEOL 2100 and JEOL 2100F have been done independently, and the positive results verify that the ζ-factor determination procedure works in general. For the $\mathrm{Ga\,K_\alpha}$ and $\mathrm{As\,K_\alpha}$ ζ-factors, the ζ-factor method is competitive with the Cliff-Lorimer method.

5.4.2 Internal ζ-factors

In this section, the concept of internal ζ-factors is defined and explained. Then, the internal ζ-factors are compared with tabulated ζ-factors and Cliff-Lorimer method in the quantification of GaAs NWs.

Internal ζ-factors are defined in this report as ζ-factors which are determined on the same EDX map as the region which is quantified. The simple concept is visualized in figure 5.12. The ζ-factors are determined from region A, which has known composition, and then applied to region B in order to find the composition there.

An advantage of internal ζ-factors is that fact that the beam current and the thickness are not needed for determining ζ-factors. This is because the beam current and the sample thickness is the same no matter which element is considered. Thus, they are canceled out when performing quantification using equation 2.17. Furthermore, internal ζ-factors are not affected by shadowing of the EDX detector. This is because shadowing effectively reduces the beam current, and as previously stated, the beam current is canceled out when applying internal references. Some other variations, such as variations in detector efficiency, cancel out as well. It should be noted that internal ζ-factors cannot be used to calculate thickness maps; they can only be used to calculate compositions. Also, the advantages do not hold if internal ζ-factors of some elements are combined with tabulated ζ-factors of other elements.

Internal references do not require the beam current and sample thickness to be known. However, if they *are* known, then the internal ζ-factors can be converted into tabulated ζ-factors. Then, they can be used in combination with any other tabulated ζ-factor and used, for instance, for thickness determination.

Internal ζ-factors have an obvious limitation: There must exist a region on the

EDX map for which the composition is known exactly. If this criterion is met, then internal ζ-factors are expected to perform better than both tabulated ζ-factors and the Cliff-Lorimer method because of the advantages stated above.
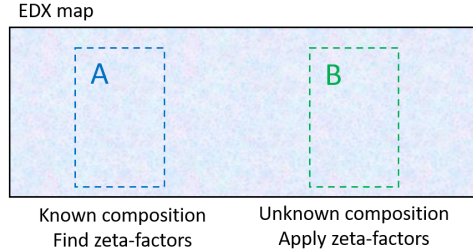

Figure 5.12: Sketch showing the principles of internal ζ-factors.

Internal ζ-factors have been used to quantify GaAs NWs (see figure 4.14). The ZB region was used as a reference for determining $\mathrm{Ga\,K_\alpha}$ and $\mathrm{As\,K_\alpha}$ ζ-factors, which were subsequently used to quantify the WZ region. The composition of both Ga and As using internal ζ-factors is within $1\,\%$ relative of the real value. Figure 4.14 shows that both internal ζ-factors and tabulated ζ-factors give better quantification results than the Cliff-Lorimer method. Internal ζ-factors give similar quantification results as tabulated ζ-factor; on the JEOL 2100F, the internal ζ-factors perform slightly better. Thus, internal ζ-factors have been confirmed to give quantification results which are generally better than both tabulated ζ-factor and the Cliff-Lorimer method. Based on this example, as well as the advantages stated above, it is recommended always to use internal ζ-factors if possible.

As part of this project, Python code has been developed for calculating and applying internal ζ-factors in a convenient way. This code is described in in appendix C.1.4. By using this code, it should be convenient to use internal ζ-factors on similar datasets.

5.4.3 Tuned ζ-factors

In this section, the concept of tuned ζ-factors is defined and explained. Then, the performance of tuned ζ-factors is discussed when applied to some datasets, to see how it compares with the Cliff-Lorimer method.

A tuned ζ-factor, as defined in this report, is a ζ-factor which is found by adjusting its value so as to maintain some constraint. For this project, the constraint is that the Ga composition should be exactly 50 at% at all positions, including at the GaAsSb insert. This constraint is physical, because Sb atoms only replace As atoms. In principle, there are many other constraints which can be used to tune ζ-factors. Figure 5.13 shows how the Ga composition changes as the Sb ζ-factor is

changed. This is what makes tuning of Sb ζ-factors possible.

Note that only one element can be tuned at the same time - the ζ-factor of all other elements must be known. However, the ζ-factors of the other elements do not have to tabulated - they can be determined internally (see section 5.4.2).
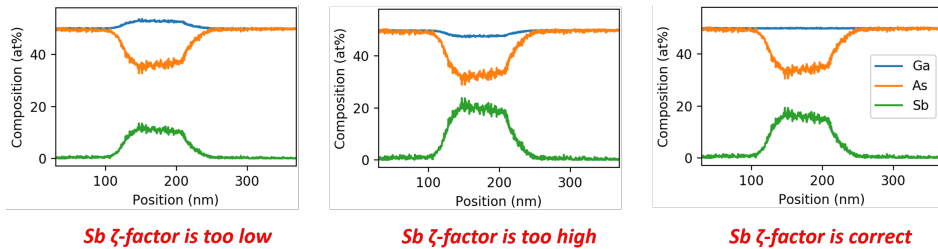

Figure 5.13: Sketch illustrating the principle of tuned ζ-factors. The Sb ζ-factor is tuned so as to make the Ga composition exactly 50 % at all positions. In this figure, the Ga K_α and As K_α ζ-factors have been determined internally.

GaAs NWs with a GaAsSb insert can easily be quantified by the Cliff-Lorimer method, as all k-factors are readily available. The compositional profiles from the Cliff-Lorimer method are shown in figure 4.15. The Ga and As compositions are off by a few percentages relative, and the Ga composition changes at the GaAsSb insert, which is unphysical.

The ζ-factor method cannot be used directly, because tabulated ζ-factors are currently only available for Ga K_α and As K_α (see table 5.4). Also, the Sb composition is now known anywhere on the EDX map, which means that the Sb L_α ζ-factor cannot be determined internally. However, the ζ-factor method can be used if the Sb-factor is found by tuning, using the constraint that the Ga composition should be exactly 50 at%. This has been done in figure 4.15, which shows the resulting compositional profiles. Qualitatively, the compositional profiles from the internal and tuned ζ-factors seem to reflect the real composition significantly better than the Cliff-Lorimer method. However, the Sb composition at the insert is not known, and thus the Sb L_α ζ-factor cannot be assessed directly.

In order to assess how well the set of internal and tuned ζ-factors are calibrated, they were converted to tabulated ζ-factors and used to quantify a dataset of GaSb particles. This conversion to tabulated ζ-factors is possible because the beam current and sample thickness are known. A range of different particles with different shape and thickness were tested, and figure 4.17 shows the results. For the JEOL 2100 (figure 4.17), the ζ-factor method gives Ga compositions which vary about the real value of 50 at%, for all spectra up to the spectrum with ID J4. On the other hand, the Cliff-Lorimer method consistently overestimates the Ga composition by about 10-15 % relative.

There is a strange trend in the plot: Spectra with ID J5 and higher all have an offset compared with the previous spectra. Both the ζ-factor compositions and the Cliff-Lorimer compositions have an offset of about the same amount. A possible explanation for the offsets is sample damage caused by the beam. Alternatively, it could be a consequence of the position of the particles in the grid; if they were close to the Cu support, then Ga and As could be unevenly absorbed by the Cu.

Figure 4.17(b) shows a similar experiment on the JEOL 2100F. For some of the points, the ζ-factor method gives compositions very close to the real value, while the Cliff-Lorimer gives an overestimation. However, at other points, both methods have a significant offset. Note that melting and dephasing of particles was observed during this experiment, which may explain some of the deviation. In any case, from this figure alone, nothing can be concluded about which method is better. Figure 4.17(c) shows a composition histogram from an EDX map which was acquired on the JEOL 2100F. The histogram shows that the ζ-factor method gives the best estimate of the composition, while Cliff-Lorimer method overestimates.

A general trend can be concluded from the experiments in figure 4.17: The ζ-factor method with internal and tuned ζ-factors generally gives better results than the Cliff-Lorimer method. However, there are some measurements which have a significant offset, both for the ζ-factor method and the Cliff-Lorimer method.

In order to test the generality of the method of ζ-factor tuning, as well as the Python code used for analysis, the approach was tested on a different dataset acquired on JEOL ARM-200F. This TEM has not been used previously in this project. Again, the ζ-factor method gives qualitatively better compositional profiles than the Cliff-Lorimer method. However, as the Sb composition is unknown, the general validity of the tuned Sb ζ-factor cannot be concluded from this experiment alone. However, this example verifies that the principle of ζ-factor tuning is applicable for other datasets.

As a final note, tuned ζ-factors are defined under the thin-film approximation (just as for ζ-factor determined experimentally and k-factors). This means that there should be no absorption in the sample, and if there is, then the ζ-factor will be shifted. However, it is possible to perform ζ-factor quantification with absorption correction. In principle, if tuning the Sb ζ-factor to the Ga composition, and finding the compositions with absorption correction, then it is possible to find an absorption-free Sb ζ-factor. The same approach could be used to find absorption-free ζ-factors for other elements as well. Finding absorption-free ζ-factors is often a challenging task, but with ζ-factor tuning, this problem could possibly be solved for some new cases.

Chapter 6

Conclusion

In this work, methods for calibrating and using the ζ-factor method on a JEOL JEM-2100 and a JEOL JEM-2100F have been developed, with the aim of improving quantitative TEM-EDX accuracy.

A DigitalMicrograph script for performing indirect measurements of beam current consistently and conveniently through the CCD was developed, and then applied to all subsequent TEM-EDX experiments. Furthermore, Python code for analyzing the beam current as well as integrating the beam current in ζ-factor determination has been developed. The beam current was verified to be stable enough for accurate ζ-factor determination; however, frequent monitoring of the beam current is recommended. A varying CCD conversion efficiency has been identified; however, this does not limit the accuracy of the results in this report.

ζ-factors for $\mathrm{Ga\,K_\alpha}$ and $\mathrm{As\,K_\alpha}$ were determined through different experimental setups, with errors of approximately $10\,\%$ due to statistical variations. Thickness determination of the standard specimen used for calibration was identified as a major contributor to errors. Furthermore, the effects of stage tilt, crystal orientation and TEM operating mode on the ζ-factors were analyzed. The ζ-factors were found to increase consistently with tilt angle below a critical angle, due to shadowing effects. The angle at which shadowing starts was estimated by fitting the measured ζ-factors to a model. It is recommended to use stage tilts well above this angle when determining ζ-factors. No significant difference in ζ-factors determined from ZB and WZ crystal structures was identified. However, near low-indexed zone axes, the ζ-factors can change rapidly due to channeling. Thus, it is recommended to work off zone when determining ζ-factors. Lastly, no significant difference between TEM mode and STEM mode was observed. This means that ζ-factors found by different modes can be used interchangeably. There are a number of reasons STEM mode should be used rather than TEM mode. To sum up these findings graphically, figure 6.1 shows the observed trends in the ζ-factors schematically.
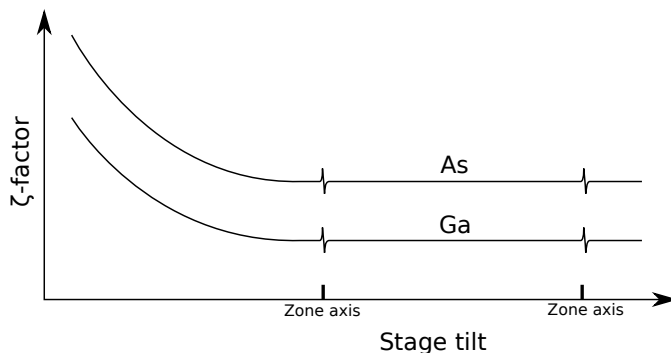
Figure 6.1: The effect of stage tilt and zone axes on ζ-factors, shown schematically.

The determined ζ-factors of $Ga\,K_\alpha$ and $As\,K_\alpha$ were verified by applying the ζ-factor method to various samples with known composition. The ζ-factor method was found to give similar or better quantification results than the Cliff-Lorimer method in all studied cases, which is a verification that the developed method for determining ζ-factors is viable.

Furthermore, alternative approaches to conventional ζ-factors were demonstrated. The first approach is internal ζ-factors, which were found to give better quantification results than the Cliff-Lorimer method and similar results to tabulated ζ-factors in all studied cases. The internal ζ-factor approach can only be used for a limited set of samples; however, it is recommended to use this approach whenever possible because of its advantages. The second approach - tuned ζ-factors - can be applied in some cases were tabulated ζ-factors are not available and internal ζ-factors cannot be found. The combination of internal and tuned ζ-factors was found to give better results than the Cliff-Lorimer method for GaSb NWs, and the approach seems to be valid in general.

The developed methods demonstrate improvements in TEM-EDX quantification accuracy compared with the commonly used Cliff-Lorimer method. Still, tabulated ζ-factors need to be calculated for many more elements before the ζ-factor method can be used as conveniently as the Cliff-Lorimer method. Furthermore, there is still room for improvements in beam current measurements. If more work is done, then the ζ-factor method can ultimately be used just as conveniently as the Cliff-Lorimer, yet with much better accuracy.

Chapter 7

Future work

7.1 Beam current measurements

Currently, beam current measurements are done using the CCD attached to the TEM. Issues have been identified with the CCD conversion efficiency: there seems to be an unphysical dependence on spot size and condenser aperture. For CCD measurements to be accurate, this issue should be resolved.

Another option is to measure the beam current by other means. There are various ways to detect electrons in a TEM; however, the detector needs to be highly accurate. Any inaccuracy will directly cause errors in the determination of ζ-factors. The fluorescent screen inside the TEM chamber has been used as an electron detector by Zanaga et al. [32] and Barabino [33]. However, this is not an optimal solution because the fluorescent screen suffers from effects such as charging, inhomogeneity and nonlinearity [33]. A better option could be to use the HAADF-STEM or BF-STEM detector for beam current measurements. This is possible because the detector image is directly proportional to the beam current [34]. In order to use a STEM detector as an accurate beam current detector, the detector response should be characterized and calibrated for beam current measurements in the same way as for the CCD (see section 4.1.1).

If EDX maps are acquired, then it may be possible to measure the beam current in situ. For this to be possible, the EDX map should be extended to a region with vacuum. If the beam current in the vacuum region is recorded by some detector, such as a BF-STEM detector, then it is possible to measure the beam current in situ.

Figure 4.4 shows a measurement of the beam current on the JEOL 2100 for a period of 40 min. It is possible to repeat this experiment and measure the beam

current for a longer period of time, in order to investigate whether the 10 % drop was representative for the beam current or just a one-time event.

7.2   Determining additional ζ-factors

For the ζ-factor method to be used in a practical way, tabulated ζ-factors are needed for every element. Currently, only the $Ga\,K_\alpha$ and $As\,K_\alpha$ ζ-factors have been determined for the JEOL 2100 and JEOL 2100F. As future work, it is suggested to find ζ-factors for additional elements from standards. As identified in this study, the thickness determination of the standard is a major contributor to errors. One way to improve on this is to acquire standards with precisely known thickness. Another option is to investigate alternative methods for accurate thickness determination.

ζ-factor determination can be done using suggested guidelines and methods as devised in this report. ζ-factors should be determined in a consistent way, and from a high number of measurements so as to reduce statistical variations. Error terms should be stated, and optimally, t-statistics should be used to determine the error. As discussed in section 2.5.2.3, it is not necessary to find ζ-factors for every element. If the ζ-factors of some elements are known accurately, then the remaining elements can be found by interpolation, as devised by Watanabe [2]. However, the more ζ-factors which are determined experimentally, the more accurate the interpolated ζ-factors will be.

7.3   Absorption correction

One of the main advantages of the ζ-factor method is the fact that absorption correction can be applied without knowing the sample thickness beforehand. The theory is well documented [2]; however, the HyperSpy library currently has no option for computing absorption correction in the ζ-factor method. Implementing absorption correction in the HyperSpy library would be a great step forward in improving quantitative EDX accuracy. Furthermore, the value of absorption coefficients from different sources can be studied. The critical self-absorption thicknesses shown by Watanabe [2] differ significantly from the corresponding values calculated using the HyperSpy library (see figure 2.15 and section E).

References

[1] G. Cliff and G. W. Lorimer. "The quantitative analysis of thin specimens." In: *Journal of Microscopy* 103.2 (Mar. 1975), pp. 203–207. ISSN: 00222720. DOI: `10.1111/j.1365-2818.1975.tb03895.x`.

[2] M. Watanabe and D. B. Williams. "The quantitative analysis of thin specimens: a review of progress from the Cliff-Lorimer to the new zeta-factor methods." In: *Journal of Microscopy* 221.2 (Feb. 2006), pp. 89–109. DOI: `10.1111/j.1365-2818.2006.01549.x`.

[3] D. B. Williams and C. B. Carter. *Transmission Electron Microscopy*. Boston, MA: Springer US, 2009. ISBN: 978-0-387-76500-6. DOI: `10.1007/978-0-387-76501-3`.

[4] N. W. M. Ritchie and J. Villarubia. *EPQ library for Electron Probe X-ray Microanalysis*. URL: `https://www.cstl.nist.gov/div837/837.02/epq/dtsa2/JavaDoc/index.html` (visited on 04/05/2019).

[5] F. de la Peña et al. *HyperSpy v1.4.1*. Oct. 2018. DOI: `10.5281/zenodo.1469364`. URL: `https://doi.org/10.5281/zenodo.1469364`.

[6] J. H. Scofield. "Exchange Corrections of K X-ray Emission Rates." In: *Physical Review A* 9.3 (Mar. 1974), pp. 1041–1049. ISSN: 0556-2791. DOI: `10.1103/PhysRevA.9.1041`.

[7] J. H. Scofield. "Relativistic Hartree-Slater Values for K and L X-ray Emission Rates." In: *Atomic Data and Nuclear Data Tables* 14.2 (Aug. 1974), pp. 121–137. DOI: `10.1016/S0092-640X(74)80019-7`.

[8] S. Salem, S. Panossian, and R. Krause. "Experimental K and L Relative X-ray Emission Rates." In: *Atomic Data and Nuclear Data Tables* 14.2 (Aug. 1974), pp. 91–109. ISSN: 0092-640X. DOI: `10.1016/S0092-640X(74)80017-3`.

[9] J. I. Goldstein et al. *Scanning Electron Microscopy and X-Ray Microanalysis*. Springer, 2017. ISBN: 149396674X.

[10] M. Watanabe and D. B. Williams. "Improvements to Energy Resolution of an X-ray Energy Dispersive Spectrum by Deconvolution Using the Zero Strobe Peak." In: *Microscopy and Microanalysis* 9.S02 (2003), pp. 124–125. ISSN: 1431-9276. DOI: `10.1017/s1431927603441111`.

[11]   C. Chantler et al. *X-Ray Form Factor, Attenuation, and Scattering Tables*. 2005. DOI: 10.18434/T4HS32. URL: https://www.nist.gov/pml/x-ray-form-factor-attenuation-and-scattering-tables (visited on 02/14/2019).

[12]   M. De Graef. *Introduction to Conventional Transmission Electron Microscopy*. Cambridge: Cambridge University Press, 2003. ISBN: 9780511615092. DOI: 10.1017/CBO9780511615092.

[13]   A. Garmannslund. *Refinement of the ζ-factor Method for Quantitative Energy-Dispersive X-ray Spectroscopy in Scanning Transmission Electron Microscopy (MSc thesis)*. Norwegian University of Science and Technology, 2016, p. 103.

[14]   C. Kittel. *Introduction To Solid State Physics*. 8th ed. Wiley, 2005, p. 680. ISBN: 978-0471415268.

[15]   A. Jain et al. "The Materials Project: A materials genome approach to accelerating materials innovation." In: *APL Materials* 1.1 (2013), p. 11002. DOI: 10.1063/1.4812323.

[16]   K. Momma and F. Izumi. "VESTA: A Three-Dimensional Visualization System for Electronic and Structural Analysis." In: *Journal of Applied Crystallography* 41.3 (June 2008), pp. 653–658. DOI: 10.1107/S0021889808012016.

[17]   P. Stadelmann. *Simulation of diffraction patterns and high resolution images using jems*. 2008.

[18]   A. M. Munshi et al. "Crystal phase engineering in self-catalyzed GaAs and GaAs/GaAsSb nanowires grown on Si(111)." In: *Journal of Crystal Growth* 372 (June 2013), pp. 163–169. ISSN: 0022-0248. DOI: 10.1016/J.JCRYSGRO.2013.03.004.

[19]   H. Kauko et al. "Near-surface depletion of antimony during the growth of GaAsSb and GaAs/GaAsSb nanowires." In: *Journal of Applied Physics* 116.14 (Oct. 2014), p. 144303. ISSN: 0021-8979. DOI: 10.1063/1.4896904.

[20]   V. S. Teodorescu and M.-G. Blanchin. "Fast and Simple Specimen Preparation for TEM Studies of Oxide Films Deposited on Silicon Wafers." In: *Microscopy and Microanalysis* 15.1 (Feb. 2009), pp. 15–19. DOI: 10.1017/S1431927609090011.

[21]   R. S. Wagner and W. C. Ellis. "Vapor-liquid-solid mechanism of single crystal growth." In: *Applied Physics Letters* 4.5 (Mar. 1964), pp. 89–90. ISSN: 0003-6951. DOI: 10.1063/1.1753975.

[22]   Python Software Foundation. *Python (programming language)*. URL: https://docs.python.org/3.7/.

[23]   G. Inc. *Orius SC200D Camera - Datasheet*. 2015.

[24]   M. Watanabe et al. "Practical Measurement of X-ray Detection Performance of Large-Angle Silicon Drift Detectors Toward Quantitative Analysis in the Newly Developed 300 kV Aberration-Corrected Grand ARM." In: *Microsc. Microanal* 21 (2015), p. 2015. DOI: 10.1017/S143192761500690X.

[25]   I.-E. Nylund. *Evaluation of energy-dispersive spectroscopy characteristics for improved compositional analysis (MSc project work)*. NTNU, 2017.

[26] C. S. Yeoh et al. "The Dark Side of EDX Tomography: Modeling Detector Shadowing to Aid 3D Elemental Signal Analysis." In: *Microscopy and Microanalysis* 21.03 (June 2015), pp. 759–764. DOI: 10.1017/S1431927615000227.

[27] Y. Liao and L. D. Marks. "Reduction of electron channeling in EDS using precession." In: *Ultramicroscopy* 126 (Mar. 2013), pp. 19–22. ISSN: 03043991. DOI: 10.1016/j.ultramic.2012.11.007.

[28] I. Jones. "Diffraction & X-Ray Excitation." In: *Transmission Electron Microscopy: Diffraction, Imaging, and Spectrometry*. Ed. by C. B. Carter and D. B. Williams. Cham: Springer International Publishing, 2016, pp. 425–437. ISBN: 978-3-319-26651-0. DOI: 10.1007/978-3-319-26651-0_15.

[29] J. R. Taylor. *An Introduction to Error Analysis*. 2nd ed. University Science Books, 1997, p. 331. ISBN: 9780935702750.

[30] H. Kauko. "Quantitative scanning transmission electron microscopy studies on heterostructured GaAs nanowires." PhD thesis. Norwegian University of Science and Technology, 2013, p. 128.

[31] A. M. Munshi. "Epitaxial Growth of Self-Catalyzed GaAs Nanowires by Molecular Beam Epitaxy." PhD thesis. Norwegian University of Science and Technology, 2014.

[32] D. Zanaga et al. "An alternative approach for ζ-factor measurement using pure element nanoparticles." In: *Ultramicroscopy* 164 (May 2016), pp. 11–16. ISSN: 0304-3991. DOI: 10.1016/J.ULTRAMIC.2016.03.002.

[33] E. Barabino, T. Withaar, and B. Freitag. "Systematic Error Determination of ζ-Factor Quantification in XEDS Analysis." In: *Microsc. Microanal* 24.1 (2018). DOI: 10.1017/S143192761800435X.

[34] X. Sang and J. M. LeBeau. "Characterizing the response of a scintillator-based detector to single electrons." In: *Ultramicroscopy* 161 (Feb. 2016), pp. 3–9. ISSN: 0304-3991. DOI: 10.1016/J.ULTRAMIC.2015.11.008.

[35] Gatan Inc. *User's guide: DigitalMicrograph Scripting*. Pleasanton, 2016.

[36] D. Mitchell. *Tutorial: Script Commands to Interact with Microscopes and Cameras*. URL: http://www.dmscripting.com/tutorial%7B%5C_%7Dmicroscope%7B%5C_%7Dcommands.html (visited on 06/09/2019).

[37] HyperSpy. *HyperSpy User Guide — HyperSpy 1.4.1 documentation*. URL: http://hyperspy.org/hyperspy-doc/current/user%7B%5C_%7Dguide/index.html (visited on 12/11/2018).

Appendices

Appendix A

Acquiring and exporting EDX data

A.1 Acquiring data for ζ-factor measurements

When acquiring EDX spectra in spot mode for ζ-factor determination, there are a few things worth taking note of. It is recommended to acquire EDX spectra at multiple tilts, and acquire several spots for each tilt. Now, in between each tilt, the following should be done:

- Measure the beam current. This could be done by the CCD camera, using the beam current script which is described in section B.

- Store the stage tilts. This is necessary for thickness corrections.

It is important to be consistent and structured when doing the measurement and when handling the data. Before exporting the spectra, it is advisable to label each spectrum. For this project, the following simple scheme was used: Each spectrum is labeled by a letter and a number (e.g. "B3"). The number denotes the tilt index (e.g. "3" means the third tilt), and the letter denotes the position on the sample. For advice on how to perform ζ-factor measurements based on experiences from this project, refer to the last part of section 5.3.6.

A.2 Guide for exporting EDX data from AZtec

Data analysis in this project has been done in HyperSpy. Before that data can be analyzed, it needs to be exported from the EDX software into a format which can be read by HyperSpy. For the JEOL 2100 and JEOL 2100F, it is AZtec software which is used. Exporting data from AZtec is not trivial, and a guide has been made in order to ease this process. The guide applies both to EDX spots and EDX maps.

Exporting EDX data from AZtec

Contents

Before you start

This guide is meant for exporting EDX data from AZtec to formats which can be easily interpreted by alternative EDX analysis software.

The AZtec project structure should look like this (the folders "data" and "reports" may not exist).

Name	Date modified	Type	Size
data	06.05.2019 13:50	File folder	
reports	06.05.2019 11:16	File folder	
EDS_2019-06-05.oip	06.05.2019 13:50	AZtec Project	1 684 KB

Open "AZtec", and open the ".oip" project file.

Exporting EDX spectra

An EDX spectrum in AZtec can be exported as an ".emsa" file. The ".emsa" format is a general text-based format which can be read by any EDX analysis software, including the open source software HyperSpy and NIST DTSA-II.

Create a folder "spectra" in the project folder.

Choose "Analyzer" mode and "Acquire Spectra" step.

In the Data Tree panel, click on the EDX spectrum to be exported (by default, they're labeled "Spectrum x"). It is recommended to rename the spectrum item (e.g. to labels "A1", "A2", "B1", etc.).
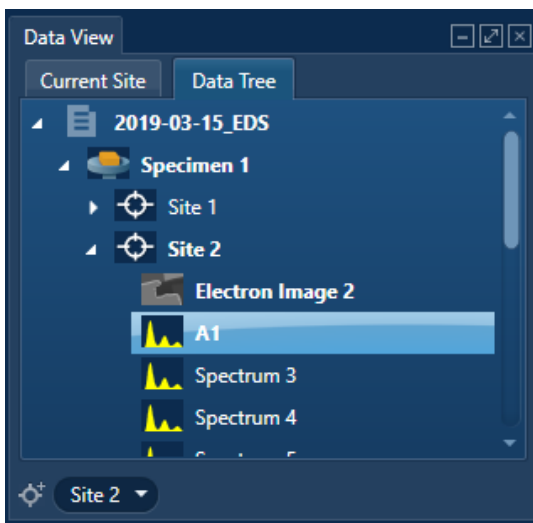
The main window should now contain the EDX spectrum. Right click the spectrum, then Export → EMSA.
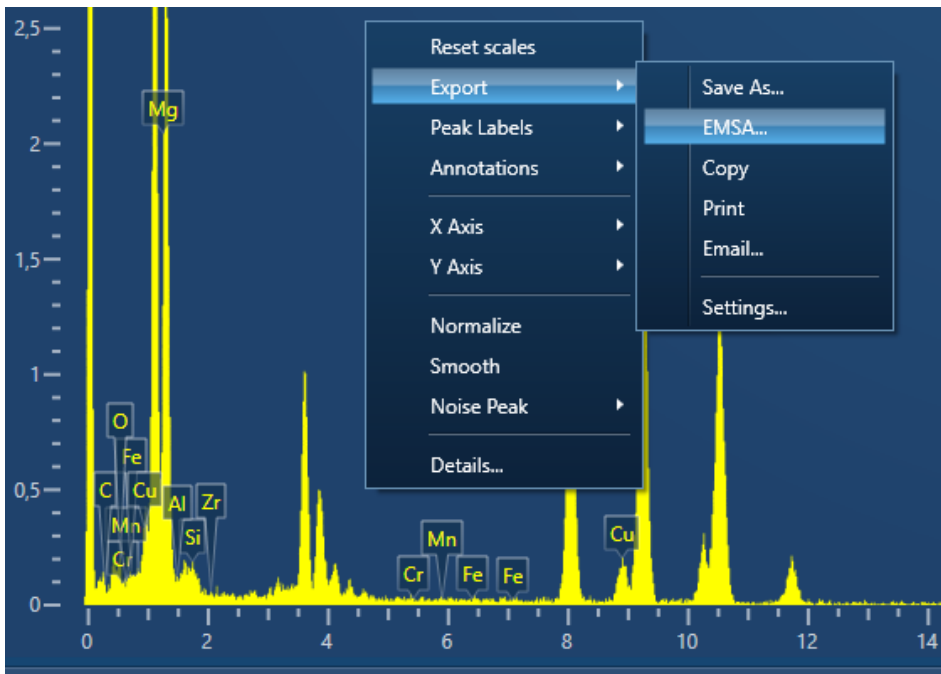
(1) Choose the "spectra" folder. (2) Choose the "*.emsa" option, (3) rename to your label and (4) press "Save".

Repeat this procedure for all EDX spectra to be exported.

Exporting EDX maps

An EDX map in AZtec can be exported as an ".hdf5" file. The ".hdf5" format is an open format which can be read by EDX analysis software such as the open source software HyperSpy. To create an ".hdf5" file, it is necessary to export the map as an ".raw" file along with a ".rpl" file describing its structure, and add calibrations from the ".emsa" sum spectrum and additional metadata from a ".txt" file. The procedure below describes how to do this.

Create a folder "maps".
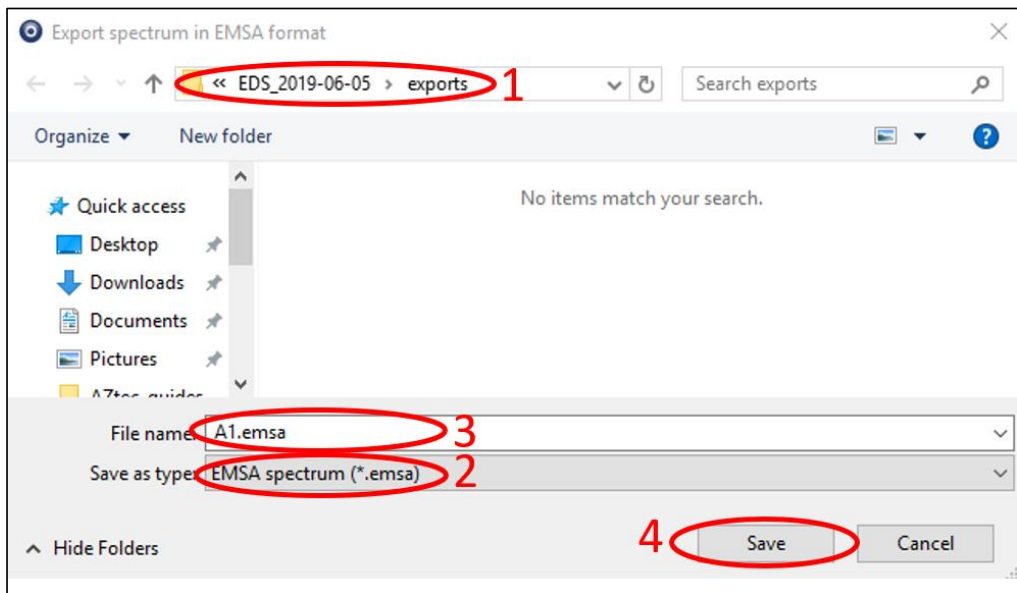
In the Data Tree panel, locate the EDX map to be exported (by default, they're labeled "Map Data x"). It is recommended to rename the EDX map item (I use labels "A1", "A2", "B1", etc.).

Right click → Batch export
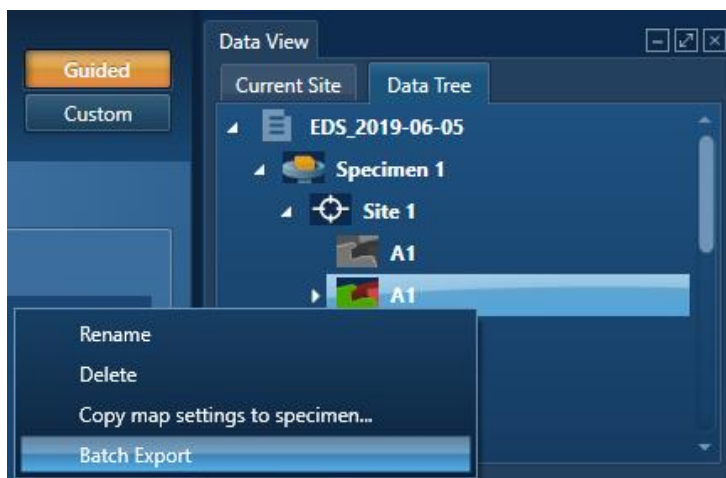
In the Batch Export menu, choose options (1, (2) and (3).
(4) Rename to your label and (5) choose the "maps" folder. (6) Press "Start" to start exporting.
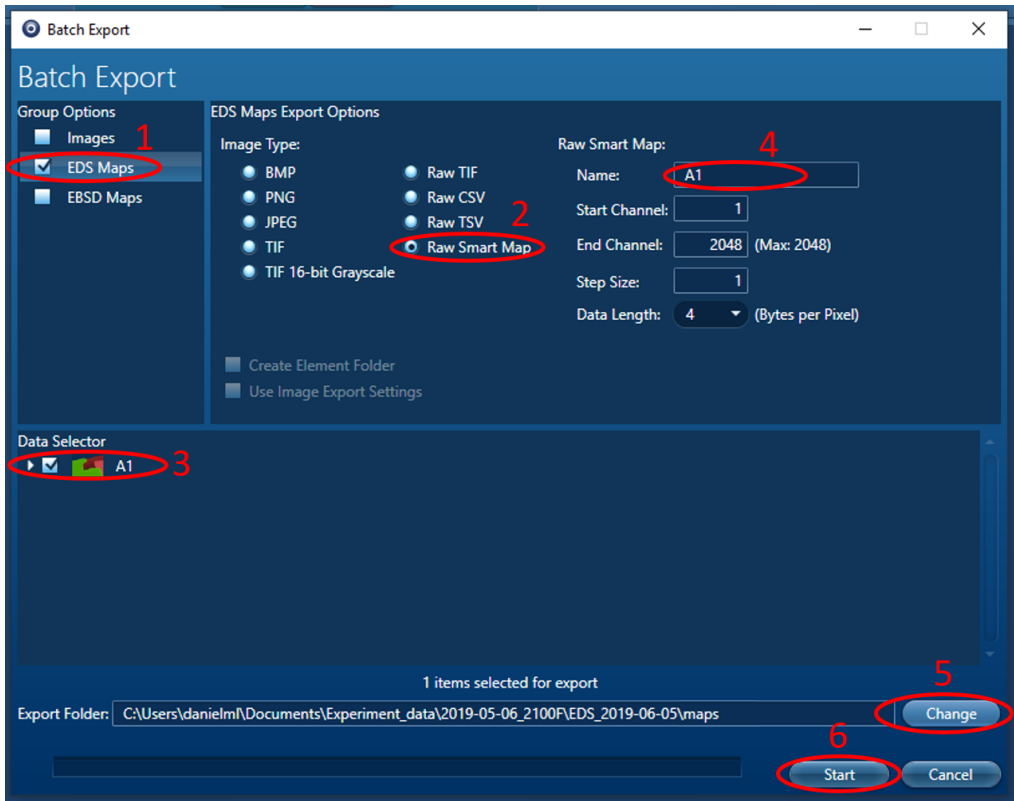
AZtec will inform you when the procedure is finished. Then, the "maps" folder should contain a ".raw" file and a ".rpl" file:

Choose "Analyzer" mode and "Acquire Spectra" step.

The main window should now contain the sum spectrum. Right click the spectrum, then Export → EMSA

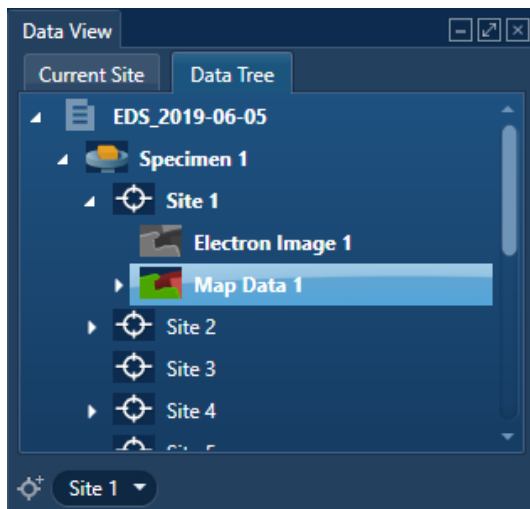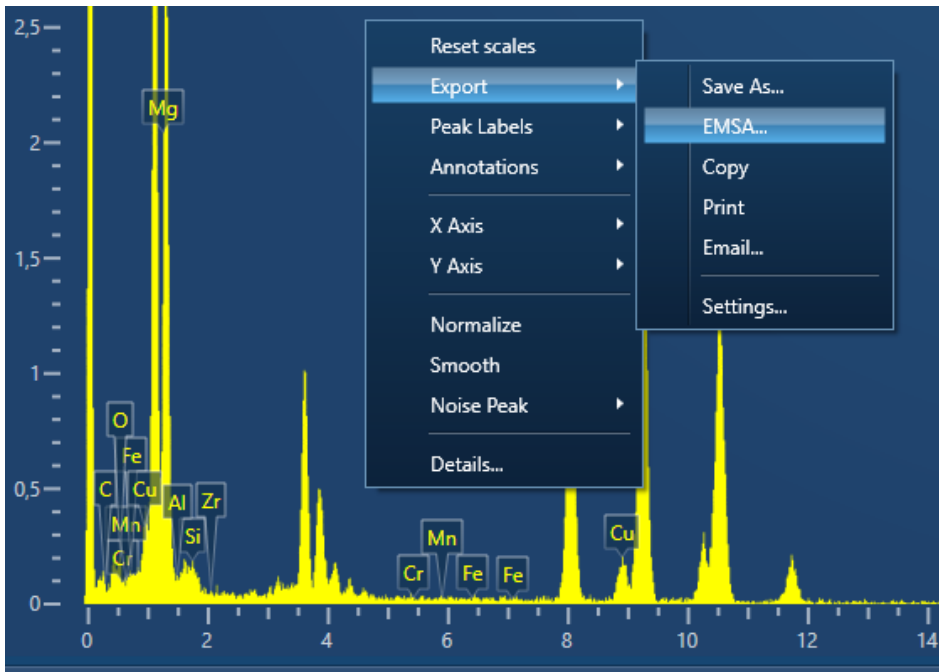(1) Choose the "maps" folder. (2) Choose the "*.emsa" option, (3) rename to your label and (4) press "Save".
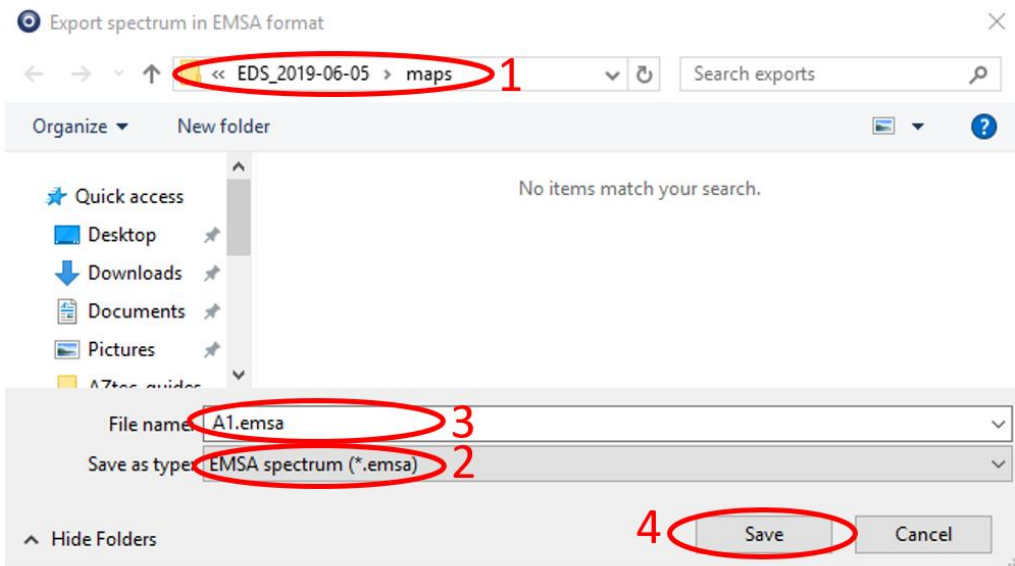
Choose "Map" mode, and the "Construct Maps" step.
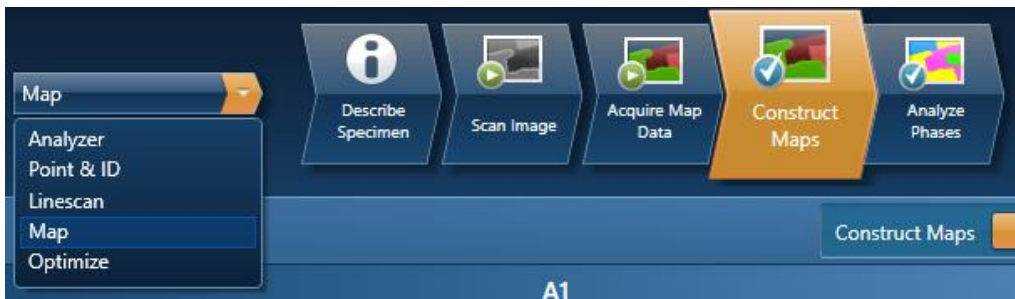
The main window should now show a number of "element maps". Right-click any element map, end press "Details".
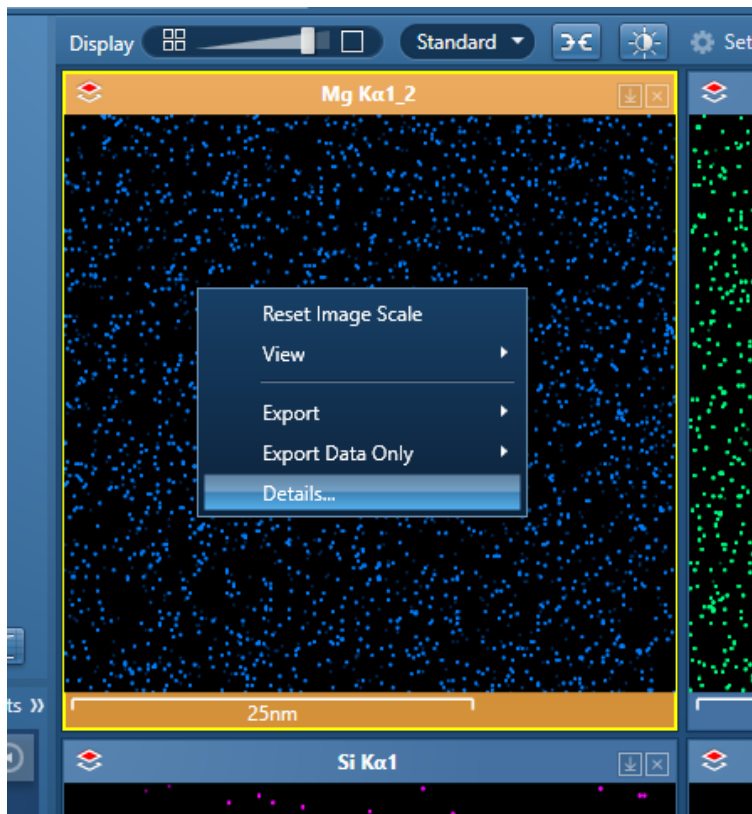
Press "Copy" to copy the items.

Open a new Notepad window. (1) Paste the data into the window. (2) Use the label as filename, (3) choose encoding UTF-8 and (4) save the file.
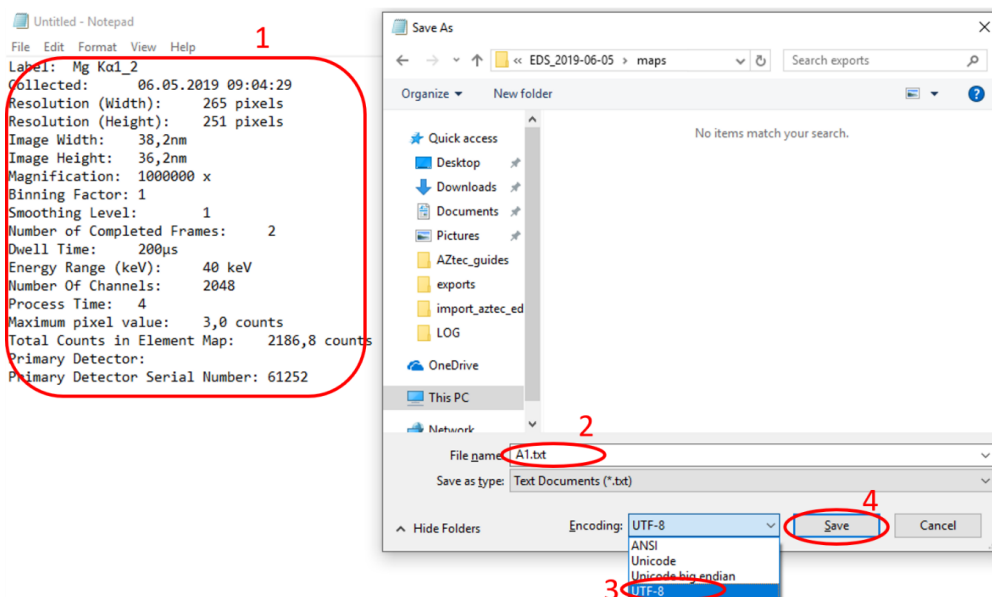
When finished, the files need to be combined into a single file ".hdf5" file containing the EDX map. A simple Windows program has been made for this purpose, called "Export EDX maps from AZtec". This program has an embedded Python script which does the conversion.

Open the program "Export EDX maps from AZtec" on the desktop.
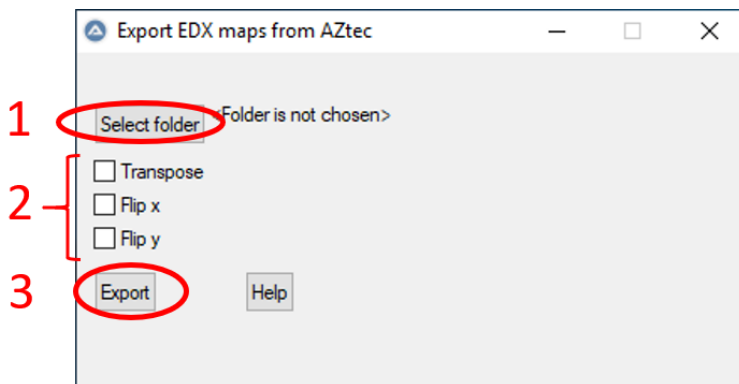
(1) Select the folder "maps".

(2) Choose whether the EDX maps should be:

- Transposed: *x* and *y* axes interchanged
- Flip x: Make the *x* axis reversed
- Flip y: Make the *y* axis reversed

(3) Click Export

If the script is running for very long without action, it might be necessary to hit "Enter".

When the export procedure is finished, the "maps" folder should contain an ".hdf5" file.

Name	Date modified
A1.emsa	26.04.2019 09:41
A1.hdf5	27.05.2019 19:34
A1.raw	26.04.2019 09:40
A1.rpl	26.04.2019 09:40
A1.txt	26.04.2019 09:44

The conversion program supports batch conversion of multiple EDX maps within the same folder, as long as the files are labeled properly.

It is possible to use the embedded Python conversion script directly; it is located in the same folder as this guide. Run the script with the working folder as argument (defaults to the current folder if not specified). The keywords "--transpose", "--flipx" and "--flipy" can be used.

Exporting EDX linescans (don't do this)

Exporting EDX linescans from AZtec is a non-trivial, tedious task and is not recommended. Instead of acquiring EDX linescans, acquire EDX maps with very high aspect ratio.

Written by Daniel Lundeby, master student at the TEM group.

May 28th, 2019

A.3 Script for exporting EDX maps

When exporting EDX maps, data needs to be combined from several sources into a single `.hdf5` file. A script has been made, which combines the data automatically. The source code is attached below.

```python
 1  ##################################################
 2  # Script for exporting EDX maps from AZtec
 3  ##################################################
 4
 5  print('Loading Python libraries')
 6
 7  import os
 8  import sys
 9  import hyperspy.api as hs
10  import numpy as np
11  import json
12
13  print()
14
15  path = '.\\'
16
17  for arg in sys.argv[1:]:
18      if not arg.startswith('-'):
19          path = arg.rstrip('\\') + '\\'
20          break
21
22
23  transpose = False
24  if '--transpose' in sys.argv:
25      transpose = True
26
27  flipx = False
28  if '--flipx' in sys.argv:
29      flipx = True
30
31  flipy = False
32  if '--flipy' in sys.argv:
33      flipy = True
34
35  def main():
36      labels = []
37      contents = os.listdir(path)
38      for filename in contents:
39          fn_spl = filename.split('.')
40          if len(fn_spl) == 1:
41              continue
42          label, filetype = ''.join(fn_spl[:-1]), fn_spl[-1]
43          if filetype == 'raw':
44              labels.append(label)
45
46      for label in labels:
47          print('Processing', label)
48          pathlabel = path + '\\' + label
49          convert_aztec_to_hdf5(pathlabel, transpose, flipx, flipy)
50
51      if len(labels) == 0:
52          print('Couldn\'t find any files to process')
53
54
55  def convert_aztec_to_hdf5(pathlabel, transpose=False, flipx=False, flipy=False):
56      """
57      Convert AZtec EDX map referenced by `pathlabel` to an `.hdf5` file, and save this file to
   the same folder.
58
59      The function assumes the following files exist:
60
61      * `.raw`: The raw EDX data.
62      * `.rpl`: Information about the structure of the raw data.
63      * `.emsa`: Sum spectrum, with calibration data and metadata.
64      * `.txt`: Additional metadata.
65
66      :param pathlabel: Full path of the files containing EDX information, including label but
   without extension. Example: `C:/Users/john/Documents/EDX/A1`. In this case, `A1` is the label
   and the following files are assumed to exist: `A1.raw`, `A1.rpl`, `A1.emsa`, `A1.txt`.
67      :param transpose: Whether to interchange the `x` and `y` axes.
68      :param flipx: Whether to make the `x` axis reversed.
69      :param flipy: Whether to make the `y` axis reversed.
70      :return: The `.hdf5`signal which has been created.
```

```python
 71        """
 72
 73        fn_rpl = pathlabel + '.rpl'
 74        fn_emsa = pathlabel + '.emsa'
 75        fn_txt = pathlabel + '.txt'
 76
 77
 78        # Load spectrum
 79        # The .rpl file uses data from the .raw file.
 80        # For some reason, the signal needs to be transposed.
 81        s = hs.load(fn_rpl, signal_type='EDS_TEM').T
 82
 83        # Load sum spectrum
 84        # The sum spectrum contains some metadata which is not contained in the .rpl file
 85        s_sum = hs.load(fn_emsa, signal_type='EDS_TEM')
 86        s.get_calibration_from(s_sum)
 87
 88        # The EDX detector real time and live time needs to divided by the number of pixels
 89        pixels=1
 90        for axis in s.axes_manager.navigation_axes:
 91            pixels *= axis.size
 92        s.metadata.Acquisition_instrument.TEM.Detector.EDS.real_time /= pixels
 93        s.metadata.Acquisition_instrument.TEM.Detector.EDS.live_time /= pixels
 94
 95        # Some properties are not transfered by s.get_calibration_from
 96        def transfer(item):
 97            s.metadata.set_item(item, s_sum.metadata.get_item(item))
 98        transfer('General.date')
 99        transfer('General.time')
100
101        # Load metadata
102        meta_np = np.genfromtxt(fn_txt, encoding='utf-8-sig', delimiter=':\t', dtype='str')
103        meta = dict(meta_np)
104
105        # Set properties from metadata
106        ax_ids = ['width', 'height']
107        ax_names = ['x', 'y']
108        sizes_id = ['Image Width', 'Image Height']
109        pxs_id = ['Resolution (Width)', 'Resolution (Height)']
110
111        for ax_id, ax_name, size_id, px_id in zip(ax_ids, ax_names, sizes_id, pxs_id):
112            ax = s.axes_manager[ax_id]
113            size, size_unit = split_property(meta[size_id])
114            px, px_unit = split_property(meta[px_id])
115            ax.scale = float(size.replace(',', '.')) / float(px)
116            ax.units = size_unit
117            ax.name = ax_name
118
119        if transpose:
120            s = s.transpose(signal_axes=[2], navigation_axes=[1, 0])
121            s.axes_manager[0].name = ax_names[0]
122            s.axes_manager[1].name = ax_names[1]
123
124        if flipx:
125            s.data = np.flip(s.data, axis=1)
126
127        if flipy:
128            s.data = np.flip(s.data, axis=0)
129
130        s.save(pathlabel, extension='hdf5', overwrite=True)
131
132        return s
133
134
135 def split_property(text):
136        lim = None
137        for i in range(len(text) - 1, -1, -1):
138            if text[i].isnumeric():
139                lim = i + 1
140                break
141        return text[:lim], text[lim:]
142
143
```

```python
144 def get_index(string):
145     s = ".".join(string.split('.')[:-1]).split('-')[0]
146     start = -1
147     for i in range(len(s)-1, -1, -1):
148         if not s[i].isdigit():
149             start = i
150             break
151     return s[start+1:]
152
153
154 def load_json(path):
155     with open(path) as file:
156         return json.load(file)
157
158 main()
159
160 input('Press Enter to exit')
161
```

Appendix B

Beam current measurements

A script has been made which measures the beam current consistently using the CCD camera. The script has been made in the DigitalMicrograph scripting language, and can be used inside DigitalMicrograph. The following guide shows how to use the script, along with details on how the script works.

B.1 Using the beam current measurement script

Before using the script, the number of counts per pixel needs to be set. To do this, navigate to the function `approachMaxIntensity` and look for the following lines of code:

```
AddObjectToList(aims, alloc(NumClass).Init(12000));
AddObjectToList(aims, alloc(NumClass).Init(12000));
AddObjectToList(aims, alloc(NumClass).Init(12000));
AddObjectToList(aims, alloc(NumClass).Init(12000));
```

By default, the number of counts per pixel is 12000. To change this, substitute 12000 by the desired number[1]. The script tunes the exposure time iteratively; because there are four code lines, the tuning of exposure time is done four times.

The script can be run in two modes. Choose one of these modes before using the script:

---

[1] 12000 is a useful number for the JEOL 2100 CCD, which saturates at ~ 16000 counts per pixel. The JEOL 2100F CCD saturates at a higher number of counts per pixel, so then this number should be increased.

1. Default mode: Acquire a given number of CCD images. To use this mode, include the following line: `acquisitionSeries(exp, imgtags, 9);`. In this case, 9 images are acquired.

2. Alternative mode: Acquire CCD images for a given number of minutes. To use this mode, include the following line: `acquisitionSeriesForDuration(` ↪ `exp, imgtags, 30);`. In this case, images are acquired subsequently for a duration 30 min.

Before using the script, it needs to be installed. To do this, follow the instructions below:

- Navigate to `File → Install Script File`.

- Locate and open the script file.

- Choose the desired command name (e.g. "Measure beam current") and menu (e.g. "Zeta"), and press "OK".

This creates a menu item at the chosen location inside DigitalMicrograph. To measure the beam current, press this menu item and follow the instructions. Note that the electron beam should cover most of the screen when measuring the beam current (see figure 4.2 for how this should look like).

The beam current script acquires a series of ten measurements by default. When the measurements are done, it is necessary to choose where to save the results. It is convenient to have a dedicated folder, e.g. "beam_current/", for all beam current results. The results are stored as a `.dm3` file (referred to as a "reference image"). The `.dm3` file itself contains a CCD image of beam current (this is useful for analyzing the beam profile in retrospect; see figure 4.2).

The individual measurements are stored as metadata in the `.dm3` file. To see the metadata in DigitalMicrograph, open the `.dm3` file, right-click the image → "Image Info" → "Tags". The results are stored in the tag group called "Acquisition_series". There are two relevant tag groups here: "Sum" and "Time". "Sum" contains a list of the CCD sum counts of each measurement. "Time" contains the exact time at which each measurement was done. The exposure time, which is constant for all measurements, is stored in the tag "DataBar" → "Exposure Time (s)". Now, to calculate the beam current I, the following formula can be used:

$$I = \frac{\text{CCD sum counts}}{\text{exposure time}} \cdot \frac{1}{\text{conversion efficiency}} \cdot e \qquad \text{(B.1)}$$

e is the elementary charge (number of electrons per unit charge). The conversion efficiency is the number of CCD counts per primary electron. This is discussed for the JEOL 2100 in section 5.1.1. Note that the formula gives the beam current in

Ampere. The beam current in TEMs is commonly stated in nA - this is also the HyperSpy convention.

It is possible to read the `.dm3` file using HyperSpy. Python code for retrieving and analyzing the beam current in a convenient way is described in section C.1.2.

B.2 Details on how the beam current measurement script works

When the beam current script is running, the following steps are executed.

- Tune the exposure time to obtain the desired number of counts per pixel.

- Acquire a reference CCD image as a `.dm3` file.

- Acquire a series of subsequent CCD images. Store the sum counts and the time as metadata inside the reference image.

The script ensures consistent measurements by always using the same CCD camera settings.

- `CM_SetProcessing( acq_params, 3 );` Apply dark and gain correction

- `CM_SetCorrections( acq_params, 1911, 887);` Apply corrections as specified by the word "887"

The number 887 is interpreted as binary, and it means that the following corrections are applied (these are the default correction when acquiring a CCD image manually):

- Defect correction

- Deinterlace correction

- Extraction correction

- Bias correction

- Linearization correction

- Dark correction

- Gain correction

The DigitalMicrograph User's Guide has been used as reference for the DigitalMicrograph scripting language [35]. For details on how to interact with the CCD camera as well as with other parts of the TEM, refer to the highly useful tutorial at Dave Mitchell's DigitalMicrograph's website [36] (this is not covered by the User's Guide).

B.3   Source code

The DigitalMicrograph script for beam current measurements is attached below.

```
 1    // ***********************************************************************
 2    // DigitalMicrograph script to find beam current from the CCD camera
 3    // ***********************************************************************
 4    //
 5    // The script is useful when using the zeta-factor method
 6    //
 7    // Author: Daniel Lundeby
 8    // May 2019
 9    //
10
11
12    // Define an wrapper class around Number
13    Class NumClass : Object
14    {
15        Number var;
16        Object init(object self, number v) {
17            var = v
18            return self;
19        }
20        Number get(object self) {
21            return var;
22        }
23    }
24
25
26    // Calculate the maximum intensity of an image
27    number calcMax(Image img) {
28        number min, max;
29        ImageCalculateMinMax( img, 1,  0, min, max );
30        return max;
31    }
32
33
34    // Create a metadata tag as a number
35    void createTagNumber(TagGroup imgtags, String tagfolder, String tagname, Number value) {
36        TagGroup innerTG = TagGroupGetOrCreateTagGroup( imgtags, tagfolder);
37        if (! TagGroupDoesTagExist( innerTG, tagname )) {
38            TagGroupCreateNewLabeledTag(innerTG, tagname);
39        }
40        TagGroupSetTagAsNumber(innerTG, tagname, value );
41    }
42
43
44    // Create a metadata tag as a string
45    void createTagString(TagGroup imgtags, String tagfolder, String tagname, String value) {
46        TagGroup innerTG = TagGroupGetOrCreateTagGroup( imgtags, tagfolder);
47        if (! TagGroupDoesTagExist( innerTG, tagname )) {
48            TagGroupCreateNewLabeledTag(innerTG, tagname);
49        }
50        TagGroupSetTagAsString(innerTG, tagname, value );
51    }
52
53
54    // Create acquisition parameters to be used by the CCD camera
55    Object createAckParams(Object camera, Number exposure) {
56        Object acq_params = CM_GetCameraAcquisitionParameterSet_HighQualityImagingAcquire(
      camera );
57        CM_SetExposure( acq_params, exposure );
58        CM_SetProcessing( acq_params, 3 ); // Gain and dark correction
59        CM_SetCorrections( acq_params, 1911, 887); // Additional, default corrections
60        if ( CM_IsValid_AcquisitionParameters( camera, acq_params ) ) {
61            return acq_params;
62        }
63        else {
64            result("Not valid acquisition parameters\n");
65        }
66    }
67
68
69    // Capture a CCD image
70    Image captureImage(Number exposure) {
71        Object camera = CM_GetCurrentCamera();
72        Object acq_params = createAckParams(camera, exposure)
73        if (! acq_params) {
74            return null;
75        }
```

```
76          return CM_AcquireImage( camera, acq_params );
77      }
78
79
80      // Find the exposure time which causes the max intensity to reach a certain value, by
        iteration
81      Number approachMaxIntensity() {
82
83          Object aims = alloc(ObjectList);
84          AddObjectToList(aims, alloc(NumClass).Init(12000)); // First aim of intensities
85          AddObjectToList(aims, alloc(NumClass).Init(12000)); // Second aim of intensities
86          AddObjectToList(aims, alloc(NumClass).Init(12000)); // Third aim of intensities
87          AddObjectToList(aims, alloc(NumClass).Init(12000)); // Fourth aim of intensities
88
89          Number exp = 0.001; //  Initial exposure time, in seconds
90
91          foreach (Object aim; aims) {
92              Image img = captureImage(exp);
93              result("Exposure time: " + exp + " s, max intensity: " + calcMax(img) + "\n");
94              Number factor = aim.get() / calcMax(img);
95              exp = exp*factor;
96              if (exp > 5) { // Set maximum exposure time in seconds
97                  exp = 5;
98              }
99          }
100         return exp;
101
102     }
103
104
105     // Save metadata to the .dm3 image, and print to console
106     void saveMetadataAndPrint(Image img, TagGroup imgtags, number index) {
107         number counts = sum(img);
108         number ma = calcMax(img);
109         string datetime = FormatTimeString( GetCurrentTime(), 1+16*2);
110         createTagNumber(imgtags, "Acquisition series:Sum", "Sum " + index, counts);
111         createTagString(imgtags, "Acquisition_series:Time", "Time_" + index, datetime);
112         createTagNumber(imgtags, "Acquisition series:Max", "Max " + index, ma);
113         result("Max intensity: " + ma + ", sum: " + counts + "\n");
114     }
115
116
117     // Acquire a given number of CCD images
118     void acquisitionSeries(Number exp, TagGroup imgtags, Number repetitions) {
119
120         result("Acquiring " + repetitions + " images" + "\n");
121
122         Number i = 0;
123         while (i < repetitions) {
124             Image img = captureImage(exp);
125             saveMetadataAndPrint(img, imgtags, i+2);
126             i++;
127         }
128
129     }
130
131
132     // Acquire CCD images as often as possible, for a given number of minutes
133     void acquisitionSeriesForDuration(Number exp, TagGroup imgtags, Number minutes) {
134
135         Number startTime = GetCurrentTime();
136         Number endTime = startTime + minutes*60*10000000;
137
138         result("Ending at " + FormatTimeString( endTime, 1+16*2) + "\n");
139
140         Number i = 0;
141         while (GetCurrentTime() < endTime) {
142             Image img = captureImage(exp);
143             saveMetadataAndPrint(img, imgtags, i+2);
144             i++;
145         }
146     }
147
148
149     void run() {
150
```

```
151        Object camera = CM_GetCurrentCamera();
152        if (!CM_GetCameraInserted(camera)) {
153            //CM_SetCameraInserted(camera, 1);
154            OkDialog("You need to insert the camera before measuring the current\n");
155            return;
156        }
157
158        number cont = ContinueCancelDialog("Confirm that the beam is focused at a hole, and
       covers most of the CCD.\n\nPress Continue to perform the calculation.");
159        if (cont==0) {
160            return;
161        }
162
163        Result("\nStarting exposure series \n");
164        Number exp = approachMaxIntensity();
165        Result("Ending exposure series. Final exposure: " + exp + "s\n");
166
167        Result("Starting acquisition series\n");
168        // Capture image for saving, START
169        Object acq_params = createAckParams(camera, exp)
170        if (! acq_params) {
171            return;
172        }
173        Image img = CM_CreateImageForAcquire( camera, acq_params, "image");
174        CM_AcquireImage( camera, acq_params, img );
175        TagGroup imgtags = img.imagegettaggroup();
176        saveMetadataAndPrint(img, imgtags, 1);
177        // Capture image for saving, END
178
179
180        // Choose one of the following options:
181        acquisitionSeries(exp, imgtags, 9); // Acquire the given number of CCD images
182        //acquisitionSeriesForDuration(exp, imgtags, 30); // Acquire CCD images for the
       given number of minutes
183
184        Number saveAfter = 0; // Whether to save a picture after ending acquisition series
185        Image imgAfter;
186        if (saveAfter) {
187            imgAfter = CM_CreateImageForAcquire( camera, acq_params, "image");
188            CM_AcquireImage( camera, acq_params, imgAfter );
189        }
190        Result("Ending acquisition series\n");
191
192        Number current_estimate = Sum(img) / exp / 1.5 * 1.6e-19 * 1e9
193        Result("Rough beam current estimate: " + current_estimate + " nA\n");
194
195        string path = "";
196        SaveAsDialog( "Choose where to save the picture", "current", path);
197        if (path != "") {
198            SaveAsGatan( img, path );
199            result("File saved at: " + path + "\n");
200            if (saveAfter) {
201                SaveAsGatan( imgAfter, path+" after" );
202                result("File saved at: " + path+"_after" + "\n");
203            }
204        }
205
206  }
207
208  run();
209
```

Appendix C

Python code for data analysis

This appendix describes the Python code which has been implemented for analyzing EDX data in this project. The reader is assumed to have basic knowledge of Python, as well as some advanced concepts such as Python modules, classes and lambda functions.

A choice was made to implement code which permits fast, consistent analysis of dataset containing multiple spectra. For this project, one dataset typically contains 30 single spectra. As a consequence of this choice, code has been implemented inside a Python module, which has been called `uts.py` (short for "utilities"). The code for analyzing datasets is made in Jupyter notebooks, which uses methods and classes from the `uts.py` module.

This appendix contains instructions on how to use the `uts.py` module. The module contains two main classes which are used to analyze EDX spectra:

- `SpotAnalyzer`: Used to analyze a series of single EDX spectra, such as a tilt series.
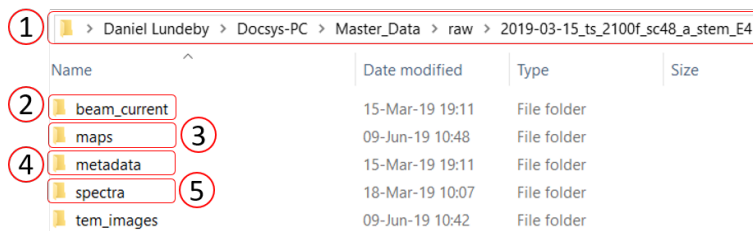
- `MapAnalyzer`: Used to analyze a series of EDX maps.

The `SpotAnalyzer` and `MapAnalyzer` classes use a class called `BeamCurrentAnalyzer` ↪ internally. In the following subsections, instructions for using all of these classes are described.

C.1 Instructions for using the `uts.py` module

C.1.1 Prerequisites

In order to use the `uts.py` module, it first needs to be installed using a Python package manager (e.g. Anaconda or pip). As an easier solution for testing the code quickly, the `uts.py` module can be placed in the same location as the Jupyter notebook which uses the module.

The `uts.py` module assumes the EDX data to be stored with a specific folder structure:

Figure C.1: Folder structure for analyzing EDX data using the `uts.py` module.

1. The EDX data is stored in a folder, which is recommended to be in a separate location from the Jupyter notebook.

2. All `.dm3` files containing beam current measurements are in a folder called "beam_current/".

3. All EDX maps (which usually have the file ending `.hdf5`) are in a folder called "maps/".

4. Metadata, such as the stage tilt, could be stored in a folder called "metadata/".

5. All single EDX spectra (which usually have the file ending `.emsa` are in a folder called "spectra".)

C.1.2 The BeamCurrentAnalyzer class

The BeamCurrentAnalyzer class is used to read `.dm3` files containing beam current measurements (see section B) in Python. The class requires the conversion factor as input. Note that the `SpotAnalyzer` and `MapAnalyzer` classes use the `BeamCurrentAnalyzer` internally. Thus, all function which are available for the `BeamCurrentAnalyzer` are available for these classes as well. The functionality

of the `BeamCurrentAnalyzer` class is illustrated by a Jupyter Notebook attached below.

BeamCurrentAnalyzer - Demo

In [1]: ►
```python
%matplotlib inline
import numpy as np
import matplotlib.pyplot as plt
import hyperspy.api as hs
import uts        # Importing the uts.py module
import importlib
```

. . .

Loading data and initializing the BeamCurrentAnalyzer class

In [2]: ►
```python
params = {
    'folder_current': r'C:\Users\danie\Docsys-PC\Master_Data\raw\2019-05-
09_ts_2100_gasb_a\beam_current_measurements\beam_size', # Path to the folder containing the .dm3
files.
    'format': 'size{d}',      # Format of .dm3 files. Optional.
    'counts_per_electron': 1.47,     # Specify the conversion efficiency
}
a = uts.BeamCurrentAnalyzer(params)
```

Analyzing the data

List the beam currents

In [3]: ►
```python
a.get_beam_current()
```

Out[3]: ([datetime.datetime(2019, 5, 9, 13, 33, 44),
    datetime.datetime(2019, 5, 9, 13, 36, 7),
    datetime.datetime(2019, 5, 9, 13, 37, 40),
    datetime.datetime(2019, 5, 9, 13, 39, 8),
    datetime.datetime(2019, 5, 9, 13, 40, 30),
    datetime.datetime(2019, 5, 9, 13, 41, 54),
    datetime.datetime(2019, 5, 9, 13, 43, 14),
    datetime.datetime(2019, 5, 9, 13, 44, 50),
    datetime.datetime(2019, 5, 9, 13, 46, 9),
    datetime.datetime(2019, 5, 9, 13, 47, 27),
    datetime.datetime(2019, 5, 9, 13, 48, 37),
    datetime.datetime(2019, 5, 9, 13, 49, 47),
    datetime.datetime(2019, 5, 9, 13, 51, 7),
    datetime.datetime(2019, 5, 9, 13, 52, 20),
    datetime.datetime(2019, 5, 9, 13, 53, 37),
    datetime.datetime(2019, 5, 9, 13, 54, 52),
    datetime.datetime(2019, 5, 9, 13, 56, 6),
    datetime.datetime(2019, 5, 9, 13, 57, 15),
    datetime.datetime(2019, 5, 9, 13, 58, 22)],
    [1.785016100700017

Plot beam currents

`# Each blue spot is the beam current measured at the particular spot. Note that each spot is based`
`# on ten individual measurements. The spot is the median of the ten measurements.`

`a.plot_beam_current()`

`(<Figure size 432x288 with 1 Axes>,`
`<matplotlib.axes._subplots.AxesSubplot at 0x2646b1077f0>)`
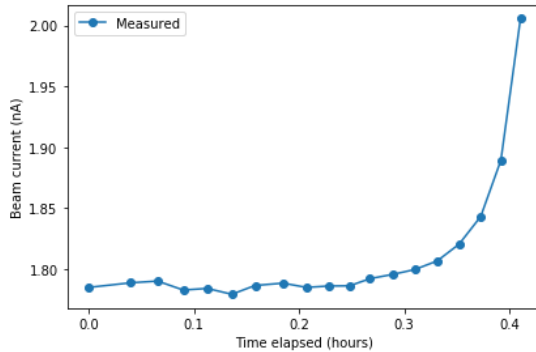
`# The same plot as above, shown at greater detail. The green spots indicate the ten individual`
`# measurements. The blue spot is chosen as the median of the ten measurements. Note that the x`
`# position of each measurements corresponds exactly to the time at which the measurement was done.`

`a.plot_beam_current(full=True)`
`plt.xlim(-0.01, 0.12)`
`plt.ylim(1.7775, 1.796)`

`(1.7775, 1.796)`
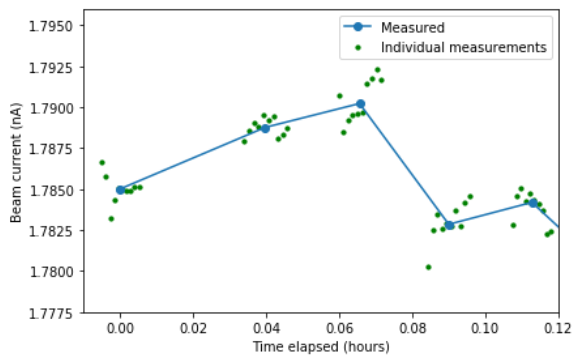
C.1.3 Using the SpotAnalyzer class

The SpotAnalyzer class is made for analyzing multiple EDX spectra taken in spot mode, such as from a tilt series experiment. Each EDX spectrum is given a label (e.g. "B3"), which is the same as the filename of the EDX spectrum. To demonstrate how to use the SpotAnalyzer class, a demo notebook has been made.

SpotAnalyzer - Demo

Regions:

- A: GaAs, ZB
- B: GaAsSb
- C: GaAs, WZ
- D: Pure GaAs, amorphous

Setup

```
In [1]:   %matplotlib inline
          import numpy as np
          import matplotlib.pyplot as plt
          import hyperspy.api as hs
          import uts    # Import the uts.py module
```

...

```
In [2]:   # Define function to get the thickness from a signal
          def get_thick(s):
              reg = uts.get_region(s)

              if reg in ['A', 'B', 'C']:     # A, B and C are at the nanowire
                  width = 104e-9    # in meters
                  return uts.get_thickness(s, width, params['zone_tilt'], hexagonal=True)

              if reg in ['D']:    # D is at the Ga catalyst droplet
                  return 108e-9
```

```
In [3]:  ▶| # Define a dictionary `params`, which contains all information necessary to create a SpotAnalyzer
            object
            params = {
                'id': 'ts_2100_sc48_c_stem',     # Unique id for the dataset
                'folder': r'C:\Users\danie\Docsys-PC\Master_Data\raw\2019-04-
            08_ts_2100_sc48_c_E2_3\STEM_EDS_session',     # Folder containing the EDX data
                'region_names': {     # Give each region a name. These names can be used when plotting data.
                    'A': 'ZB',
                    'B': 'insert',
                    'C': 'WZ',
                    'D': 'amorphous'
                },
                'all_elements': ['Ga', 'As', 'Sb', 'Cu', 'C', 'O', 'Si', 'Fe'],     # Specify all elements which
            are present in the samples. Useful when plotting spectra.
                'spectrum_calibration_scale': 0.010034,     # Optional. Tune the scale of the spectrum.
                'spectrum_calibration_offset': -0.2105,     # Optional. Tune the offset of the spectrum.
                'beam_current': 'from_measurement_files',     # Specify that you want to obtain beam currents
            from .dm3 measurement files. Alternatively, supply beam currents as a dictionary in the format
            {'A1': 1.15, 'A2': 1.18, ...}.
                'counts_per_electron': 1.47,     # Conversion efficiency of the CCD
                'beam_current_strategy': 'interp_fill',     # Set the beam current of each spectrum by
            interpolation the beam current measurements. Other options are `regr`, `mean` and `middle`.
                'intensity': 'model_fitting',     # Either `model_fitting` or `window_method`. Specifies how the
            X-ray intensities should be retrieved from the EDX spectra
                'mod_elements': {     # If model fitting: Specify which elements should be model fitted.
                    'A': ['As', 'Cu', 'Ga'],
                    'B': ['As', 'Cu', 'Ga'],
                    'C': ['As', 'Cu', 'Ga'],
                    'D': ['Cu', 'Ga']
                },
                'mod_lim': {     # If model fitting: Specify the energy range (in keV) which is used for model
            fitting.
                    'A': slice(2.5, 20.0),
                    'B': slice(5.0, 20.0),
                    'C': slice(2.5, 20.0),
                    'D': slice(2.5, 20.0),
                },
                'bw_pos': {'Ga_Ka': [4, 3], 'As_Ka': [3.5, 2.5]},     # If window method: Specify the background
            window positions of each peak, as multiples of the FWHM of the peak.
                'iw_width': 1.2,     # Specify the width of the integration window
                'composition': {     # Sample composition at each region, in at%. Internally, the compositions
            are converted to wt%.
                    'A': {'Ga': 0.5, 'As': 0.5},
                    'C': {'Ga': 0.5, 'As': 0.5},
                    'D': {'Ga': 1}
                },
                'zone_tilt': -6.41,     # Stage tilt (in degrees) at which the nanowire is orthogonal to the
            electron beam (110 zone axis). Used for thickness correction.
                'zone_axes': {-6.41: '110', 23.99: '112'},     # Specify which zone axes are at which stage
            tilts (in degrees)
                'thickness': get_thick,     # Function for retrieving thickness from each signal
                'density': {     # in kg/m^3
                    'A': 5317.6,     # Density of region A, which is GaAs
                    'C': 5317.6,     # Density of region C, which is GaAs
                    'D': hs.material.elements.Ga.Physical_properties.density_gcm3 * 1e3     # Density of region
            D, which is pure Ga
                },
                'regions': ['A', 'C', 'D'],     # Regions to find zeta-factors from
                'xray_lines': ['Ga_Ka', 'As_Ka'],     # X-ray lines to find zeta-factors from
                'exclude': ['1', '5-1']     # Exclude individual points from the dataset
            }
```

```
In [4]:  ▶| # Create the SpotAnalyzer object
            a = uts.SpotAnalyzer(params)
```

```
Loading model fitting results from cache
```

Analyzing the data

The signals as stored in the `signals` attribute of the SpotAnalyzer class. The current dataset contains 56 single spectra.

```
In [5]:    a.signals
```
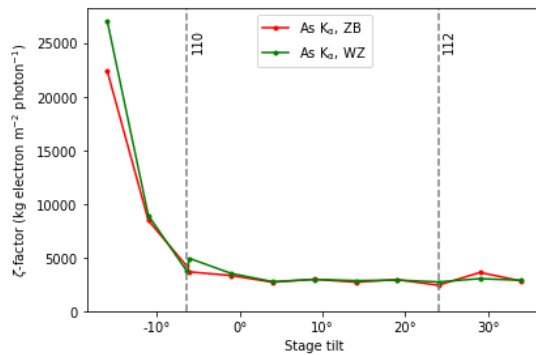
```
Out[5]:    [<EDSTEMSpectrum, title: A1, dimensions: (|2048)>,
            <EDSTEMSpectrum, title: B1, dimensions: (|2048)>,
            <EDSTEMSpectrum, title: C1, dimensions: (|2048)>,
            <EDSTEMSpectrum, title: D1, dimensions: (|2048)>,
            <EDSTEMSpectrum, title: A2, dimensions: (|2048)>,
            <EDSTEMSpectrum, title: B2, dimensions: (|2048)>,
            <EDSTEMSpectrum, title: C2, dimensions: (|2048)>,
            <EDSTEMSpectrum, title: D2, dimensions: (|2048)>,
            <EDSTEMSpectrum, title: A3, dimensions: (|2048)>,
            <EDSTEMSpectrum, title: B3, dimensions: (|2048)>,
            <EDSTEMSpectrum, title: C3, dimensions: (|2048)>,
            <EDSTEMSpectrum, title: D3, dimensions: (|2048)>,
            <EDSTEMSpectrum, title: A4, dimensions: (|2048)>,
            <EDSTEMSpectrum, title: B4, dimensions: (|2048)>,
            <EDSTEMSpectrum, title: C4, dimensions: (|2048)>,
            <EDSTEMSpectrum, title: D4, dimensions: (|2048)>,
            <EDSTEMSpectrum, title: A5-1, dimensions: (|2048)>,
            <EDSTEMSpectrum, title: B5-1, dimensions: (|2048)>,
            <EDSTEMSpectrum, title: C5-1, dimensions: (|2048)>,
            <EDSTEMSpectrum, title: D5-1, dimensions: (|2048)>,
```

Plot tilt series

Plot a tilt series only containing the `Ga_Ka` points

```
In [6]:    a.plot_tilt_series(xray_lines=['As_Ka'])
```

```
Out[6]:    (<Figure size 432x288 with 1 Axes>,
            <matplotlib.axes._subplots.AxesSubplot at 0x21cc4073c50>)
```
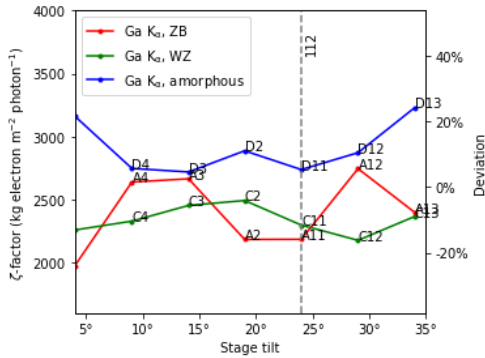

Plot a tilt series at a limited region, with labeled spots and with deviation

```
a.plot_tilt_series(xray_lines=['Ga_Ka'], annotate='all', ann_off=0, xmin=4, xmax=35, ymin=1600,
ymax=4000, ref=2600)
```

Out[7]: (<Figure size 432x288 with 2 Axes>,
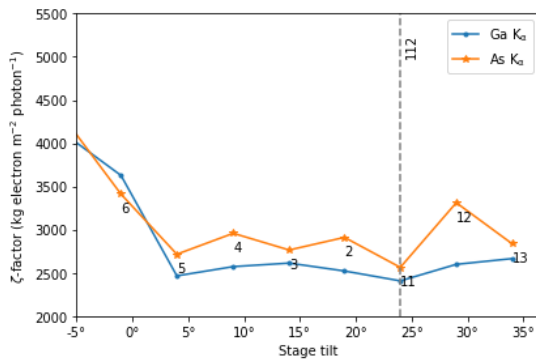   <matplotlib.axes._subplots.AxesSubplot at 0x21cc42582e8>)

Create a clone object to see the effect of beam current correction

```
args = {'xmin': -5, 'ymin': 2000, 'ymax': 5500, 'annotate': 'single', 'avg': 'xray_lines', 'color':
None, 'ann_id': 1, 'ann_off': -0.06}    # It is possible to specify function arguments as a
dictionary
```

```
# Case 1: Account for differences in beam current (this is done by default)
a.plot_tilt_series(**args)
```

Out[9]: (<Figure size 432x288 with 1 Axes>,
         <matplotlib.axes._subplots.AxesSubplot at 0x21cc52cef98>)

In [10]: ▶| # Case 2: Set the beam current to be constant
         b = a.update(beam_current=0.057)
         b.plot_tilt_series(**args)

         Loading model fitting results from cache

Out[10]: (<Figure size 432x288 with 1 Axes>,
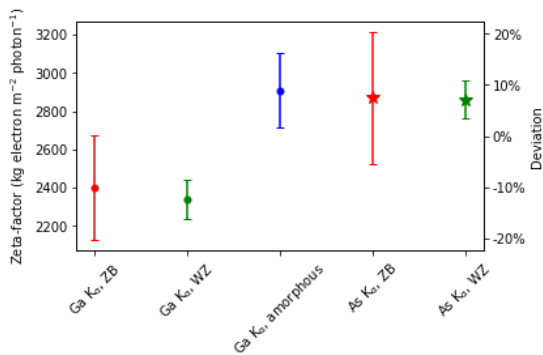   <matplotlib.axes._subplots.AxesSubplot at 0x21cc3f43c18>)
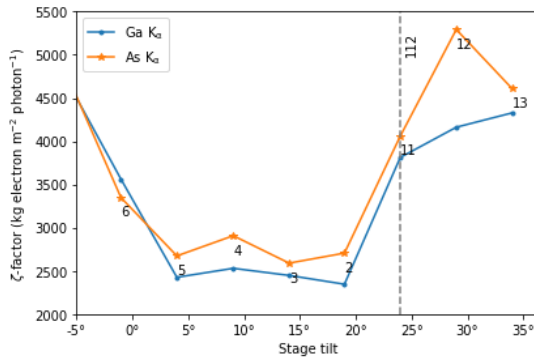
Analyze zeta-factors

In [11]: ▶| indices=['5-2', '4', '3', '2', '11', '12', '13'] # These are the indices from which zeta-factors
         are determined. See the figures above for the labeling of spots

         Plot zeta_factors for each region

In [12]: ▶| a.plot_zeta_factors(indices=indices)

Out[12]: (<Figure size 432x288 with 2 Axes>,
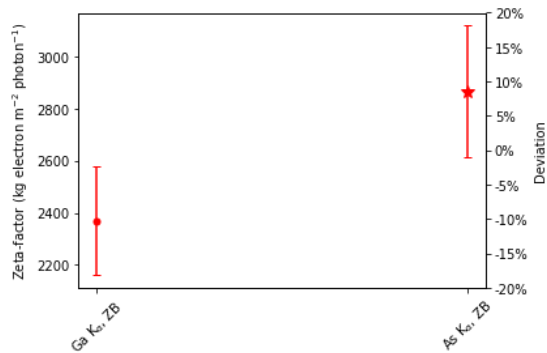   <matplotlib.axes._subplots.AxesSubplot at 0x21cc3f2d550>)

         Find the desired zeta-factors

In [13]: ▶| # Chooze which X-ray lines and region to find zeta-factors from
         ts_Ga = uts.ts_merge(a.tilt_series, xray_lines=['Ga_Ka'], regions=['A', 'C'], indices=indices)
         ts_As = uts.ts_merge(a.tilt_series, xray_lines=['As_Ka'], regions=['A', 'C'], indices=indices)

In [14]: ▶ # Plot the results
             uts.plot_zeta_factors(uts.get_zeta_factors(ts_Ga)+uts.get_zeta_factors(ts_As))

Out[14]: (<Figure size 432x288 with 2 Axes>,
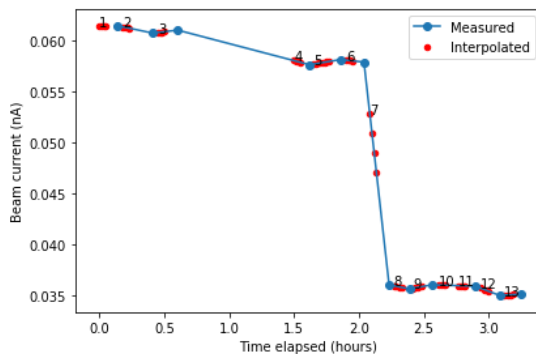   <matplotlib.axes._subplots.AxesSubplot at 0x21cc40af7f0>)

Analyze beam current

Plot the beam current along with interpolated beam currents

In [15]: ▶ #All methods which are available in BeamCurrentAnalyzer are available here as well.
             # The red spots are the individual EDX spectra, whose beam current has been interpolated from the
             measurements
             a.plot_beam_current(interpolated=True, label=True, ref_dec=1)

Out[15]: (<Figure size 432x288 with 1 Axes>,
          <matplotlib.axes._subplots.AxesSubplot at 0x21cd338dda0>)

C.1.4   Using the MapAnalyzer class

The MapAnalyzer class is made for analyzing multiple EDX maps. Each EDX map is given a label (e.g. "B3"), which is the same as the filename of the EDX map. As for the SpotAnalyzer class, a demo notebook has been made for demonstrating functionality. Note that the MapAnalyzer is similar to the SpotAnalyzer in many aspects.

MapAnalyzer - Demo

Imports

```
In [1]:  %matplotlib inline
         import numpy as np
         import matplotlib.pyplot as plt
         import hyperspy.api as hs
         import uts      # Import the uts.py module
```

. . .

Setup

```
In [2]:  # Define a dictionary `params`, which contains all information necessary to create a MapAnalyzer
         object

         params = {
             'id': 'ts_2100f_sc48_b_map',      # Unique id for the dataset
             'folder': r'C:\Users\danie\Docsys-PC\Master_Data\raw\2019-05-06_ts_2100f_sc48_b_map_E6',      #
         Folder containing the EDX data
             'description': {     # Description of each individual EDX map
                 'A1': 'on zone',
                 'A2': 'partially on zone',
                 'A3': 'off zone'
             },
             'all_elements': ['Ga', 'As', 'Sb', 'Cu', 'C', 'O', 'Si', 'Fe'],      # Specify all elements which
         are present in the samples. Useful when plotting spectra.
             'pre_processing': lambda x: x.sum('y'),      # Apply some function to each EDX map before .
         Often, it is useful to sum the map over one of the axes or rebin the signal.
             'pca': 3,     # Specify the number of PCA components to use. If PCA is not used, then specify
         `None`.
             'beam_current': 'from_measurement_files',      # Specify that you want to obtain beam currents
         from .dm3 measurement files. Alternatively, supply beam currents as a dictionary in the format
         {'A1': 1.15, 'A2': 1.18, ...}.
             'counts_per_electron': 4.96,      # Conversion efficiency of the CCD
             'beam_current_strategy': 'middle',      # Set the beam current of each spectrum by interpolation
         the beam current measurements. Other options are `regr`, `mean` and `middle`.
             'intensity': 'model_fitting', # Either `model_fitting` or `window_method`. Specifies how the X-
         ray intensities should be retrieved from the EDX spectra
             'mod_lim': slice(2.5, 20.0),      # If model fitting: Specify the energy range (in keV) which is
         used for model fitting.
             'mod_elements': ['As', 'Cu', 'Ga', 'Sb'],      # If model fitting: Specify which elements should
         be model fitted.
             'composition': lambda x: {'Ga': 0.5, 'As': 0.5},      # Sample composition at each region, in
         at%. Internally, the compositions are converted to wt%.
             'zone_tilt': -1.46,      # Stage tilt (in degrees) at which the nanowire is orthogonal to the
         electron beam (110 zone axis). Used for thickness correction.
             'thickness': lambda x: uts.get_thickness(x, 97.0e-9, params['zone_tilt'], hexagonal=True), #
         Lambda function for retrieving thickness from each signal
             'density': 5317.6,      # Density of GaAs, in kg/m^3
             'xray_lines': ['Ga_Ka', 'As_Ka', 'Sb_La'] # X-ray lines to find zeta-factors from
         }
```

```
In [3]:  # Calibration function, which e.g. can be used to line up multiple maps relative to each other
         def calibration(s):
             if uts.get_label(s) == 'A2':
                 s.axes_manager['x'].offset = 4
             if uts.get_label(s) == 'A3':
                 s.axes_manager['x'].offset = 30
```

```
In [4]:  ▶| # Create the MapAnalyzer object
            a = uts.MapAnalyzer(params, calibration)
```

```
Loading signals...Done
Changing datatype...Done
Applying pre-processing step...Done
Changing datatype...Done
Applying pre-processing step...Done
Changing datatype...Done
Applying pre-processing step...Done
Retrieving PCA results for signal A1 from cache.
Retrieving PCA results for signal A2 from cache.
Retrieving PCA results for signal A3 from cache.
Loading model fitting results from cache
```
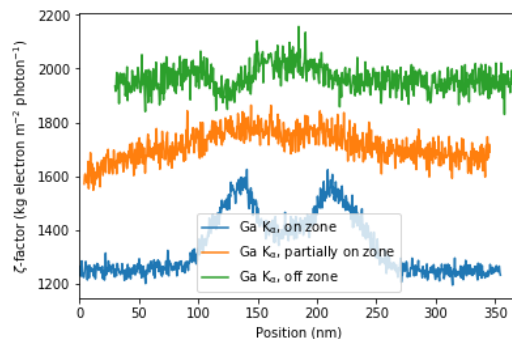
Analysis

Plot intensities

```
In [5]:  ▶| # Plot the Ga_Ka intensities
            fig, ax = a.plot_intensities(xray_lines=['Ga_Ka'])
            uts.add_deviation(ax)
```
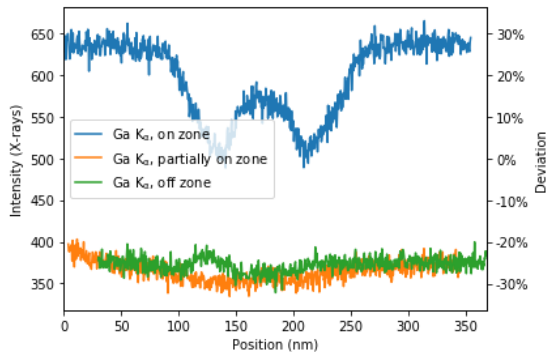

Plot zeta-factors

```
In [6]:  ▶| fig, ax = a.plot_zetas(xray_lines=['Ga_Ka'], option='absolute')
```


Calculate compositions

Determine internal zeta-factors from ROIs

```
In [7]:  ▶|  z_ga = a.determine_zeta_factor('A3', 'Ga_Ka', option='absolute')
```

```
In [8]:  ▶|  print(z_ga)
```

        {'xray_line': 'Ga_Ka', 'label': 'A3', 'zeta': 1964.4888231342143, 'std': 45.72200879063382}

```
In [9]:  ▶|  # The ROIs are specified as a list of tuples. Multiple tuples can be supplied. The tuple arguments
             are the relative position on the map; 0 is to the left, and 1 is to the right.
             z_as = a.determine_zeta_factor('A3', 'As_Ka', option='absolute', rois=[(0, 0.2)], plot=True)
```
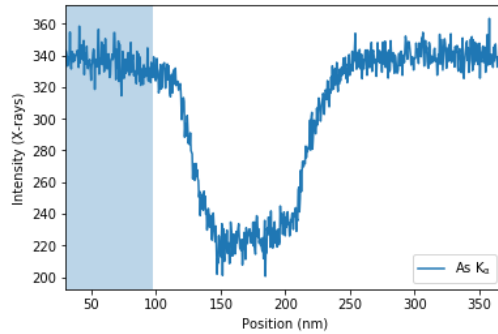


```
In [10]:  ▶|  print(z_as)
```

        {'xray_line': 'As_Ka', 'label': 'A3', 'zeta': 2342.242643745933, 'std': 55.2095847180036}

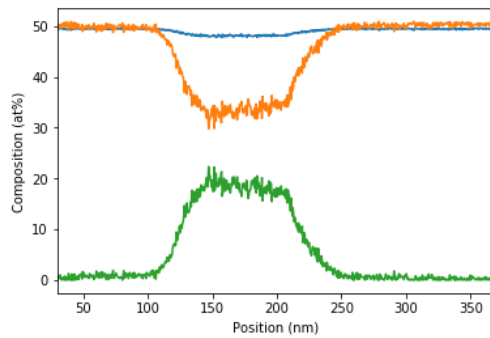Composition from tuned zeta-factors

```
In [11]:  ▶|  z_sb = {'xray_line': 'Sb_La', 'zeta': 3070}
             fig, ax = a.plot_composition(['A3'], 'zeta', {'Ga_Ka': z_ga, 'As_Ka': z_as, 'Sb_La': z_sb},
             legend=False)
```
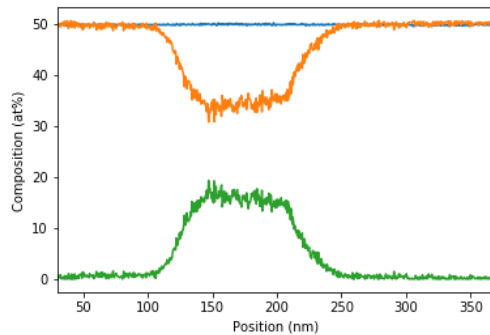

Composition from tabulated zeta-factors

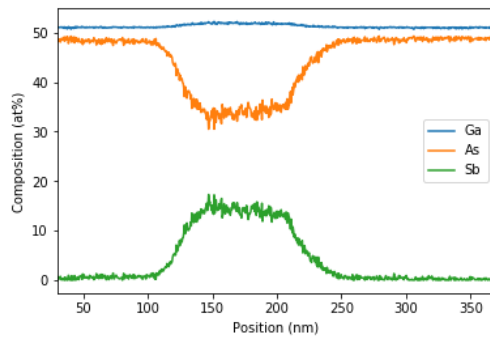In [12]:   ▶| a.plot_composition(['A3'], 'zeta', {'Ga_Ka': 1628, 'As_Ka': 1963, 'Sb_La': 3070}, legend=False)

Out[12]:   (<Figure size 432x288 with 1 Axes>,
             <matplotlib.axes._subplots.AxesSubplot at 0x249a82f55f8>)

Composition by the Cliff-Lorimer method

In [13]:   ▶| a.plot_composition(['A3'], 'CL', {'Ga_Ka': 1.444, 'As_Ka': 1.636, 'Sb_La': 1.935})

Out[13]:   (<Figure size 432x288 with 1 Axes>,
             <matplotlib.axes._subplots.AxesSubplot at 0x249a8092a20>)

C.2 Implementation details

This section describes implementation details of selected features of the `uts.py` module.

C.2.1 Thickness correction

The thickness correction in the `uts.py` module are implementation of the equations in section 2.6.3. If the `hexagonal` argument is `True`, then "hexagonal correction" is performed (figure 2.24(a)); if it is `False` then "thin-film correction" is performed (figure 2.24(b)).

```python
def get_thickness(s, width, zone_tilt, hexagonal=False,
    ↪ beam_width=0):
    if isinstance(s, hs.signals.BaseSignal): stage_tilt = s.
        ↪ metadata.Acquisition_instrument.TEM.Stage.tilt_alpha
    else: stage_tilt = s

    tilt = stage_tilt - zone_tilt
    if hexagonal:
        if tilt > 30: # Degrees
            tilt = tilt - 60
    if beam_width == 0:
        fac = 1 / np.cos(np.deg2rad(tilt))
    else: # Beam width correction (experimental)
        fac = (1 / np.cos(np.deg2rad(tilt)) - 1) * (1-beam_width)
            ↪  + 1
    t = get_uniform_thickness(width)
    return t*fac


def get_uniform_thickness(width):
    return np.sqrt(3)/2 * width
```

C.2.2 Estimating beam current

The beam current has been measured using a DigitalMicrograph script, and are then imported to a `BeamCurrentAnalyzer` class as described in section 5.1.

The beam currents are measured in between the acquisition of EDX spectra. To estimate the beam current at the time of each EDX spectrum, linear interpolation is

used. This is illustrated in figure C.2. The blue spots indicate actual measurements, while the red spots indicate interpolated values. The labels denote each EDX spectrum. The interpolation has been done based on the exact at which the EDX spectra were acquired.
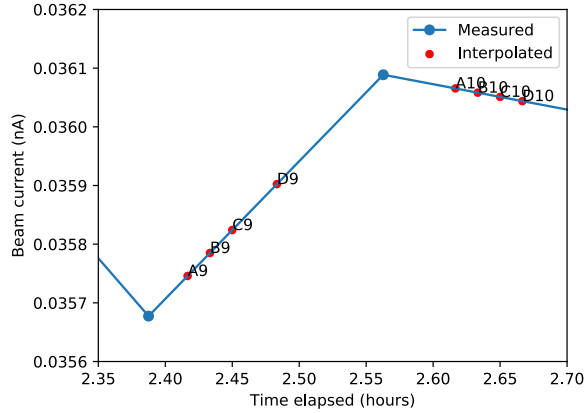

Figure C.2: The beam current at the time of each EDX spectrum (marked as red spots) is interpolated between the actual beam current measurements (marked as blue spots), based on the exact time the EDX spectrum was acquired.

It has proven to be crucial to account for beam current when estimating ζ-factors; in particular, this can be seen on figure C.3. If beam current variations were not accounted for, there would be a significant offset at stage tilts around 30°.
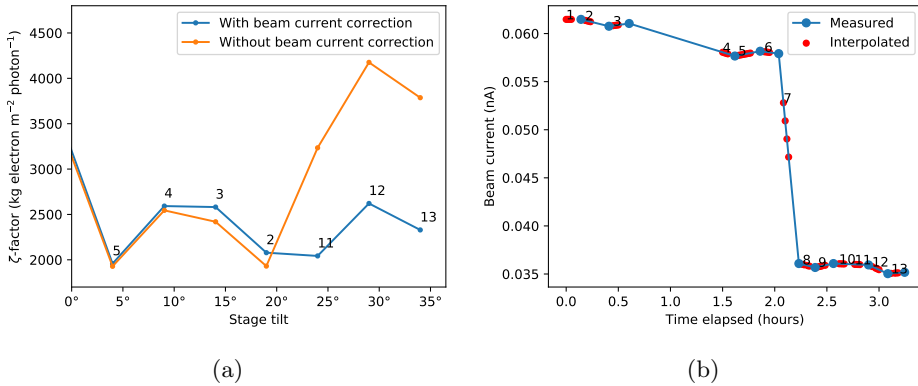

Figure C.3: (a) ζ-factor dependence on stage tilt, with and without taking into account variations in beam current. (b) Measured beam current. For the ζ-factor with a given index, the beam current with the same index was used. The measurements are from experiment E3.

C.2.3   Model fitting

In the `uts.py` module, X-ray intensities can be extracted using model fitting (refer to the "Model Fitting" section in the HyperSpy User Guide [37]). For this project, all intensities have been extracted using model fitting. First, each X-ray peak is modeled as a Gaussian component, and the background is modeled as a polynomial function. Then, the peaks and the background are fitted to the real spectrum by an optimization procedure. The X-ray intensity is then found as the area under the Gaussian component. To perform the fitting, some adjustments have been made. This is described in the following paragraph. The description is quite technical and requires knowledge on how model fitting works in HyperSpy.

First, the coupling of relative intensities of X-ray peaks within the same family is removed. This is done by setting the `twin` attribute to `None`. By default in HyperSpy, these X-ray peaks have a fixed ratio; however different sources provide different values for this ratio (see table 2.1 for some example), and the ratio used in HyperSpy does not correspond well to the ratios in the experimental spectra. Then, the `sigma` and `center` parameters are set free to enable the optimizer to adjust them. These parameters control the width and the position, respectively, of the Gaussian peaks. However, bounds are set on these parameters, so that only small adjustments from the default value are permitted. As is default, the area `A` is allowed to be adjusted (of course, only positive values for `A` are permitted).

In the case of EDX maps, the described procedure is applied to the sum spectrum. Then, the values of `sigma` and `center` are stored, and the value of the `twin` attribute is estimated. These parameters are then used when fitting each single spectrum of the EDX map, permitting only the area attribute `A` to be adjusted.

In the `uts.py` module, the model fitting results are cached and then restored when needed.

This procedure has proven to give models which fit well to the experimental EDX spectra. For an example, see figure C.4. Note how the overlapping peaks are elegantly deconvoluted into two Gaussian components.
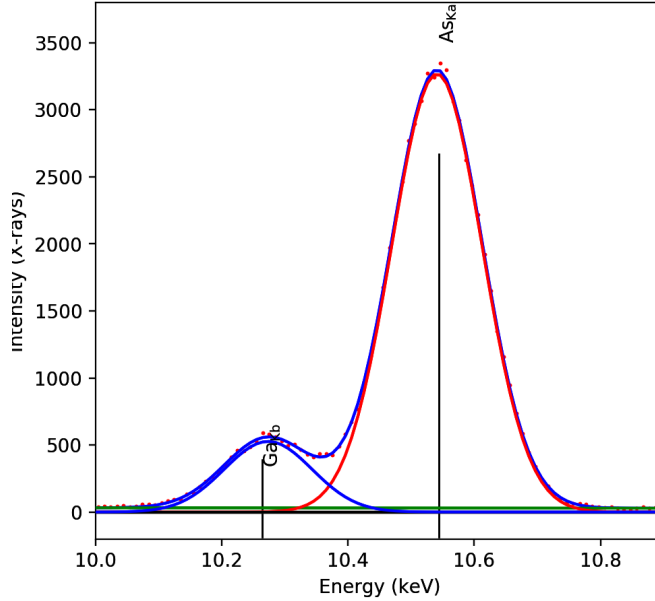
Figure C.4: Example of model fitting results.

The exact model fitting procedure can be found by looking at the function `_model_fit` ↪ in the class `ModelFitter` in the `uts.py` module.

C.2.4 Signal pre-processing

EDX maps can optionally be pre-processed using the `uts.py` module. PCA processing is specified by using the `pca` key in the `params` dictionary supplied to the `MapAnalyzer` object. The value is the number of PCA components to retain; if `None`, then PCA is not applied. Any processing prior to PCA, such as binning, can be specified using the `pre_processing` key in the `params` dictionary. The pre-processing operation is then supplied as a function, which accepts the input signal as an argument and returns the processed signal.

For this project, all EDX maps have been rebinned in order to increase the counting statistics for each spectrum. Typically, a set of 8×8 pixels is combined into a single pixel. Finally, the EDX maps have been PCA processed. The neck in the explained variance ratio has been used as an indication of the number of components to retain.

Appendix D

Supplementary data

This section contains figures, plots, images and other data to supplement the main report.

D.1 TEM images used for thickness determination
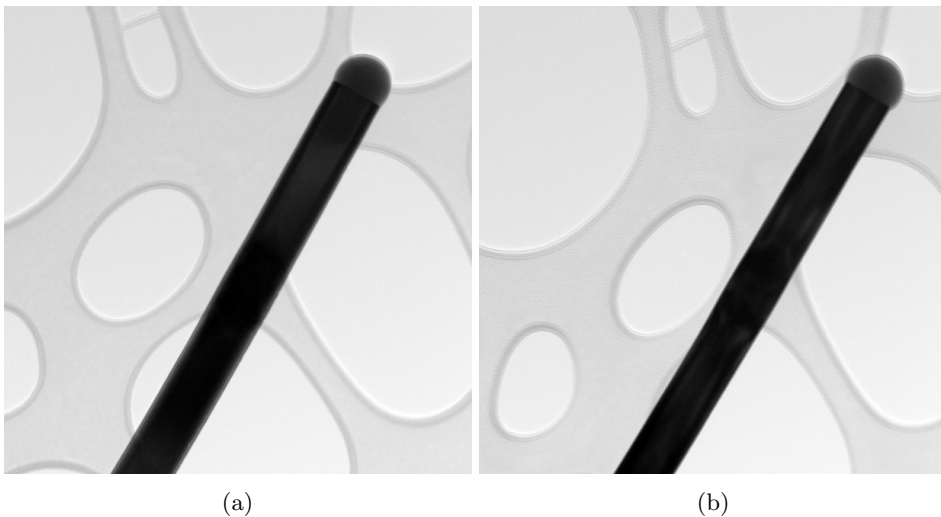

(a)   (b)

Figure D.1: TEM image of a NW taken at (a) a [110] zone axis and (b) a [112] zone axis by tilting against the NW axis. These images were used for thickness measurements, and for verifying the NW symmetry.
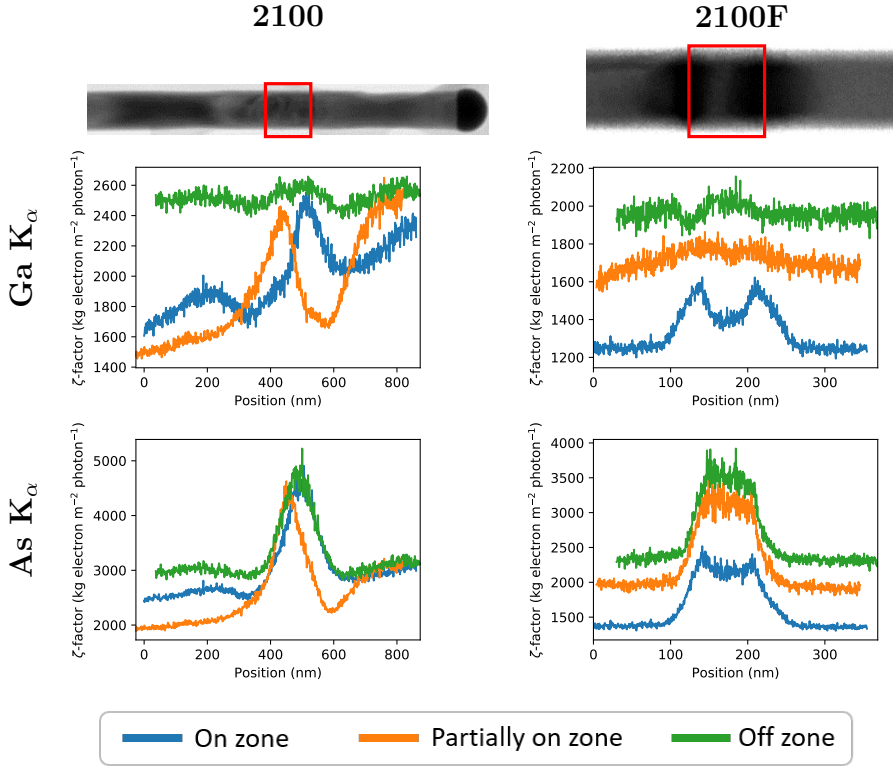
D.2 ζ-factor determination on zone axes

Figure D.2: ζ-factors as a function of position on the NW, under different crystal orientations. When "on zone", the NW was oriented on the (110) zone axis. When "partially on zone", the NW was tilted off 12° in the x-tilt axis (α-tilt), and the y-tilt (β-tilt) was tuned to make the y-orientation on zone. When "off zone", the NW was tilted an additional 3° in the y-tilt axis. The NW orientation is believed to change gradually along the growth axis due to strain in the insert region, which is indicated by a red rectangle. The JEOL 2100 and JEOL 2100F experiments have ID E5 and E6, respectively.

D.3 Corrections to the CCD camera

Two types of corrections are in mainstream use in all modern digital image acquisition devices:

Dark correction: Corrects for the displacement of detector response. Dark correction is performed by the CCD camera immediately before the acquisition of an

image, by acquiring a *dark reference image*. A dark reference image is an image taken at no beam current.

Gain correction: Corrects for differences in *responsivity* of the sensors, meaning to what extent the output signal depends on the input signal. Gain reference images are recorded manually, and they should be recorded on a regular basis. It is crucial to perform dark correction prior to gain correction.

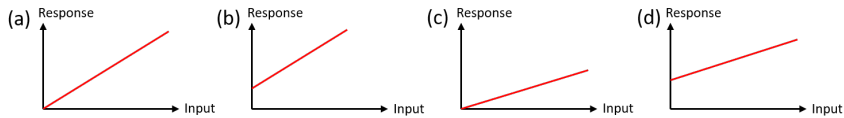Figure D.3 visualizes the two types of corrections.

Figure D.3: Sketch of detector anomalies which can be corrected by dark and gain corrections (a) Ideal detector response. (b) Displacement of detector response, which is handled by dark correction. (c) Deviation of detector responsivity, which is handled by gain correction. (d) Difference in both displacement and responsivity of the detector, which is handled by the combination of dark and gain correction.
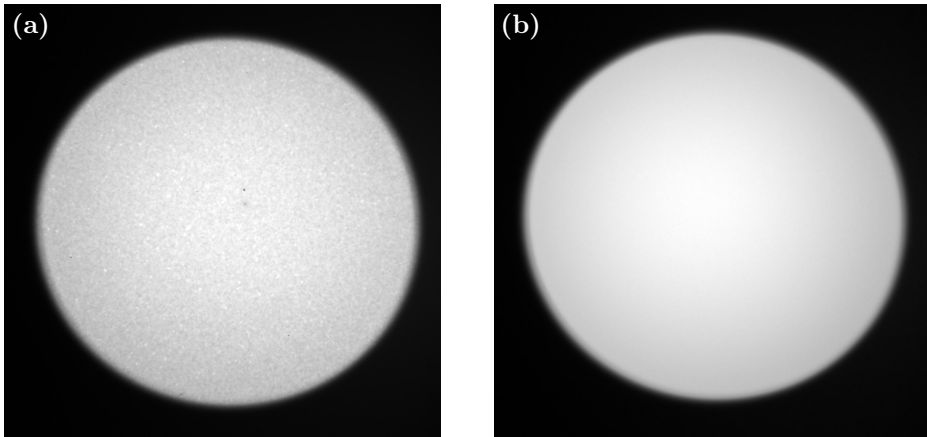

Figure D.4: CCD image of the electron beam in vacuum. (a) No corrections have been applied. (b) Dark and gain corrections have been applied. There is a clear visual improvement on the dark- and gain corrected image.

There exists a number of additional corrections, e.g. linearization correction, defect correction and bias correction, which all contribute to making the image more physically correct.
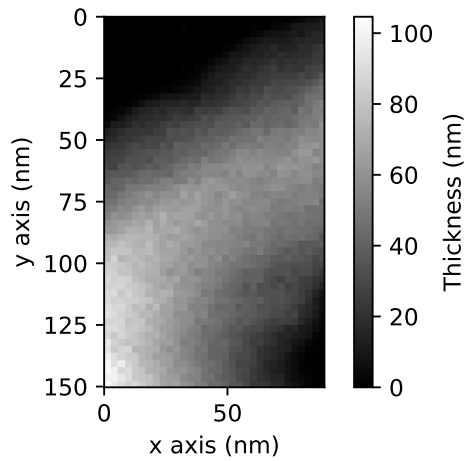
D.4 Thickness map

Figure D.5: Thickness map of the GaSb particle shown in figure 4.18(b). The thickness map has been calculated using the ζ-factor method, using $Ga\,K_\alpha$ and $Sb\,L_\alpha$ ζ-factors found in section 4.3.3.

Appendix E

Python code for self-absorption plot

Figure 2.15 was created using HyperSpy. This section contains the code to create the plot.

Using HyperSpy to calculate self absorption plots

This notebook demonstrates how to use HyperSpy to create "critical specimen thickness by self absorption" plots.

The calculation is simply based on Beer-Lamberts-law:

$$I = I_0 \exp\left(-[\mu/\rho] * \rho t\right)$$

For the calculation, the expression is rearranged to:

$$t = -\frac{\log(I/I_0)}{[\mu/\rho] * \rho}$$

The absorption constant $[\mu/\rho]$ of the `Ga_Ka` line in pure `Ga` is given by the constant found by `hs.material.mass_absorption_coefficient('Ga', 'Ga_Ka')` .

```
In [1]:    %matplotlib inline
           import matplotlib.pyplot as plt
           import numpy as np
           import hyperspy.api as hs
```

. . .

```
In [2]:    def create_absorption_data(family, absorption):

               element_dictionary = hs.material.elements.as_dictionary()
               elements = sorted(list(element_dictionary.keys()), key=lambda x: element_dictionary[x]
           ['General_properties']['Z'])

               x = []
               y = []
               energies = []

               for el in elements:
                   try:
                       rho = hs.material.elements[el].Physical_properties.density_gcm3
                       abs_coeff = hs.material.mass_absorption_coefficient(el, el + '_' + family + 'a')
                       t = - np.log(1-absorption) / (rho * abs_coeff)
                       t = t * (1e-2) * 1e9    # From cm to m, and then to nm
                       x.append(hs.material.elements[el].General_properties.Z)
                       y.append(t)
                       energies.append(hs.material.elements[el].Atomic_properties.Xray_lines[family +
           'a'].energy_keV)
                   except:
                       pass

               return {'atomic_number': x, 'critical_thickness': y, 'energies': energies}

           def plot_absorption_data(families, absorption=0.05, guideline=30, kev_limit=20):
               for i, family in enumerate(families):
                   data = create_absorption_data(family, absorption)
                   i_lim = np.argmax( np.array(data['energies']) > kev_limit )
                   if i_lim == 0: i_lim = -1
                   plt.plot(data['atomic_number'][:i_lim], data['critical_thickness'][:i_lim], '.-',
           color='C'+str(i), label=family + ' lines')
                   if i_lim != -1:
                       plt.plot(data['atomic_number'][i_lim-1:-1], data['critical_thickness'][i_lim-1:-1], '.-
           ', color='C'+str(i), alpha=0.2)
               plt.axhline(y=guideline, linestyle='--', color='grey', label=str(guideline)+' nm')
               plt.gca().set_yscale('log')
               plt.xlabel('Atomic number')
               plt.ylabel('Specimen thickness at ' + str(absorption*100) + ' %\nX-ray absorption (nm)')
               plt.ylim(10e-1, 10e8)
               plt.legend()
               plt.tight_layout()
```
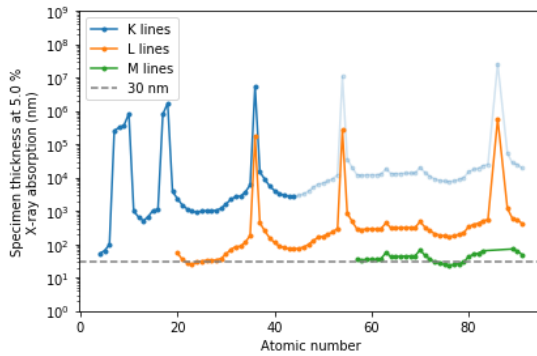
```
plot_absorption_data(['K', 'L', 'M'], absorption=0.05, guideline=30, kev_limit=20)
```


For reference, here is the plot by Watanabe et. al (2006) (https://onlinelibrary.wiley.com/doi/full/10.1111/j.1365-2818.2006.01549.x). Note that there are some large deviations.
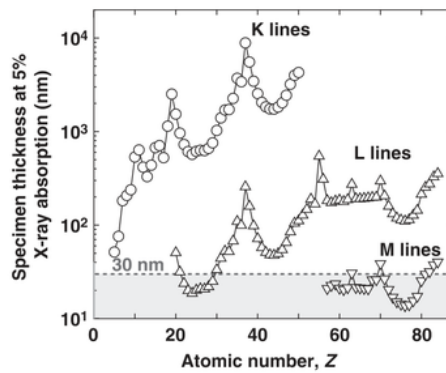

Fig. 2. The critical specimen thickness at 5% X-ray absorption in the pure element thin films. The shadowed area indicates the specimen thickness range below 30 nm. The critical thicknesses at the 5% absorption for all the K line and most of the L lines above Zn (> ~1 keV) are higher than the 30 nm.